INFORMATION TO USERS

This manuscript has been reproduced from the microfilm master. UMI films the text directly from the original or copy submitted. Thus, some thesis and dissertation copies are in typewriter face, while others may be from any type of computer printer.

The quality of this reproduction is dependent upon the quality of the copy submitted. Broken or indistinct print, colored or poor quality illustrations and photographs, print bleedthrough, substandard margins, and improper alignment can adversely affect reproduction.

In the unlikely event that the author did not send UMI a complete manuscript and there are missing pages, these will be noted. Also, if unauthorized copyright material had to be removed, a note will indicate the deletion.

Oversize materials (e.g., maps, drawings, charts) are reproduced by sectioning the original, beginning at the upper left-hand corner and continuing from left to right in equal sections with small overlaps.

Photographs included in the original manuscript have been reproduced xerographically in this copy. Higher quality 6" x 9" black and white photographic prints are available for any photographs or illustrations appearing in this copy for an additional charge. Contact UMI directly to order.

ProQuest Information and Learning
300 North Zeeb Road, Ann Arbor, MI 48106-1346 USA
800-521-0600

Three-Dimensional Computational Analysis of Transport Phenomena in a PEM Fuel Cell

by

Torsten Berning
Dipl.-Ing., RWTH Aachen, 1997

A Dissertation Submitted in Partial Fulfillment of the
Requirements for the Degree of

DOCTOR OF PHILOSOPHY

in the Department of Mechanical Engineering.

We accept this dissertation as conforming
to the required standard

Dr. N. Djilali, Supervisor (Department of Mechanical Engineering)

Dr. Z. Dong, Departmental Member (Department of Mechanical Engineering)

Dr. S. Dost, Departmental Member (Department of Mechanical Engineering)

Dr. F. Gebali, Outside Member (Department of Electrical Engineering)

Dr. T. V. Nguyen, External Examiner (University of Kansas)

Supervisor: Dr. N. Djilali

Abstract

Fuel cells are electrochemical devices that rely on the transport of reactants (oxygen and hydrogen) and products (water and heat). These transport processes are coupled with electrochemistry and further complicated by phase change, porous media (gas diffusion electrodes) and a complex geometry. This thesis presents a three-dimensional, non-isothermal computational model of a proton exchange membrane fuel cell (PEMFC). The model was developed to improve fundamental understanding of transport phenomena in PEMFCs and to investigate the impact of various operation parameters on performance. The model, which was implemented into a Computational Fluid Dynamics code, accounts for all major transport phenomena, including: water and proton transport through the membrane; electrochemical reaction; transport of electrons; transport and phase change of water in the gas diffusion electrodes; temperature variation; diffusion of multi-component gas mixtures in the electrodes; pressure gradients; multi-component convective heat and mass transport in the gas flow channels.

Simulations employing the single-phase version of the model are performed for a straight channel section of a complete cell including the anode and cathode flow channels. Base case simulations are presented and analyzed with a focus on the physical insight and fundamental understanding afforded by the availability of detailed distributions of reactant concentrations, current densities, temperature and water fluxes. The results are consistent with available experimental observations and

show that significant temperature gradients exist within the cell, with temperature differences of several degrees Kelvin within the membrane-electrode-assembly. The three-dimensional nature of the transport processes is particularly pronounced under the collector plates land area, and has a major impact on the current distribution and predicted limiting current density. A parametric study with the single-phase computational model is also presented to investigate the effect of various operating, geometric and material parameters, including temperature, pressure, stoichiometric flow ratio, porosity and thickness of the gas diffusion layers, and the ratio between the channel with and the land area.

The two-phase version of the computational model is used for a domain including a cooling channel adjacent to the cell. Simulations are performed over a range of current densities. The analysis reveals a complex interplay between several competing phase change mechanisms in the gas diffusion electrodes. Results show that the liquid water saturation is below 0.1 inside both anode and cathode gas diffusion layers. For the anode side, saturation increases with increasing current density, whereas at the cathode side saturation reaches a maximum at an intermediate current density ($\approx 1.1 Amp/cm^2$) and decreases thereafter. The simulation show that a variety of flow regimes for liquid water and vapour are present at different locations in the cell, and these depend further on current density.

The PEMFC model presented in this thesis has a number of novel features that enhance the physical realism of the simulations and provide insight, particularly in heat and water management. The model should serve as a good foundation for future development of a computationally based design and optimization method.

Examiners:

Dr. N. Djilali, Supervisor (Department of Mechanical Engineering)

Dr. Z. Dong, Departmental Member (Department of Mechanical Engineering)

Dr. S. Dost, Departmental Member (Department of Mechanical Engineering)

Dr. F. Gebali, Outside Member (Department of Electrical Engineering)

Dr. T. V. Nguyen, External Examiner (University of Kansas)

Table of Contents

List of Figures

List of Tables

Nomenclature

Symbol	Description	Units
A	Area	m^2
a	Chemical activity	–
b	Tafel slope	$Vdec^{-1}$
C	Electric charge	C
c	Concentration	$mol\,m^{-3}$
D	Diffusion coefficient	$m^2\,s^{-1}$
$[\mathbf{D^0}]$	Matrix of Fick's diffusion coefficients	$m^2\,s^{-1}$
$[\mathbf{D}]$	Matrix of Fick's diffusion coefficients	$m^2\,s^{-1}$
$\mathfrak{D}$	Binary diffusion coefficient	$m^2\,s^{-1}$
E	Cell potential	V
e	Electronic charge	$1.6022 \times 10^{-19}\,C$
F	Faraday's constant	$96485\,C\,mol^{-1}$
G	Gibb's free energy	J
$\bar{g}$	Specific Gibb's free energy	$J\,mol^{-1}$
H	Enthalpy	J
$\bar{h}$	Specific enthalpy	$J\,mol^{-1}$
h	Specific enthalpy	$J\,kg^{-1}$

Symbol	Description	Units
h	Height	m
I	Electric current	A
i	Current density	$\mathrm{A\,m^{-2}}$
i_0	Exchange current density	$\mathrm{A\,m^{-2}}$
J	Molar diffusion flux rel. to molar average velocity	$\mathrm{mol\,m^{-2}\,s^{-1}}$
j	Mass diffusion flux rel. to mass averaged velocity	$\mathrm{kg\,m^{-2}\,s^{-1}}$
K	Chemical equilibrium constant	$-$
k_ϕ	Electrokinetic permeability	$\mathrm{m^2}$
k_p	Hydraulic permeability	$\mathrm{m^2}$
l	Length	m
M	Molecular weight	$\mathrm{kg\,mol^{-1}}$
$\vec{N}$	Molar flux	$\mathrm{mol\,m^{-2}}$
$\dot{N}$	Molar flux (phase change)	$\mathrm{mol\,s^{-1}}$
n	Amount of electrons transferred	$-$
n	Normal vector	$-$
p	Pressure	Pa
$\dot{Q}$	Heat flux	W
$\dot{q}$	Heat source or -flux	$\mathrm{W\,m^{-2}}$
R	Universal gas constant	$8.3145\,\mathrm{J\,mol^{-1}\,K^{-1}}$
R	Electric resistance	Ω
r	Electric resistance	$\Omega\,\mathrm{m^2}$
S	Entropy	$\mathrm{J\,K^{-1}}$
$\bar{s}$	Specific entropy	$\mathrm{J\,mol^{-1}\,K^{-1}}$
s	Saturation	$-$

Symbol	Description	Units
T	Temperature	K
t	Thickness	m
$\mathbf{u}$	Velocity vector	$\mathrm{m\,s^{-1}}$
u	x-component of $\mathbf{u}$	$\mathrm{m\,s^{-1}}$
$\mathbf{v}$	Diffusion velocity vector	$\mathrm{m\,s^{-1}}$
V	Electrical Potential	V
v	y-component of $\mathbf{u}$	$\mathrm{m\,s^{-1}}$
W	Work transfer	W
w	Width	m
w	z-component of $\mathbf{u}$	$\mathrm{m\,s^{-1}}$
x	Molar fraction	–
$(\mathbf{x})$	Molar fraction vector	–
y	Mass fraction	–
$(\mathbf{y})$	Mass fraction vector	–
z	Charge number	–

Greek Letters

Φ	Electrical potential inside the membrane	V
α	Transfer coefficient	–
β	Modified heat transfer coefficient	$\mathrm{W\,m^{-3}\,K^{-1}}$
γ	Concentration coefficient	–
δ	Kronecker Delta	–
ϵ	Efficiency	–
ε	Porosity	–
ζ	Stoichiometric flow ratio	–
η	Overpotential	V
ϑ	Temperature	°C
κ	Membrane (protonic) conductivity	$\mathrm{S\,m^{-1}}$
λ	Thermal conductivity	$\mathrm{W\,m^{-1}\,K^{-1}}$
μ	Chemical Potential	$\mathrm{J\,mol^{-1}}$
μ	Viscosity	$\mathrm{kg\,m^{-1}\,s^{-1}}$
μ	Fuel utilization coefficient	–
ξ	Relative Humidity	–
ϖ	Scaling parameter for evaporation	–
ρ	Density	$\mathrm{kg\,m^{-3}}$
σ	(*i*) Electric conductivity	S
σ	(*ii*) Surface Tension	$\mathrm{N\,m^{-1}}$
ϕ	Transported scalar	
φ	Roughness factor	–
ψ	Oxygen/nitrogen ratio	–

Subscripts	Description
$()_a$	Anode
$()_{act}$	Activation
$()_{ave}$	Average
$()_C$	Carnot
$()_c$	*i*). Cathode; *ii*). contact
$()_{ch}$	Channel
$()_{conc}$	Concentration
$()_{cond}$	Condensation
$()_d$	Drag
$()_e$	Gas diffusion electrode
$()_{eff}$	Effective value
$()_{evap}$	evaporation
$()_f$	*i*). faradaic, *ii*). fixed charge in the membrane
$()_g$	Gas phase
$()_{gr}$	Graphite

Subscripts	Description
$()_h$	hot
$()_i$	i). internal, ii). Species i;
$()_{ij}$	Gas pair i, j in a mixture
$()_l$	Liquid phase
$()_{mem}$	Membrane
$()_{ohm}$	Ohmic
$()_{Pt}$	Platinum
$()_p$	Value at constant pressure
$()_{rev}$	reversible
$()_{ref}$	reference
$()_s$	Solid phase
$()_{sat}$	Saturation
$()_{theo}$	Theoretical value
$()_{tot}$	total
$()_w$	Water
$()^0$	Standard value

Acknowledgements

The computational model presented in this thesis is based on the work by Dr. Dongming Lu and Dr. Ned Djilali at the Institute for Integrated Energy Systems of the University of Victoria (IESVic).

I am very grateful to Dr. Ned Djilali for giving me the opportunity to work on such an exciting project and for his constant encouragement and valuable guidance throughout this work.

I want to thank Dr. Dongming Lu for his guidance and assistance in the beginning of my work.

Many thanks to Sue Walton, who encouraged me to revise these acknowledgements and to all my fellow graduate students.

Most of all, I want to thank my parents for their unconditional support throughout all the years of my education. This dissertation would not have been possible without them.

This work was in part funded by the National Science and Engineering Research Council of Canada, British Gas, and Ballard Power Systems under the NGFT project.

Chapter 1

Introduction

1.1 Background

Fuel Cells (FC's) are electrochemical devices that directly convert the chemical energy of a fuel into electricity. In contrast to batteries, which are energy storage devices, fuel cells operate continuously as long as they are provided with reactant gases. In the case of a hydrogen/oxygen fuel cells, which are the focus of most research activities today, the only by-product is water and heat. The high efficiency of fuel cells and the prospects of generating electricity without pollution have made them a serious candidate to power the next generation of vehicles. More recently, focus of fuel cell development has extended to remote power supply and applications, in which the current battery technology reduces availability because of high recharging times compared to a short period of power supply (*e.g.* cellular phones). Still, one of the most important issues impeding the commercialization of fuel cells is the cost; the other major issue, particularly for urban transportation applications, is the source and/or storage of hydrogen. Drivers for fuel cell development are mainly the much

discussed greenhouse effect, local air quality and the desire of industrialized countries to reduce their dependency on oil imports.

The different types of fuel cells are distinguished by the electrolyte used. The Proton-Exchange Membrane Fuel Cell (PEMFC), which is the focus of this thesis, is characterized by the use of a polymer electrolyte membrane. Low operating temperature ($60 - 90\,°C$), a simple design and the prospect of further significant cost reduction make PEMFC technology a prime candidate for automotive applications as well as for small appliances such as laptop computers.

Still, current PEMFC's are significantly more expensive than both internal combustion engines and batteries. If these fuel cells are to become commercially viable, it is critical to reduce cost and increase power density through engineering optimization, which requires a better understanding of PEMFC's and how various parameter affect their performance. While prototyping and experimentation are excellent tools, they are expensive to implement and subject to practical limitations. Computer modelling is more cost effective, and easier to implement when design changes are made.

In this thesis, a theoretical model will be formulated for the various processes that determine the performance of a single PEMFC, and the effect of various design and operating parameters on the fuel cell performance. This model is implemented in a computational fluid dynamics code allowing comprehensive numerical simulations. In addition, a two-phase model is formulated and implemented in order to address water-management issues.

1.2 Operation Principle of a PEM Fuel Cell

Figure 1.1 shows the operation principle of a PEM Fuel Cell. Humidified air enters the cathode channel, and a hydrogen-rich gas enters the anode channel. The hydrogen diffuses through the anode diffusion layer towards the catalyst, where each hydrogen molecule splits up into two hydrogen protons and two electrons according to:

$$2H_2 \rightarrow 4H^+ + 4e^- \tag{1.1}$$

The protons migrate through the membrane and the electrons travel through the conductive diffusion layer and an external circuit where they produce electric work. On the cathode side the oxygen diffuses through the diffusion layer, splits up at the catalyst layer surface and reacts with the protons and the electrons to form water:

$$O_2 + 4H^+ + 4e^- \rightarrow 2H_2O \tag{1.2}$$

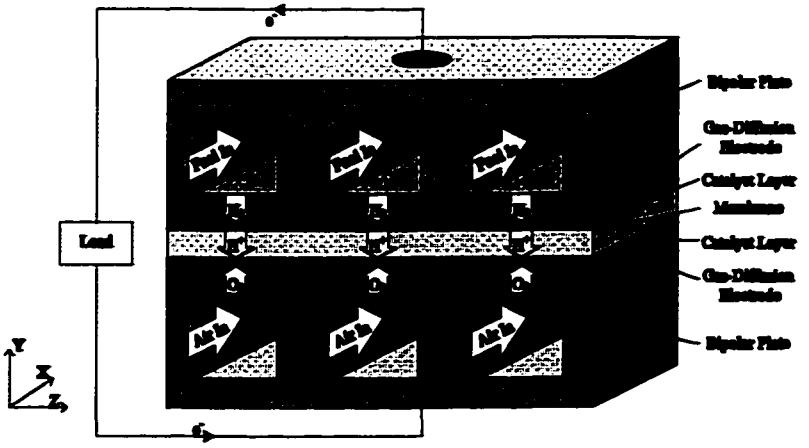

Figure 1.1: Operating scheme of a PEM Fuel Cell.

Reaction 1.1 is slightly endothermic, and reaction 1.2 is heavily exothermic, so that overall heat is created. From above it can be seen that the overall reaction in a PEM Fuel Cell can be written as:

$$2H_2 + O_2 \rightarrow 2H_2O \tag{1.3}$$

Based on its physical dimensions, a single cell produces a total amount of current, which is related to the geometrical cell area by the current density of the cell in $[\mathrm{A}/\mathrm{cm}^2]$. The cell current density is related to the cell voltage via the polarization curve, and the product of the current density and the cell voltage gives the power density in $[\mathrm{W}/\mathrm{cm}^2]$ of a single cell.

1.3 Fuel Cell Components

1.3.1 Polymer Electrolyte Membrane

An important part of the fuel cell is the electrolyte, which gives every fuel cell its name. In the case of the Proton-Exchange Membrane Fuel Cell (or Polymer-Electrolyte Membrane Fuel Cell) the electrolyte consists of an acidic polymeric membrane that conducts protons but repels electrons, which have to travel through the outer circuit providing the electric work. A common electrolyte material is Nafion from DuPont, which consists of a fluoro-carbon backbone, similar to Teflon, with attached sulfonic acid (SO_3^-) groups. The membrane is characterized by the fixed-charge concentration (the acidic groups): the higher the concentration of fixed-charges, the higher is the protonic conductivity of the membrane. Alternatively, the term "equivalent weight" is used to express the mass of electrolyte per unit charge.

For optimum fuel cell performance it is crucial to keep the membrane fully humidified at all times, since the conductivity depends directly on water content [38]. The thickness of the membrane is also important, since a thinner membrane reduces the ohmic losses in a cell. However, if the membrane is too thin, hydrogen, which is much more diffusive than oxygen, will be allowed to cross-over to the cathode side and recombine with the oxygen without providing electrons for the external circuit. The importance of these internal currents will be discussed in section 1.4.3. Typically, the thickness of a membrane is in the range of $5 - 200\,\mu$m [21].

1.3.2 Catalyst Layer

For low temperature fuel cells, the electrochemical reactions occur slowly especially at the cathode side; the exchange current density on a smooth electrode being in the range of only $10^{-9}\,\mathrm{A/cm^2}$ [2]. This gives rise to a high activation overpotential, as will be discussed in a later chapter. In order to enhance the electrochemical reaction rates, a catalyst layer is needed. Catalyzed carbon particles are brushed onto the gas-diffusion electrodes before these are hot-pressed on the membrane. The catalyst is often characterized by the surface area of platinum by mass of carbon support. The electrochemical half-cell reactions can only occur, where all the necessary reactants have access to the catalyst surface. This means that the carbon particles have to be mixed with some electrolyte material in order to ensure that the hydrogen protons can migrate towards the catalyst surface. This "coating" of electrolyte must be sufficiently thin to allow the reactant gases to dissolve and diffuse towards the catalyst surface. Since the electrons travel through the solid matrix of the electrodes, these have to be connected to the catalyst material, *i.e.* an isolated carbon particle with platinum

surrounded by electrolyte material will not contribute to the chemical reaction.

Ticianelli *et al.* [42] conducted a study in order to determine the optimum amount of Nafion loading in a PEM Fuel Cell. For high current densities, the increase in Nafion content was found to have positive effects only up to 3.3% of Nafion, after which, the performance starts to decrease rapidly. Although the catalyst layer thickness can be up to 50 μm thick, it has been found that almost all of the electrochemical reaction occurs in a 10 μm thick layer closest to the membrane [41].

1.3.3 Gas-Diffusion Electrodes

The gas-diffusion electrodes (GDE) consist of carbon cloth or carbon fiber paper and they serve to transport the reactant gases towards the catalyst layer through the open wet-proofed pores. In addition, they provide an interface when ionization takes place and transfer electrons through the solid matrix. GDE's are characterized mainly by their thickness (between 100 μm and 300 μm) and porosity. The hot-pressed assembly of the membrane and the gas-diffusion layer including the catalyst is called the *Membrane-Electrode-Assembly* (*MEA*).

1.3.4 Bipolar Plates

The role of the bipolar plates is to separate different cells in a fuel cell stack, and to feed the reactant gases to the gas-diffusion electrodes. The gas-flow channels are carved into the bipolar plates, which should otherwise be as thin as possible to reduce weight and volume requirements. The area of the channels is important, since in some cases a lot of gas has to be pumped through them, but on the other hand there has to be a good electrical connection between the bipolar plates and the gas-diffusion layers

to minimize the contact resistance and hence ohmic losses [23]. A judicious choice of the land to open channel width ratio is necessary to balance these requirements.

1.4 Fuel Cell Thermodynamics

1.4.1 Free-Energy Change of a Chemical Reaction

Electrochemical energy conversion is the conversion of the free-energy change associated with a chemical reaction directly into electrical energy. The free-energy change of a chemical reaction is a measure of the maximum net work obtainable from the reaction. It is equal to the enthalpy change of the reaction only if the entropy change, $\Delta\bar{s}$, is zero, as can be seen from the equation:

$$\Delta\bar{g} = \Delta\bar{h} - T\Delta\bar{s} \tag{1.4}$$

If in a chemical reaction the number of moles of gaseous products and reactants are equal, the entropy change of such a reaction is effectively zero. Because the number of molecules on the product side of equation 1.3 is lower than on the reactant side, the entropy change inside the PEM Fuel Cell is negative, which means that the amount of energy obtainable from the enthalpy is reduced. The standard Gibb's free enthalpy for the overall reaction in a PEM Fuel Cell is $\Delta\bar{g}^0 = -237.3 \times 10^3\,\mathrm{J/mol}$ when the product water is in the liquid phase [11].

On the other hand, the Gibb's free energy of a reaction

$$\alpha A + \beta B \rightarrow \gamma C + \delta D \tag{1.5}$$

is given by the difference in the chemical potential μ of the indicated species:

$$\Delta\bar{g} = \gamma\mu_C + \delta\mu_D - \alpha\mu_A - \beta\mu_B \tag{1.6}$$

where the chemical potential is defined as [11]:

$$\mu_i = \left(\frac{\partial\bar{g}}{\partial n_i}\right)_{T,p,n_j} ; j \neq i \tag{1.7}$$

The chemical potential of any substance can be expressed by [26]:

$$\mu = \mu^0 + RT\ln a \tag{1.8}$$

where a is the activity of the substance and μ has the value μ^0 when a is unity. The standard free energy of reaction of equation 1.5 is then given by equation 1.6 with the chemical potentials of all species replaced by their standard chemical potentials:

$$\Delta\bar{g}^0 = \gamma\mu_C^0 + \delta\mu_D^0 - \alpha\mu_A^0 - \beta^0\mu_B \tag{1.9}$$

Substituting equation 1.8 for each of the reactants and products, and equation 1.9 into equation 1.6 results in

$$\Delta\bar{g} = \Delta\bar{g}^0 + RT\ln\frac{a_C^\gamma a_D^\delta}{a_A^\alpha a_B^\beta} \tag{1.10}$$

For a process at constant temperature and pressure at equilibrium the free-energy change is zero. It follows that

$$\Delta\bar{g}^0 = -RT\ln\frac{a_{C,e}^\gamma a_{D,e}^\delta}{a_{A,e}^\alpha a_{B,e}^\beta} = -RT\ln K \tag{1.11}$$

The suffices e in the activity terms indicate the values of the activities at equilibrium, and K is the equilibrium constant for the reaction.

Once $\Delta\bar{g}^0$ is determined, $\Delta\bar{g}$ can be calculated for any composition of a reaction mixture. The value of $\Delta\bar{g}$ indicates whether a reaction will occur or not. If $\Delta\bar{g}$ is positive, a reaction can not occur for the assumed composition of reactants and products. If $\Delta\bar{g}$ is negative, a reaction can occur.

1.4.2 From the Free-Energy Change to the Cell Potential: The Nernst Equation

In order to derive an expression for the free-energy change in a fuel cell, we consider a system as denoted in Figure 1.2.

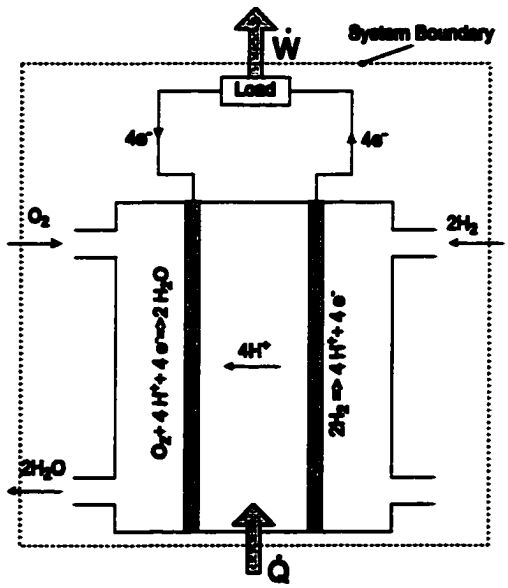

Figure 1.2: Open system boundaries for thermodynamic considerations.

Assuming an isothermal system and applying the first law of thermodynamics for an open system, we find that:

$$0 = \dot{n}_{H_2}\bar{h}_{H_2} + \dot{n}_{O_2}\bar{h}_{O_2} - \dot{n}_{H_2O}\bar{h}_{H_2O} + \dot{Q} - \dot{W} \tag{1.12}$$

where $\dot{n}_i$ are the molar flow rates in [mol / s] and $\bar{h}$ is the molar enthalpy in [J / mol], $\dot{Q}$ and $\dot{W}$ represent the heat transferred to and work done by the system, respectively, in [W]. It is customary in combustion thermodynamics to write this expression on a *per mole of fuel* basis:

$$0 = \bar{h}_{H_2} + \frac{\dot{n}_{O_2}}{\dot{n}_{H_2}}\bar{h}_{O_2} - \frac{\dot{n}_{H_2O}}{\dot{n}_{H_2}}\bar{h}_{H_2O} + \frac{\dot{Q}}{\dot{n}_{H_2}} - \frac{\dot{W}}{\dot{n}_{H_2}} \tag{1.13}$$

Recalling the overall fuel cell reaction:

$$2H_2 + O_2 \rightarrow H_2O \tag{1.14}$$

this leads to:

$$0 = \bar{h}_{H_2} + \frac{1}{2}\bar{h}_{O_2} - \frac{1}{2}\bar{h}_{H_2O} + \frac{\dot{Q}}{\dot{n}_{H_2}} - \frac{\dot{W}}{\dot{n}_{H_2}} \tag{1.15}$$

or:

$$0 = \bar{h}_{in} - \bar{h}_{out} + \frac{\dot{Q}}{\dot{n}_{H_2}} - \frac{\dot{W}}{\dot{n}_{H_2}} \tag{1.16}$$

where $\bar{h}_{in}$ and $\bar{h}_{out}$ denote the incoming and outgoing enthalpy streams per mole of fuel, respectively. Applying the second law of thermodynamics for this case yields:

$$\bar{s}_{out} - \bar{s}_{in} - \frac{\dot{Q}/\dot{n}_{H_2}}{T} \geq 0 \tag{1.17}$$

If the process is carried out reversibly, the equality sign holds and the heat production is given by:

$$\frac{\dot{Q}}{\dot{n}_{H_2}} = T\left(\bar{s}_{out} - \bar{s}_{in}\right) \tag{1.18}$$

Combining the first and the second law we obtain an expression for the work for a reversible process, which is the maximum work obtainable per mole of hydrogen:

$$\frac{\dot{W}_{rev}}{\dot{n}_{H_2}} = \bar{h}_{in} - \bar{h}_{out} - T\left(\bar{s}_{in} - \bar{s}_{out}\right) \tag{1.19}$$

or with the definition of the Gibb's free energy:

$$\frac{\dot{W}_{rev}}{\dot{n}_{H_2}} = \bar{g}_{in} - \bar{g}_{out} = -\Delta\bar{g} \tag{1.20}$$

The reversible work in a fuel cell is defined as the electrical work involved in transporting the charges around the circuit from the anode side towards the cathode side at their reversible potentials, $V_{rev,a}$ and $V_{rev,c}$, respectively. Hence, the maximum electrical work per mole of hydrogen that can be done by the overall reaction carried out in a cell, involving the transport of n electrons *per mole of hydrogen* is:

$$\frac{\dot{W}'_{rev}}{\dot{n}_{H_2}} = ne\left(V_{rev,c} - V_{rev,a}\right) \tag{1.21}$$

This holds under ideal conditions, in which the internal resistance of the cell and the overpotential losses are negligible. To convert into molar quantities, it is necessary to multiply $\dot{W}'_{rev}$ by N, the Avogadro number $\left(6.022 \times 10^{23}\,\mathrm{mol}^{-1}\right)$. As the product

of electronic charge ($e = 1.602 \times 10^{-19}$ C) and Avogadro's number is the *Faraday* F ($96485\,\mathrm{C\,mol^{-1}}$), it follows that

$$\frac{\dot{W}_{rev}}{\dot{n}_{H_2}} = nF\left(V_{rev,c} - V_{rev,a}\right) \tag{1.22}$$

Comparison of this equation with equation 1.20 results in:

$$\Delta\bar{g} = -nF\left(V_{rev,c} - V_{rev,a}\right) \tag{1.23}$$

Noting that

$$\left(V_{rev,c} - V_{rev,a}\right) = E_{rev} \tag{1.24}$$

equation 1.23 becomes

$$\Delta\bar{g} = -nFE_{rev} \tag{1.25}$$

where E is the *electromotive force* (EMF) of the cell. If the reactants and products are all in their standard states, it follows that

$$\Delta\bar{g}^0 = -nFE^0_{rev} \tag{1.26}$$

Combining these equations with equation 1.10 yields:

$$E_{rev} = \frac{-\Delta\bar{g}^0}{nF} - \frac{RT}{nF}\ln\frac{a^{\gamma}_{C,e}a^{\delta}_{D,e}}{a^{\alpha}_{A,e}a^{\beta}_{B,e}} \tag{1.27}$$

which reduces to the common form of the so-called *Nernst Equation*:

$$E_{rev} = E^0_{rev} - \frac{RT}{nF} \ln \frac{a^{\gamma}_{C,e} a^{\delta}_{D,e}}{a^{\alpha}_{A,e} a^{\beta}_{B,e}} \tag{1.28}$$

The power of this equation lies in the fact that it allows the calculation of theoretical cell potentials from a knowledge of the compositions (activities) involved in a given electrochemical reaction.

In the case of the hydrogen-oxygen fuel cell the Nernst equation results in:

$$E_{rev} = E^0_{rev} - \frac{RT}{2F} \ln \frac{a_{H_2O}}{a_{H_2} a^{\frac{1}{2}}_{O_2}} \tag{1.29}$$

The effect of temperature on the free energy change and hence on the equilibrium potential can be found from equation 1.4:

$$\left(\frac{\partial \Delta \bar{g}^0}{\partial T} \right)_p = -\Delta \bar{s}^0 \tag{1.30}$$

and so it follows that:

$$E_{rev,T} = \frac{-\Delta \bar{g}^0}{nF} - \frac{\Delta \bar{s}^0}{2F} \left(T - T^0 \right) - \frac{RT}{2F} \ln \frac{a_{H_2O}}{a_{H_2} a^{\frac{1}{2}}_{O_2}} \tag{1.31}$$

where the activities can be replaced by the partial pressures for ideal gases $a = p_i / p^0$.

1.4.3 Fuel Cell Performance

It is important to realize that the cell potential predicted by the Nernst equation corresponds to an equilibrium (open circuit) state. The actual cell potential under operating conditions (*i.e.* when $i \neq 0$) is always smaller than E^0. Figure 1.3 shows a typical polarization curve of a PEM Fuel Cell.

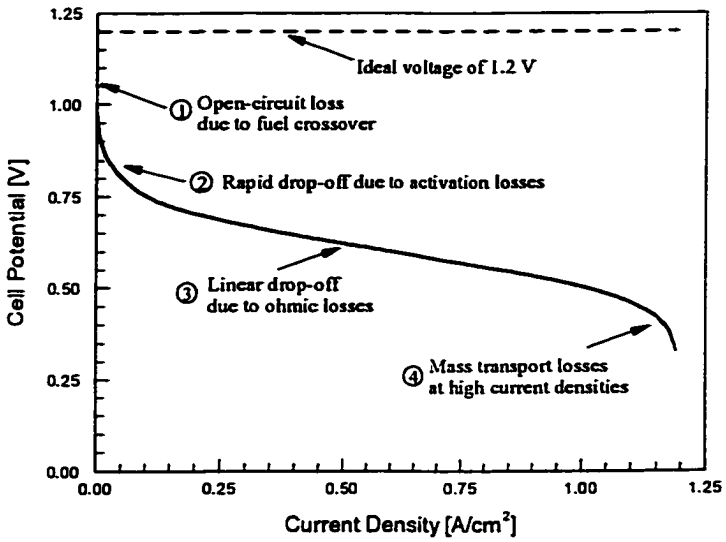

Figure 1.3: Typical polarization curve of a PEM Fuel Cell and predominant loss mechanisms in various current density regions.

The losses that occur in a fuel cell during operation can be summarized as follows:

1. **Fuel crossover and internal currents** occur even when the outer circuit is disconnected. The highly diffusive hydrogen can cross the membrane and recombine with the oxygen at the cathode side. It has been shown that when the internal current is as low as $0.5\,\mathrm{mA}/\mathrm{cm}^2$ the open circuit voltage can drop to 1.0 V [23]. Since the diffusivity of hydrogen increases with temperature, the

open circuit potential decreases [32]. This loss can be reduced by increasing the thickness of the electrolyte at the cost of a higher ohmic loss. In addition, adventitious reactions can cause a mixed-potential in the absence of a net current; one example is the surface oxidation of Pt [30]:

$$Pt + 2H_2O \rightarrow PtO + 2H^+ + 2e^- \tag{1.32}$$

This reaction has an equilibrium potential of $E^0 = 0.88\,\mathrm{V}$, which reduces the observed equilibrium potential for the fuel cell.

2. **Activation losses** are caused by the slowness of the reactions taking place on the surface of the electrodes. A proportion of the voltage generated is lost in driving the chemical reaction that transfers the electrons to or from the electrode. In a PEM Fuel Cell this loss occurs mainly at the cathode side, since exchange current density i_0 of the anodic reaction is several orders of magnitude higher than the cathodic reaction [2]. For most values of the overpotential, a logarithmic relationship prevails between the current density and the applied overpotential, which is described by the so-called *Tafel equation* [4]:

$$\eta_{act} = b \ln \frac{i}{i_0} \tag{1.33}$$

where i is the observed current density and b is the Tafel-slope, which depends on the electrochemistry of the particular reaction.

3. **Ohmic losses** result of the resistance of the electrolyte and is sometimes due to the electrical resistance in the electrodes. It is given by [11]:

$$\eta_{ohm} = ir_i \tag{1.34}$$

where r_i is the internal resistance. When porous electrodes are used the electrolyte within the pores also contributes to the electrolyte resistance. The ohmic loss is the simplest cause of loss of potential in a fuel cell. Reduction in the thickness of the electrolyte layer between anode and cathode may be thought of as an expedient way to eliminate ohmic overpotential. However, "thin" electrolyte layers may cause the problem of crossover or intermixing of anodic and cathodic reactants, which would thereby reduce faradaic efficiencies, as will be discussed in the next section. In addition, the electrons moving through the outer circuit and the electrodes and interconnections experience an ohmic resistance, where the interconnection between the bipolar plates and the porous gas-diffusion electrodes is the most significant (*contact resistance*). Ohmic resistance causes a heating effect of the cell, which is given by:

$$\dot{q}_{ohm} = i^2 r_i \tag{1.35}$$

4. **Mass transport or concentration losses** result from the change in concentration of the reactants at the surface of the electrodes as the reactants are being consumed [23]. At a sufficiently high current density, the rate of reaction consumption becomes equal to the amount of reactants than can be supplied by diffusion, and this is denoted the limiting current density. It can be shown that the voltage drop for a current density i due to concentration overpotential is equal to [23]:

$$\eta_{conc} = \frac{RT}{2F} \ln\left(1 - \frac{i}{i_l}\right) \tag{1.36}$$

where i_l is the limiting current density, R is the universal gas constant and F is Faraday's constant.

1.4.4 Fuel Cell Efficiencies

The Maximum Intrinsic Efficiency

In order to compare the efficiency of electrochemical energy converters with those of other energy conversion devices, it is necessary to have a common base. In the case of an internal combustion engine, the efficiency is defined as the work output divided by the enthalpy of the reactants $\Delta\bar{h}$. For the fuel cell it has also been shown that in the ideal case the Gibb's free energy may be converted into electricity. Thus, an electrochemical energy converter has an intrinsic maximum efficiency given by [11]:

$$\epsilon_i = \frac{\Delta\bar{g}}{\Delta\bar{h}} = 1 - \frac{T\Delta\bar{s}}{\Delta\bar{h}} = -\frac{nF}{\Delta\bar{h}}E_{rev} \tag{1.37}$$

As was mentioned before, the difference in entropy $\Delta\bar{s}$ might be positive, when the total number of moles in the gas phase increases so that the maximum theoretical efficiency can be larger than 100 percent. Examples of fuel cell efficiencies are given in Table 1.1 [11].

Table 1.1: Thermodynamic data for chosen fuel cell reactions

Reaction	T [°C]	$\Delta\bar{g}^0$ [J / mol]	$\Delta\bar{h}^0$ [J / mol]	E_r^0 [V]	ϵ_i
$H_2 + \frac{1}{2}O_2 \rightarrow H_2O$	25	−237,350	−286,040	1.229	0.830
$H_2 + \frac{1}{2}O_2 \rightarrow H_2O$	150	−221,650	−243,430	1.148	0.911
$C + \frac{1}{2}O_2 \rightarrow CO$	25	−137,370	−110,620	0.711	1.24
$C + \frac{1}{2}O_2 \rightarrow CO$	150	−151,140	−110,150	0.782	1.372

Figure 1.4 compares the fuel cell efficiency as function of temperature with the efficiency of a Carnot cycle, defined as:

$$\eta_C = \frac{T_h - T_c}{T_h} \tag{1.38}$$

It can be seen that whereas the efficiency of a fuel cell decreases with increasing temperature, the Carnot efficiency increases.

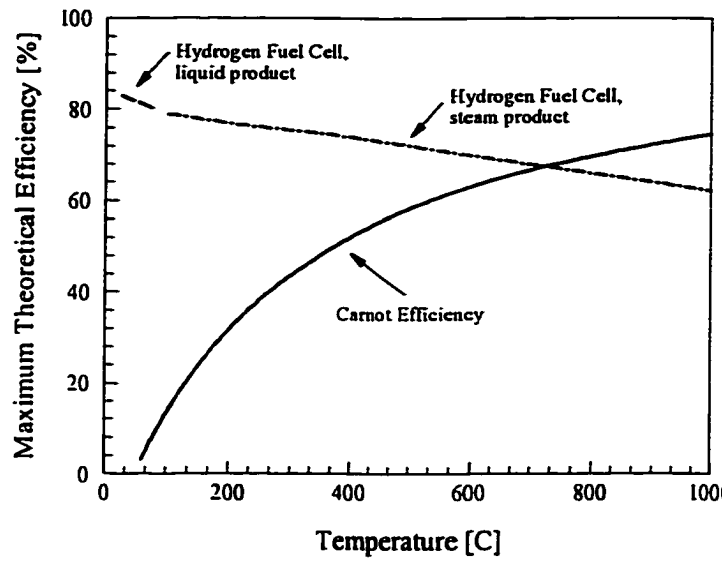

Figure 1.4: Comparison between the maximum theoretical efficiencies of a fuel cell at standard pressure with a Carnot Cycle at a lower temperature of $T_c = 50\,°C$.

At higher operating temperatures, however, the need for expensive electrocatalysts in a fuel cell is diminished because the temperature itself increases the reaction rate and hence makes the overpotential necessary for a given current density, or power, less than that for lower temperatures.

Voltage Efficiency

In the case of practically all fuel cells the terminal cell potential decreases with increasing current density drawn from the cell. As we have seen before, the main reasons for this decrease are: (1) the slowness of one or more of the intermediate steps of the reactions occurring at either or both of the electrodes, (2) the slowness of mass-transport processes, and (3) ohmic losses through the electrolyte. Under conditions where all of these forms of losses exist, the terminal cell potential is given by [11]:

$$E = E_{rev} - \eta_{act,a} - \eta_{act,c} - \eta_{conc,a} - \eta_{conc,c} - \eta_{ohm} \tag{1.39}$$

where the η's with the appropriate suffices represent the magnitudes of the losses of the first two types at the anode a and the cathode c and the third type generally in the electrolyte. The potentials expressing these losses are termed *overpotentials*. The three types of overpotentials are called *activation*, *concentration*, and *ohmic*, respectively. For a terminal voltage E, the *voltage efficiency* ϵ_e is defined as [11]:

$$\epsilon_e = \frac{E}{E_{rev}} \tag{1.40}$$

Voltage efficiencies can be as high as 0.9, and they decrease with increasing current density, owing mainly to the increasing ohmic overpotential. In the absence of faradaic losses (see below) the overall efficiency is expressed by the terminal cell voltage E via:

$$\epsilon = -\frac{nFE}{\Delta\bar{h}} \tag{1.41}$$

The Faradaic Efficiency

Another loss in a fuel cell is owing to the fact that either there is an incomplete conversion of the reactants at each electrode to their corresponding products or sometimes

the reactant from one electrode diffuses through the electrolyte and reaches the other electrode, where it reacts directly with the reactant at this electrode. The efficiency that takes this into account is termed the *faradaic efficiency*, and it is defined as [11]:

$$\epsilon_f = \frac{I}{I_{theo}} \tag{1.42}$$

I is the observed current from the cell and I_{theo} is the theoretically expected current on the basis of the amount of reactants consumed, assuming that the overall reaction in the fuel cell proceeds to completion.

Fuel Utilization

In practice, not all the fuel that is input into a fuel cell is used, because a finite concentration gradient in the bulk flow is needed to allow the reactants to diffuse towards the catalyst layer. A *fuel utilization coefficient* can be defined as [23]:

$$\mu_f = \frac{mass\ of\ fuel\ reacted\ in\ cell}{mass\ of\ fuel\ input\ to\ cell} \tag{1.43}$$

Note that this is the inverse of the *stoichiometric flow ratio*.

Overall Efficiency

The overall efficiency ϵ in a fuel cell is the product of the efficiencies worked out in the preceding subsections [11]:

$$\epsilon = \mu_f \epsilon_i \epsilon_e \epsilon_f \tag{1.44}$$

1.5 Fuel Cell Modelling: A Literature Review

Fuel cell modelling has been used extensively in the past to provide understanding about fuel cell performance. Numerous researchers have focussed on different aspects of the fuel cell, and it is difficult to categorize the different fuel cell models, since they vary in the number of dimensions analyzed, modelling domains and complexity. However, a general trend can be established. In the early 1990s most models were exclusively one-dimensional in nature, often focussing on just the gas-diffusion electrodes and the catalyst layer. From the late 1990s on, the models became more elaborate and researchers have started to apply the methods of Computational Fluid Dynamics (CFD) for fuel cell modelling. The following models should be mentioned in particular:

In 1991 and 1992, Bernardi and Verbrugge [7], [8] published a one-dimensional, isothermal model of the gas-diffusion electrodes, the catalyst layer and the membrane, providing valuable information about the physics of the electrochemical reactions and transport phenomena in these regions in general.

Also in 1991, Springer *et al.* [38], [37] at the *Los Alamos National Laboratories* (LANL) published a one-dimensional, isothermal model of the same domain, which was the first to account for a partially dehumidified membrane. To achieve this, the water content in the membrane had been measured experimentally as a function of relative humidity outside the membrane, and a correlation between the membrane conductivity and the humidification level of the membrane had been established. Since this is the only such model, it is still widely used by different authors (*e.g.* [17]), when a partly humidified membrane is to be taken into account.

Fuller and Newman [16] were the first to publish a quasi two-dimensional model of the MEA, which is based on concentration solution theory for the membrane and accounts for thermal effects. However, details of that model were not given, which makes it difficult to compare with others. Quasi two-dimensionality is obtained by solving a one-dimensional through-the-membrane problem and integrating the solutions at various points in the down-the-channel direction.

A steady-state, two-dimensional heat and mass transfer model of a PEM fuel cell was presented in 1993 by Nguyen and White [28]. This model solves for the transport of liquid water through the membrane by electro-osmotic drag and diffusion and includes the phase-change of water, but the MEA is greatly simplified, assuming "ultra-thin" gas-diffusion electrodes. The volume of the liquid phase is assumed to be negligible. This model was used to investigate the effect of different humidification schemes on the fuel cell performance. It was refined in 1998 by Yi and Nguyen [52] by including the convective water transport across the membrane, temperature distribution in the solid phase along the flow channel, and heat removal through natural convection and coflow and counterflow heat exchangers. The shortcoming of assuming ultrathin electrodes had not been addressed, so that the properties at the faces of the membrane are determined by the conditions in the channel. Again, various humidification schemes were evaluated. The same model presented in [28] was used later on by Thirumalai and White [40] to model the behaviour of a fuel cell stack. In 1999 Yi and Nguyen [53] published a two-dimensional model of the multicomponent transport in the porous electrodes of an interdigitated gas distributor [27]. The first detailed two-phase model of a PEM Fuel Cell was published by He, Yi and Nguyen in 2000 [18]. It is two-dimensional in nature and employs the inter-digitated flow field

design proposed by Nguyen [27].

In 1995 Weisbrod *et al.* [50] developed an isothermal, steady-state, one-dimensional model of a complete cell incorporating the membrane water model of Springer *et al.* This model explores the possibility of the water flux in the electrode backing layer.

More recently, Wöhr *et al.* [51] have developed a one-dimensional model that is capable of simulating the performance of a fuel cell stack. In addition, it allows for the simulation of the transient effects after changes of electrical load or gas flow rate and humidification. The modelling domain consists of the diffusion layers, the catalyst layers and the membrane, where the "dusty gas model" is applied at the diffusion layer and the transport of liquid water occurs by surface diffusion or capillary transport. For the membrane, the model previously described by Fuller and Newman [16] was used. Based on this work, Bevers *et al.* [9] conducted a one-dimensional modelling study of the cathode side only including the phase change of water.

Baschuk and Li [5] published a one-dimensional, steady-state model where they included the degree of water flooding in the gas-diffusion electrodes as a modelling parameter, which was adjusted in order to match experimental polarization curves, *i.e.* the degree of flooding was determined by a *trial and error* method.

The first model to use the methods of computational fluid dynamics for PEM Fuel Cell modelling was published by Gurau *et al.* [17]. This group developed a two-dimensional, steady-state model of a whole fuel cell, *i.e.* both flow channels with the MEA in between. The model considers the gas phase and the liquid phase in separate computational domains, which means that the interaction between both phases is not considered.

Another research group to apply the methods of CFD for fuel cell modelling is located at Pennsylvania State University. Their first publication [44] describes a two-dimensional, model of a whole fuel cell, similar to the one by Gurau *et al.*, with the exception that transient effects can be included as well in order to model the response of a fuel cell to a load change. This model is used to investigate the effect of hydrogen dilution on the fuel cell performance. The transport of liquid water through the membrane is included, however, results are not shown. Since the model is isothermal, the interaction between the liquid water and the water-vapour is not accounted for. In a separate publication [49], the same group investigates the phase change at the cathode side of a PEM fuel cell with a two-dimensional model. It is shown that for low inlet gas humidities, the two-phase regime occurs only at high current densities. A multiphase mixture model is applied here that solves for the saturation of liquid water, *i.e.* the degree of flooding.

The first fully three-dimensional model of a PEM Fuel Cell was published by a research group from the University of South Carolina, where Dutta *et al.* used the commercial software package *Fluent* (*Fluent, Inc.*). This model is very similar to the one presented in this dissertation. However, it is more complete in that it accommodates an empirical membrane model that can account for a partially dehydrated membrane. Two phase flow is also accounted for, but in a simplified fashion that neglects the volume of the liquid water that is present inside the gas-diffusion layers.

Overall it can be said that up to around 1998, most of the fuel cell models were one-dimensional, focussing on the electrochemistry and mass transport inside the MEA. In order to account for 2D and 3D effects, the methods of computational fluid dynamics have recently been successfully applied for fuel cell modelling.

1.6 Thesis Goal

The goal of this dissertation is to develop a comprehensive three-dimensional computational model of a whole PEM Fuel Cell that accounts for all major transport processes and allows for the prediction of their impact on the fuel cell performance. This model utilizes the commercial software package *CFX-4.3* (*AEA Technology*), which provides a platform for solving the three-dimensional balance equations for mass, momentum, energy and chemical species employing a finite volume discretization. Additional phenomenological equations tailored to account for processes specific to fuel cells where implemented, which required an extensive suite of user subroutines. Customized iterative procedures were also implemented to ensure effective coupling between the electrochemistry and the various transport processes.

The outline of this dissertation is as follows: Chapter 2 summarizes the three-dimensional, one-phase model and presents base case results. Chapter 3 is devoted to a detailed parametric study that was performed employing this model in order to identify parameters that are critical for the fuel cell operation. Chapter 4 describes the extension of the single phase model in order to account for multi-phase flow and phase change effects of water inside the gas diffusion layers. Results are presented in form of a base case, highlighting the physical aspects of multi-phase flow. Finally, in Chapter 5, conclusions are drawn and an outline for future work is presented.

Chapter 2

A Three-Dimensional, One-Phase Model of a PEM Fuel Cell

2.1 Introduction

This chapter describes the one-phase model that was completed in course of this thesis. The model includes the convection/diffusion of different species in the channels as well as the porous gas diffusion layers, heat transfer in the solids as well as the gases, electrochemical reactions and the transport of liquid water through the membrane. It is based on four phenomenological equations commonly used in fuel cell modelling, which are:

- the Stefan-Maxwell equations for multi-species diffusion
- the Nernst-Planck equation for the transport of protons through the membrane
- the Butler-Volmer equation for electrochemical kinetics and
- the Schlögl equation for the transport of liquid water through the membrane

In contrast with almost all of the models published in the open literature, this model accounts for non-isothermal behaviour, so that a detailed temperature distribution inside the fuel cell is part of the results.

The fact that the flux of liquid water through the MEA is accounted for might lead to the conclusion that we are dealing with a two-phase model, after all. However, it will be seen that the model treats the gas-phase and the liquid phase in separate computational domains, assuming no interaction between the phases. The reason for this is that, historically, the current model was developed based upon the one-dimensional model of Bernardi and Verbrugge [7], [8], who used a similar approach to describe the flux of liquid water through the membrane-electrode assembly. The result obtained in this model will be presented bearing in mind this shortcoming. Fortunately, at elevated temperatures such as 80 °C the volume of the liquid water is indeed quite small so that the results obtained in the parametric study are only weakly affected by neglecting the liquid water volume, as will be seen in Chapter 4.

2.2 Modelling Domain and Geometry

The modelling domain, depicted in Figure 2.1 is split up into four subdomains for computational convenience:

- The *Main Domain* accounts for the flow, heat and mass transfer of the reactant gases inside the flow channels and the gas-diffusion electrodes
- *Subdomain I* consists of the MEA only, and accounts for the heat flux through the solid matrix of the gas-diffusion electrodes and the membrane. Hence, the only variable of interest here is the temperature. Exchange terms between this

subdomain and the main domain account for the heat transfer between the solid phase and the gas phase

- *Subdomain II* is used to solve for the flux of liquid water through the membrane-electrode assembly. The flux of the water in the membrane is coupled to the electrical potential calculated in subdomain III via the so-called Schlögl equation.

- *Subdomain III* consists of the membrane only and is used to calculate the electrical potential inside the membrane.

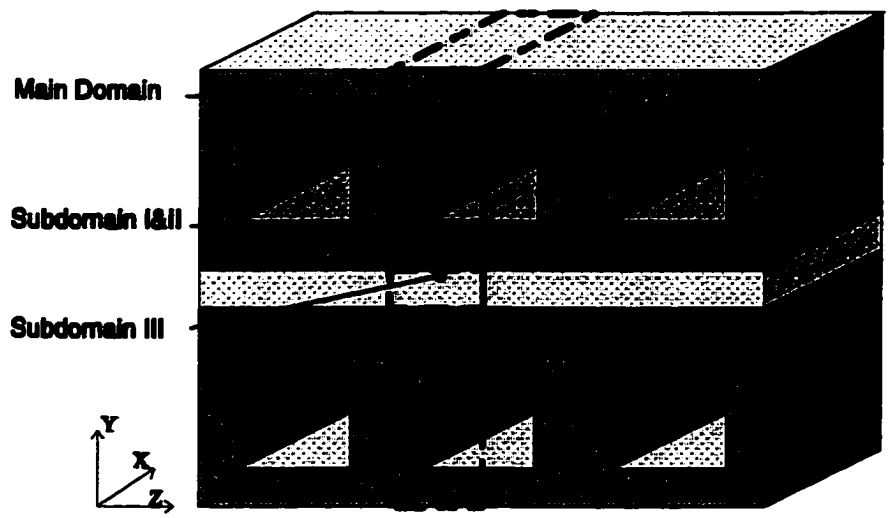

Figure 2.1: The modeling domain used for the three-dimensional model.

2.3 Assumptions

The model that is presented here is based on the following assumptions:

1. the fuel cell operates under steady-state conditions
2. all gases are assumed to be fully compressible, ideal gases, saturated with water vapour
3. the flow in the channels is considered laminar
4. the membrane is assumed to be fully humidified so that the electronic conductivity is constant and no diffusive terms have to be considered for the liquid water flux
5. Since it has been found by an earlier modelling study [8] that the cross-over of reactant gases can be neglected, the membrane is currently considered impermeable for the gas-phase
6. the product water is assumed to be in liquid phase
7. ohmic heating in the collector plates and in the gas-diffusion electrodes is neglected due to their high conductivity
8. heat transfer inside the membrane is accomplished by conduction only, *i.e.* the enthalpy carried by the net movement of liquid water is currently neglected
9. the catalyst layer is assumed to be a thin interface only where sink- and source terms for the reactants and enthalpy are specified

10. electroneutrality prevails inside the membrane. The proton concentration in the ionomer is assumed to be constant and equal to the concentration of the fixed sulfonic acid groups

11. the water in the pores of the diffusion layer is considered separated from the gases in the diffusion layers, *i.e.* no interaction between the gases and the liquid water exists

The last assumption here is the weakest and leads to a non-conservation of water. This will be addressed in a later chapter, where a two-phase model with both phases existing in the same computational domain will be described.

2.4 Modelling Equations

2.4.1 Notation

In the following, the subscript "g" denotes the gas-phase and the subscript "l" the liquid phase. For different species inside the gas phase, "i" and "j" are used, whereas the subscript "w" denotes specifically water vapour inside the gas-phase. Furthermore, "a" stands for anode side and "c" for cathode side.

2.4.2 Main Computational Domain

Gas Flow Channels

In the fuel cell channels, only the gas-phase is considered. The equations solved are the continuity equation:

$$\nabla \cdot \left(\rho_g \mathbf{u}_g\right) = 0, \tag{2.1}$$

the momentum equation

$$\nabla \cdot \left(\rho_g \mathbf{u}_g \otimes \mathbf{u}_g - \mu_g \nabla \mathbf{u}_g\right) = -\nabla \left(p + \frac{2}{3}\mu_g \nabla \cdot \mathbf{u}_g\right) + \nabla \cdot \left[\mu_g \left(\nabla \mathbf{u}_g\right)^T\right] \tag{2.2}$$

and the energy equation

$$\nabla \cdot \left(\rho_g \mathbf{u}_g h_{tot} - \lambda_g \nabla T_g\right) = 0. \tag{2.3}$$

Here ρ_g is the gas-phase density, $\mathbf{u} = (u, v, w)$ the fluid velocity, p the pressure, T the temperature, μ is the molecular viscosity, and λ is the thermal conductivity.

The total enthalpy h_{tot} is calculated out of the static (thermodynamic) enthalpy h_g via:

$$h_{tot} = h_g + \frac{1}{2}\mathbf{u}_g^2, \tag{2.4}$$

where the bulk enthalpy is related to the mass fraction y and the enthalpy of each gas by:

$$h_g = \sum y_{gi} h_{gi}. \tag{2.5}$$

The mass fractions of the different species obey a transport equation of the same form as the generic advection-diffusion equation. However, in a ternary system the

diffusion becomes more complex, because the diffusive flux now is a function of the concentration gradient of two species, i and j:

$$\nabla \cdot (\rho_g \mathbf{u}_g y_{gi}) - \nabla \cdot (\rho_g D_{gii} \nabla y_{gi}) = \nabla \cdot (\rho_g D_{gij} \nabla y_{gj}) \tag{2.6}$$

where the subscript i denotes oxygen at the cathode side and hydrogen at the anode side, and j is water vapour in both cases. The diffusion coefficients D_{gii} and D_{gij} are a function of the binary diffusion coefficients of any two species in the ternary mixture, as described in Appendix A.

As mentioned before, the gases are assumed to be fully saturated so that the molar water fraction is given by:

$$x_{gw} = \frac{p_w^{sat}(T)}{p_g} \tag{2.7}$$

The ideal gas assumption leads to:

$$\rho_{gi} = \frac{p_g M_i}{RT}, \tag{2.8}$$

with the bulk density being:

$$\frac{1}{\rho_g} = \sum \frac{y_{gi}}{\rho_{gi}} \tag{2.9}$$

The sum of all mass fractions is equal to unity

$$\sum y_{gi} = 1, \tag{2.10}$$

and the molar fraction x is related to the mass fraction by [10]:

$$x_{gi} = \frac{\frac{y_{gi}}{M_i}}{\sum_{j=1}^{n} \frac{y_{gj}}{M_j}} \tag{2.11}$$

with M_j being the molecular mass of species j.

Gas-Diffusion Layers

The equations that govern the transport phenomena in the diffusion layers are similar to the channel equations, except that the gas-phase porosity ε_g of the material is introduced in the generic advection-diffusion equation. The conservation equation for mass becomes:

$$\nabla \cdot \left(\rho_g \varepsilon_g \mathbf{u}_g\right) = 0 \tag{2.12}$$

whereas the momentum equation reduces to Darcy's law:

$$\mathbf{u}_g = -\frac{k_p}{\mu_g} \nabla p_g \tag{2.13}$$

The species transport equation in porous media becomes:

$$\nabla \cdot \left(\rho_g \varepsilon_g \mathbf{u}_g y_{gi}\right) - \nabla \cdot \left(\rho_g D_{gii} \varepsilon_g \nabla y_{gi}\right) = \nabla \cdot \left(\rho_g D_{gij} \varepsilon_g \nabla y_{gj}\right) \tag{2.14}$$

In this case, however, the binary diffusivities $\mathfrak{D}_{ij}$ that are needed for D_{gii} and D_{gij} have to be corrected for the porosity. This is often done by applying the so-called *Bruggemann correction* [33]:

$$\mathfrak{D}_{ij}^{eff} = \mathfrak{D}_{ij} * \varepsilon_g^{1.5} \tag{2.15}$$

The energy equation in the diffusion layer is:

$$\nabla \cdot \left(\rho_g \varepsilon_g \mathbf{u}_g h_{tot} - \lambda_g^{eff} \nabla T_g\right) = \beta \left(T_s - T_g\right) \tag{2.16}$$

where λ_g^{eff} is the effective thermal conductivity. The term on the right-hand side contains the source-term due to the heat exchange to and from the solid matrix of the GDL. β is a heat transfer coefficient that has the units $[\mathrm{W}/(\mathrm{K\,m^2}) \times \mathrm{m^2}/\mathrm{m^3}]$, *i.e.* it accounts for an estimated heat transfer coefficient between the solid and the gas phase as well as the specific surface area per unit volume of the GDL.

Catalyst Layers

Owing to Equation 1.1, hydrogen is oxidized at the anode side, the mechanism most likely being [46]:

$$\begin{array}{lcll} H_2 + 2M & \rightarrow & 2\left(M \cdot\cdot H\right) & \textit{slow adsorption} \\ 2\left(M \cdot\cdot H\right) & \rightarrow & 2M + 2H^+ + 2e^- & \textit{fast reaction} \end{array} \tag{2.17}$$

where "M" denotes the metal catalyst.

The local sink term for hydrogen is a function of the local current density i, according to:

$$S_{H_2} = -\frac{M_{H_2}}{2F} i \tag{2.18}$$

where M_{H_2} is the molecular weight of hydrogen and F is the Faraday constant. The factor of "2" in the above equation results from the fact that each hydrogen molecule produces two electrons.

The exact reaction mechanism for oxygen is not known, but it is believed to follow [31]:

$$\begin{array}{lcll} O_2 + M & \rightarrow & (M \cdot\cdot O_2) & \textit{fast adsorption} \\ (M \cdot\cdot O_2) + H^+ + e^- & \rightarrow & (M \cdot\cdot O_2 H) & \textit{rate-determining step} \\ (M \cdot\cdot O_2 H) + 3H^+ + 3e^- & \rightarrow & 2H_2O & \textit{via unknown, fast steps} \end{array} \tag{2.19}$$

Similar to the hydrogen depletion at the anode, the local oxygen depletion at the cathode side is described as:

$$S_{O_2} = -\frac{M_{O_2}}{4F} i \tag{2.20}$$

From the equations above, it can be seen how important it is to obtain an accurate description of the local current density i, which is given by the *Butler-Volmer equation* according to [4]:

$$i = i_0 \left[\exp\left(\frac{\alpha_a F}{RT} \eta_{act}\right) - \exp\left(-\frac{\alpha_c F}{RT} \eta_{act}\right) \right] \tag{2.21}$$

where i_0 is the apparent exchange current density, α_a and α_c are the anodic and cathodic apparent transfer coefficients, respectively, F is Faraday's constant and η_{act} is the activation overpotential. For large values of η_{act}, one of the terms on the right-hand side can be neglected. For the oxygen side, where the activation overpotential is highly negative, equation 2.21 yields:

$$i = -i_0 \left[\exp\left(-\frac{\alpha_c F}{RT} \eta_{act} \right) \right] \tag{2.22}$$

In accordance with common notation in electrochemistry, the resulting current is negative, meaning the electrons flow from the metal into the solution. The apparent exchange current density i_0, based on the geometrical area of the cell, is a function of the temperature and the reactant concentrations as well as the catalyst loading [11], and it is one of the input parameters of this model. The relation between the exchange current density and the dissolved gas concentrations at the cathode side is given by [26]:

$$i_0 = i_0^{ref} \left(\frac{C_{O_2}}{C_{O_2}^{ref}} \right)^{\gamma_{O_2}} \left(\frac{C_{H^+}}{C_{H^+}^{ref}} \right)^{\gamma_{H^+}} \tag{2.23}$$

where the concentration of the hydrogen protons can be assumed constant throughout the reaction layer so that the second term on the right-hand side is equal to unity.

From the equations above, it is important to note that for a constant surface overpotential, the local current density is a function of the local reactant concentration, for example at the cathode side it holds that:

$$i = i_{ave} \left(\frac{x_{O_2}}{x_{O_2,ave}} \right)^{\gamma_{O_2}} \tag{2.24}$$

where i_{ave} is the average current density and $x_{O_2,ave}$ is the average oxygen concentration at the catalyst layer. Hence, for a desired current density i the local current density can be obtained by knowledge of the local oxygen concentration and the average oxygen concentration at the catalyst layer.

Membrane

The membrane in the main computational domain is simply used as a separator between the anode and the cathode side. It is considered impermeable for the reactant gases. Properties of interest in the membrane are the liquid water flux, which is accounted for in subdomain II, and the electrical potential distribution, which is calculated in subdomain III. For all other purposes the membrane is considered a conducting solid that separates the electrodes (see below). Hence, no equations of interest are solved in this domain.

Bipolar Plates

The collector plates consist of graphite and serve to transfer electrons towards the gas-diffusion layers and to the reaction sites (current collectors). Currently, only heat conduction is considered in the solid plates:

$$\nabla \lambda_{gr} \cdot \nabla T_s = 0 \tag{2.25}$$

Because of the high electrical conductivity of the graphite plates Ohmic heating is neglected.

2.4.3 Computational Subdomain I

This domain is strictly used to calculate the heat transfer through the solid part of the MEA. However, various source terms have to be considered here to account for heat transfer between the gases and the solid matrix as well as ohmic heating. In detail, the following equations are being solved:

Gas-Diffusion Layers

Since this whole domain is considered a conducting solid, the only variable of interest is the temperature. The equation solved is the energy transfer equation for a solid:

$$-\nabla \cdot (\lambda_s \cdot \nabla T_s) = \beta (T_g - T_s) \tag{2.26}$$

where the term on the right-hand side accounts for the heat transfer from- and to the gas phase.

Catalyst Layer

The generation of heat in the fuel cell is due to entropy changes as well as irreversibilities associated with the charge transfer [22]:

$$\dot{q} = \left[\frac{T(-\Delta \bar{s})}{n_{e^-} F} + \eta_{act} \right] i \tag{2.27}$$

where T is the temperature, $\Delta \bar{s}$ is the entropy change in the chemical reactions, n_{e^-} is the number of electrons transferred and η_{act} is the activation overpotential. Because both terms are small at the anode side, this term is currently neglected here. η_{act} can be calculated *a priori* based on the desired current density of the cell using the Tafel equation.

When equation 2.23 is written in terms of the overpotential η_{act}, it reads as follows:

$$\eta_{act} = 2.303 \frac{RT}{\alpha_c F} \ln \left(\left| \frac{i}{i_0} \right| \right) \tag{2.28}$$

and this is the so-called *Tafel equation* [26]. The Tafel slope

$$b = 2.303\frac{RT}{\alpha_c F} \tag{2.29}$$

is inversely proportional to the apparent transfer coefficient α_c, and it has been determined experimentally to be $0.06 - 0.07\,\mathrm{V}/\mathrm{dec}$ for the cathodic fuel cell reaction [42].

Membrane

For heat transfer purposes, the membrane is considered a conducting solid, which means that the transfer of energy associated with the net water flux the membrane is neglected. However, ohmic heating due to the limited conductivity of the membrane is accounted for, according to:

$$-\nabla \cdot (\lambda_{mem} \cdot \nabla T) = \kappa |i|^2 \tag{2.30}$$

where $|i|$ is the absolute value of the local current density, according to:

$$|i| = \sqrt{i_x^2 + i_y^2 + i_z^2} \tag{2.31}$$

with:

$$\vec{i} = -\kappa \nabla \Phi \tag{2.32}$$

where κ is the protonic conductivity and Φ is the electrical potential inside the membrane.

2.4.4 Computational Subdomain II

The liquid-water domain consists of the MEA only. The equations solved here are as follows:

Gas-Diffusion Layers

The liquid water pores are considered de-coupled from the gas pores, and Darcy's law is considered for the water as well:

$$\mathbf{u}_l = -\frac{k_p}{\mu_l}\nabla p_l \tag{2.33}$$

Catalyst Layers

The product water that is being created is assumed to be in the liquid phase, and so a source term for liquid water is specified in this region:

$$S_{H_2O_{(l)}} = \frac{M_{H_2O}}{2F}i \tag{2.34}$$

Membrane

The transport of liquid water through the membrane is governed by a modified version of the Schlögl equation [35]:

$$\mathbf{u}_l = \frac{k_\phi}{\mu_l}z_f c_f F \cdot \nabla\Phi - \frac{k_p}{\mu_l}\cdot\nabla p \tag{2.35}$$

where k_ϕ and k_p denote the electric and hydraulic the permeability, respectively, z_f is the fixed-charge number in the membrane, c_f is the fixed-charge concentration, F is Faraday's constant and μ_l is the liquid water viscosity. This equation accounts for

two different water transport processes: the electro-osmotic drag, whereby hydrogen protons migrating through the membrane drag water molecules with them, and pressure driven flux, which is usually directed from the cathode side to the anode side. Strictly speaking, a diffusive term has to be accounted for as well, since the back diffusion of water plays an important role for humidification schemes. However, since the membrane is assumed to be fully humidified, this term has been dropped in the current model.

2.4.5 Computational Subdomain III

This domain is only used to calculate the electrical potential distribution inside the membrane. Currently, the membrane is considered fully humidified, which means that the electrical conductivity inside the membrane is isotropic. Bernardi and Verbrugge [7] have shown that under these conditions it holds that:

$$\nabla^2 \Phi = 0 \tag{2.36}$$

2.4.6 Cell Potential

The cell potential E is being calculated via:

$$E = E^0_{T,p} - \eta_{act} - \eta_{ohm} - \eta_{mem} \tag{2.37}$$

where $E^0_{T,p}$ is the equilibrium potential for a given temperature and pressure, η_{act} is the activation overpotential at both sides, η_{ohm} are the ohmic losses in the GDL, mainly due to contact resistances, and η_{mem} is the ohmic loss in the membrane.

The equilibrium potential $E^0_{T,p}$ can be found using the Nernst equation:

$$E^0_{T,p} = -\frac{\Delta\bar{g}^0}{2F} + \frac{\Delta\bar{s}^0}{2F}(T - T_0) + \frac{RT}{2F}\left[\ln p_{H_2} + \frac{1}{2}\ln p_{O_2}\right] \tag{2.38}$$

where the first term represents the reversible cell potential at standard temperature and pressure and the second term corrects for changes in gas pressures. Using the standard values given in Table 2.1 [25], equation 2.38 can be written as:

$$E^0_{T,p} = 1.229 - 0.83 \times 10^{-3}(T - 298.15) + 4.31 \times 10^{-5} T\left[\ln p_{H_2} + \frac{1}{2}\ln p_{O_2}\right] \tag{2.39}$$

Table 2.1: Standard thermodynamic values

Species	$\Delta\bar{g}^0_{fi}$ [J / mol]	$\Delta\bar{s}^0$ [J / (mol K)]
$H_2O_{(l)}$	-237,180	69.95
$H_{2(l)}$	0	130.57
$O_{2(l)}$	0	205.03

Provided the transfer coefficients α_a and α_c are known, the activation overpotentials η_{act} on both sides can be calculated using the Tafel equation, equation 2.28. It is well known that due to the much higher exchange current density on the anode side, the activation overpotential here is much lower than on the cathode side.

The ohmic losses in the GDL, η_{ohm}, can be calculated as:

$$\eta_{ohm} = \frac{i}{\sigma_{eff}} t_e \tag{2.40}$$

where i is the nominal current density of the cell and σ_{eff} is the electric conductivity of the diffusion layer and t_e is its thickness.

The membrane loss η_{mem} is related to the fact that an electric field is necessary in order to maintain the motion of the hydrogen protons through the membrane . This field is provided by the existence of a potential gradient across the cell, which is directed in the opposite direction from the outer field that gives us the cell potential, and thus has to be substracted. It can be shown that this loss obeys Ohm's law [29]:

$$\eta_{mem} = I R_{mem} \tag{2.41}$$

where I is the total cell current in [A] and R is the electrical resistance of the membrane in [Ω].

2.5 Boundary Conditions

Boundary conditions have to be applied at all outer interfaces of the computational domains. In the z-direction of all interfaces, symmetrical boundary conditions have been applied. By doing so, we are assuming an infinite number of identical, parallel channels, which is the simplest approach for a three-dimensional model. Further boundary conditions are given as follows:

2.5.1 Main Computational Domain

For the main computational domain, the inlet values at the anode and cathode inlet are prescribed for the velocity, temperature and species concentrations (*Dirichlet boundary conditions*).

The inlet velocity is a function of the desired current density i, the geometrical area of the membrane A_{MEA}, the channel cross-section area A_{ch}, and the stoichiometric

flow ratio ζ, according to:

$$u_{in} = \zeta \frac{i}{nF} A_{MEA} \frac{1}{x_{i,in}} \frac{RT}{p_{in}} \frac{1}{A_{ch}} \tag{2.42}$$

where n_{elec} is the number of electrons per mole of reactant, *i.e.* $n = 4$ for oxygen at the cathode side and $n = 2$ for hydrogen. R is the universal gas constant, T is the inlet temperature, $x_{i,in}$ is the molar fraction of the reactants O_2 and H_2 of the incoming humid gases and p_{in} is the static pressure.

At the outlets of the gas-flow channels, only the pressure is being prescribed as the desired electrode pressure; for all other variables, the gradient in the flow direction is assumed to be zero (*Neumann Boundary Conditions*). At the boundaries in the x-direction of the MEA, zero normal gradients are prescribed as well as zero normal fluxes of any transported parameter ϕ:

$$\frac{\partial \phi}{\partial x} = 0 \tag{2.43}$$

Since the fluid channels are bordered by the collector plates, no boundary conditions have to be prescribed at the channel/solid interface. At the outer boundaries of the bipolar plates (y-direction), boundary conditions need only to be given for the energy equation. This can be done in form of either a heat flux or a temperature value, or a mixture of the above. Currently, symmetry is assumed at the outer y-boundaries, leading to a no-heat-flux boundary condition:

$$\frac{\partial T}{\partial y} = 0 \tag{2.44}$$

By doing so we are modelling an endless number of fuel cells stacked together in a cathode-to-cathode and anode-to-anode fashion, which is obviously not physical. However, this approximation only influences the temperature distribution, which in turn has only a limited effect on the fuel cell performance, especially because the temperature rise is fairly small and locally constrained to the MEA, as we will see in the results section.

2.5.2 Computational Subdomain I

In the conducting solid region boundary conditions only need to be applied for the energy equation. This is a difficult task, since the exact boundary condition depends on the gas velocity inside the gas flow channels. To simplify this, adiabatic boundary conditions are being applied at all boundaries of this domain, which means that energy transfer takes only place to- and from the gas-phase. Mathematically this can be expressed as:

$$\frac{\partial T}{\partial n} = 0 \tag{2.45}$$

where n is the direction perpendicular to all boundaries.

2.5.3 Computational Subdomain II

For the liquid water transport through the MEA in the subdomain I, the pressure is given at the outer boundaries of the GDL, *i.e.* the channel/GDL interface:

$$p_{a,l} = p_a \tag{2.46}$$

and

$$p_{c,l} = p_c \tag{2.47}$$

As can be seen, the pressure inside the channels is assumed constant in these boundary conditions. This has been done, because preliminary computations indicated that the pressure drop in the flow channels is very small and can indeed be neglected without a loss of accuracy.

2.5.4 Computational Subdomain III

Finally, for the electrical potential equation, the potential is arbitrarily set to zero at the anode side:

$$\Phi = 0 \tag{2.48}$$

and at the cathode side, the potential distribution at the membrane/catalyst interface is given by [8]:

$$\frac{\partial \Phi}{\partial y} = -\frac{1}{\kappa}[i - F c_f v] \tag{2.49}$$

where κ is the protonic conductivity of the membrane, i is the local current density, F is Faraday's constant, c_f is the fixed-charge concentration inside the membrane, v is the y-component of the liquid water velocity.

2.6 Computational Procedure

2.6.1 Discretization Method

The equations listed in the preceding chapter are not solved by the CFX solver in their differential form. Instead, the finite volume method is applied, which uses the integral form of the conservation equations as a starting point. The integration of the transport equations results in linearized equations. In order to solve these, the solution domain is subdivided into a finite number of contiguous control volumes (CV's), and the conservation equations are applied to each CV. At the centroid of each CV lies a computational node at which the variable values are calculated. Interpolation is used to express variable values at the CV surface in terms of the nodal (CV-center) values.

The complete set of equations is not solved simultaneously (in other words by a *direct method*). Quite apart from the excessive computational effort which it would entail, this approach ignores the non-linearity of the underlying differential equations. Therefore iteration is used at two levels: an inner iteration to solve for the spatial coupling of each variable and an outer iteration to solve for the coupling between variables. Thus each variable is taken in sequence, regarding all other variables as fixed, a discrete transport equation for that variable is formed for every cell in the flow domain and the problem is handed over to the linear equation solver which returns the updated values of the variable. The non-linearity of the original equations is simulated by reforming the coefficients of the discrete equations, using the most recently calculated values of the variables, before each outer iteration. Figure 2.2 shows the order in which the equations are solved.

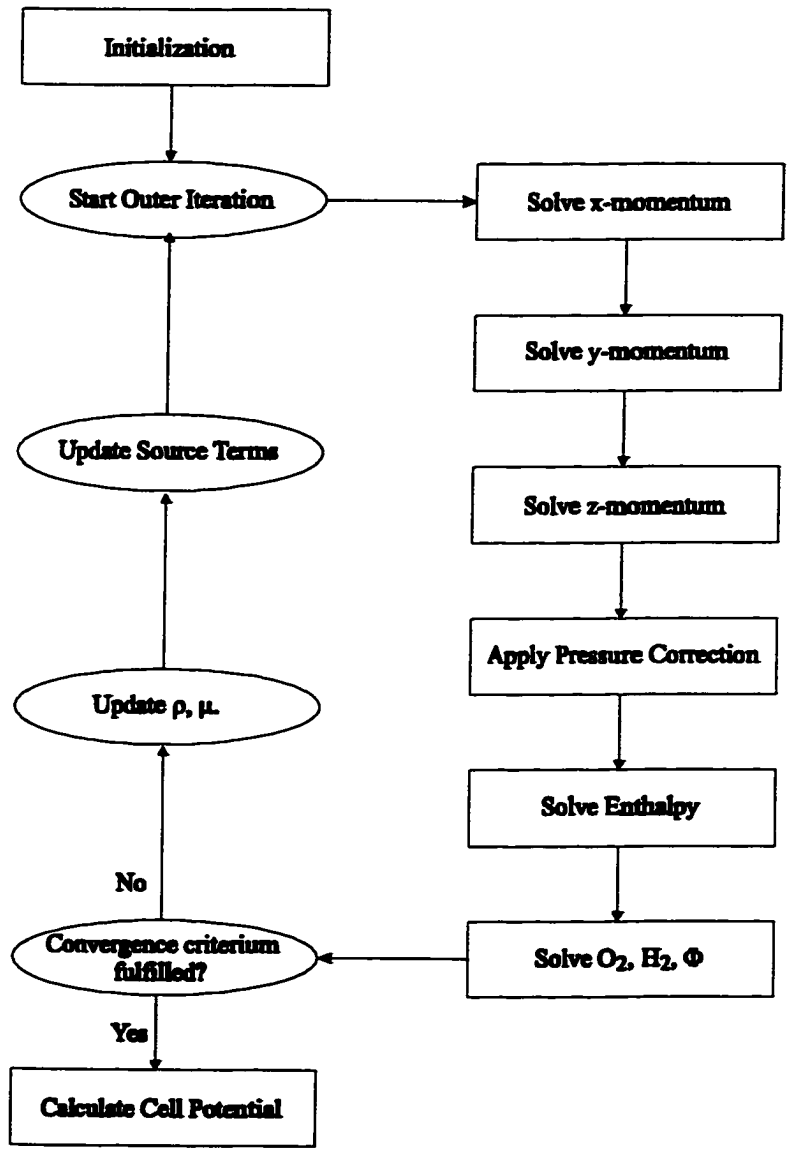

Figure 2.2: Flow diagram of the solution procedure used.

The Inner Iteration

The set of linearized difference equations for a particular variable, one equation for each control volume in the flow, is passed to a simultaneous linear equation solver which uses an iterative solution method. An exact solution is not required because this is just one step in the non-linear outer iteration. *CFX* offers a variety of linear equation solvers, and each equation for each phase can be iterated using a different solution method. Table 2.2 summarizes the different methods used in the current model [1].

Table 2.2: Selected linear equation solvers

Equation	Method	MNSL	MXSL	RDFC
U	Full field Stone's method	1	5	0.25
V	Full field Stone's method	1	5	0.25
W	Full field Stone's method	1	5	0.25
P	Algebraic Multi-grid	1	30	0.1
H	Algebraic Multi-grid	1	5	0.25
Scalar Eq.	Full field Stone's method	1	5	0.25

The parameters which control the solution process are a minimum number of iterations (MNSL), a maximum number of iterations (MXSL) and a residual reduction factor (RDFC), the residual in a particular cell being the amount by which the linear equation there is not satisfied. The values used for each of these parameters is also shown in Table 2.2. For more information about the different solvers, the interested reader is referred to [1].

2.6.2 Computational Grid

The computational grid that was used for the main modelling domain is shown in Figure 2.3. Only shown is the grid for the gas flow channel and the MEA, the grid of the bipolar plates has been left out for reasons of clarity. The total number of grid cells amounted to roughly 80,000. This relatively coarse grid is owing to the high computational requirement of this problem. The computations presented here were performed on a *Pentium II* processor with 450 MHz.

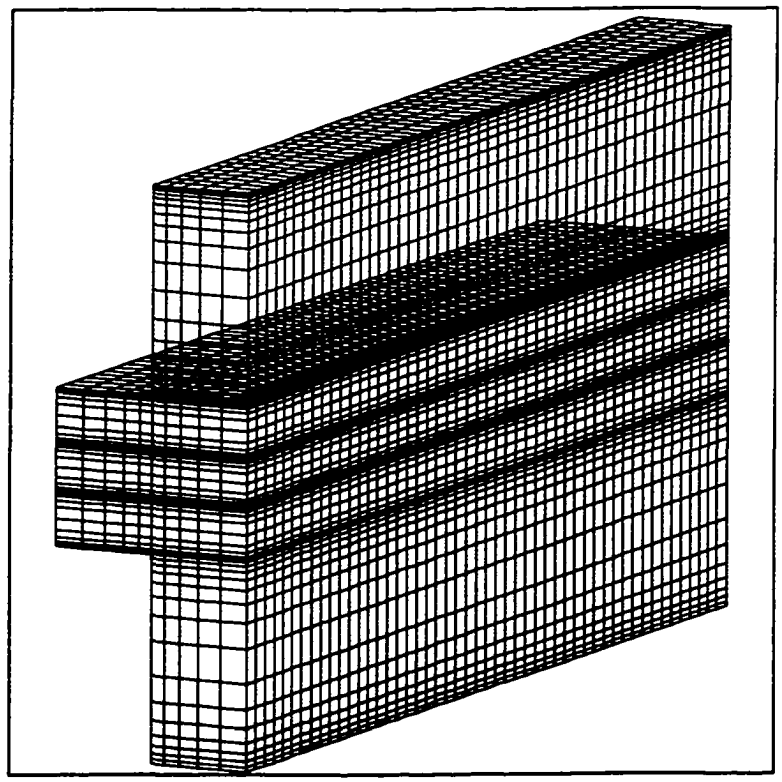

Figure 2.3: Numerical grid of the main computational domain.

2.7 Modelling Parameters

Among the most tedious parts of model development is the determination of the correct parameters for the model, which will eventually determine the accuracy of the results. Since the fuel cell model that is presented in this thesis accounts for all basic transport phenomena simply by virtue of its three-dimensionality, a proper choice of the modelling parameters will make it possible to obtain good agreement with experimental results obtained from a 'real' fuel cell. Therefore, much effort went into finding modelling parameters that are as realistic as possible.

Table 2.3 shows the basic dimensions of the computational domain. Because the basic model has been developed to identify and quantify basic transport phenomena that occur during the operation of a fuel cell, only a straight channel section is considered for now. All parameters listed in Table 2.3 refer to both sides, anode and cathode. The membrane thickness is taken from [8], and it refers to a fully wetted *Nafion 117* membrane.

Table 2.3: Physical dimensions of the base case

Parameter	Symbol	Value	Unit
Channel length	l	0.05	m
Channel height	h	$1.0 * 10^{-3}$	m
Channel width	w_{ch}	$1.0 * 10^{-3}$	m
Land area width	w_l	$1.0 * 10^{-3}$	m
Electrode thickness	t_e	$0.26 * 10^{-3}$	m
Membrane thickness	t_{mem}	$0.23 * 10^{-3}$	m

Table 2.4 gives the basic operational parameters for our fuel cell model. All these were taken from Bernardi and Verbrugge [7, 8], who used the experimental data of Ticianelli *et al.* [42] as their base case. The stoichiometric flow ratio for the experiments was not reported.

Table 2.4: Operational parameters at base case conditions

Parameter	Symbol	Value	Unit
Inlet fuel and air temperature	T	80	°C
Air side pressure	p_c	5	atm
Fuel side pressure	p_a	3	atm
Air stoichiometric flow ratio	ζ_c	3	–
Fuel stoichiometric flow ratio	ζ_a	3	–
Relative humidity of inlet gases	ξ	100	%
Oxygen/Nitrogen ratio	ψ	0.79/0.21	–

Electrode properties for the base case are listed in Table 2.5. The effective thermal conductivity λ_{eff} has been taken from an expression given by Gurau *et al.* [17]:

$$\lambda_{eff} = -2\lambda_{gr} + \frac{1}{\frac{\varepsilon}{2\lambda_{gr}+\lambda_g} + \frac{1-\varepsilon}{3\lambda_{gr}}} \tag{2.50}$$

where the thermal conductivity of the graphite matrix is $\lambda_{gr} = 150.6\,\mathrm{W/(m\,K)}$. Since the conductivity of the gases is several orders of magnitude lower, it has been neglected and the expression above can be simplified to:

$$\lambda_{eff} = \left(\frac{6}{\varepsilon+2} - 2\right)\lambda_{gr} \tag{2.51}$$

Table 2.5: Electrode properties at base case conditions

Parameter	Symbol	Value	Unit	Ref.
Electrode porosity	ε	0.4	–	[8]
Hydraulic permeability	k_p	$4.73 * 10^{-19}$	m^2	[8]
Electronic conductivity	σ	6000	S / m	assumed
Effective thermal conductivity	λ_{eff}	75.3	W / (m K)	[17]
Transfer coefficient, anode side	α_a	0.5	–	–
Transfer coefficient, cathode side	α_c	1	–	[42]
An. ref. exchange current density	$i_{0,a}^{ref}$	0.6	A / cm^2	[48]
Cath. ref. exchange current density	$i_{0,c}^{ref}$	$4.4 * 10^{-7}$	A / cm^2	[42]
Oxygen concentration parameter	γ_{O_2}	1	–	[31]
Hydrogen concentration parameter	γ_{H_2}	1/2	–	[17]
Entropy change of cathode reaction	$\Delta\bar{s}_{Pt}$	−326.36	J / (mol K)	[22]
Heat transfer coefficient	β	$1.0 * 10^8$	W / m^3	assumed

The reference exchange current density i_0^{ref} is one of the most sensitive parameters in this model, since it determines the activation overpotential that is necessary to obtain a certain current density. It depends on a number of factors such as catalyst loading and localization, Nafion loading in the catalyst layer [42], reactant concentrations and temperature [29]. The values cited here are within physical limits, and they can easily be adjusted, *i.e.* for the modelling of different catalyst loadings. Fortunately, a wealth of data is available by now in the open literature (e.g. [32], [31]).

The heat transfer coefficient between the gas phase and the solid matrix of the electrodes β has been found by *trial-and-error*. It has been adjusted so that the tem-

perature difference between the solid and the gas-phase is minimal, *i.e.* below 0.1 K throughout the whole domain. This is equivalent to assuming thermal equilibrium between the phases. The low velocity of the gas-phase inside the porous medium and the high specific surface area which accommodates the heat transfer justify this assumption.

For the gas-pair diffusivities in the Stefan-Maxwell equations listed in Table 2.6, experimentally determined values were taken and scaled for the temperature and pressure, according to [13]:

$$\mathfrak{D}_{ij}^{eff} = \mathfrak{D}_{ij}\left(T_0, p_0\right) \frac{p}{p_0} \left(\frac{T}{T_0}\right)^{1.75} \tag{2.52}$$

Table 2.6: Binary diffusivities at 1atm at reference temperatures

Gas-Pair	Reference Temperature	Binary Diffusivity
	T_0 [K]	D_{ij} [cm^2 / s]
$\mathfrak{D}_{H_2-H_2O}$	307.1	0.915
$\mathfrak{D}_{H_2-CO_2}$	298.0	0.646
$\mathfrak{D}_{H_2O-CO_2}$	307.5	0.202
$\mathfrak{D}_{O_2-H_2O}$	308.1	0.282
$\mathfrak{D}_{O_2-N_2}$	293.2	0.220
$\mathfrak{D}_{H_2O-N_2}$	307.5	0.256

Table 2.7 lists the membrane properties taken for the base case. The membrane type is *Nafion 117*. Bernardi and Verbrugge [8] developed the following theoretical expression for the electric conductivity of the membrane:

$$\kappa = \frac{F^2}{RT} z_f \mathfrak{D}_{H^+} c_f \tag{2.53}$$

This expression leads however to an over-estimation of the conductivity compared to experimentally determined results, which range between 0.03 and 0.06 S / cm for an ambient humidity of 100% [30]. In this work, a value of 0.068 S / cm was taken for the ionic conductivity of the membrane, which agrees with the value used by Springer *et al.* [38].

Table 2.7: Membrane properties

Parameter	Symbol	Value	Unit	Ref.
Ionic conductivity	κ	0.068	S / cm	[38]
Protonic diffusion coefficient	$\mathfrak{D}_{H^+}$	$4.5 * 10^{-9}$	m^2 / s	[8]
Fixed-charge concentration	c_f	1,200	mol / m^3	[8]
Fixed-site charge	z_f	-1	$-$	[8]
Electrokinetic permeability	k_ϕ	$7.18 * 10^{-20}$	m^2	[8]
Hydraulic permeability	k_p	$1.8 * 10^{-18}$	m^2	[8]
Thermal conductivity	λ	0.67	W / (m K)	[19]

Because the Nafion membrane consists of a Teflon backbone, filled with liquid water, the thermal conductivity of the membrane can be estimated. The thermal conductivity λ of water is 0.67 W / (m K) [19], whereas Teflon has a value of around 0.4 W / (m K) at a temperature of 350 K [19]. Both values are in the same range, and the value of water was taken for the current simulations.

2.8 Base Case Results

2.8.1 Validation Comparisons

In order to establish the accuracy of the numerical simulations, comparisons have to be made with experimental results, where the first (and in many cases only) output is the polarization curve. The results obtained in this model are being compared with experimental results by Ticianelli *et al.* [42] and in a later chapter with data from Kim *et al.* [20].

Ticianelli *et al.* [42] modelled their experimental results with an equation of the form:

$$E = E_0 - b\log(i) - r_i i \tag{2.54}$$

which models the obtained polarization curves and gives insight into the electrode kinetic parameters for the oxygen reduction reaction and the ohmic losses. b in this expression is the Tafel slope and r_i is the internal resistance of the cell. The assumptions made in this equation are that mass transport limitations and activation overpotential at the hydrogen electrode are negligible.

Kim *et al.* [20] fitted their data to the following expression that also accounts for the mass transport overpotential:

$$E = E_0 - b\log(i) - r_i i - m\exp(ni) \tag{2.55}$$

where m and n were obtained through curve-fitting and are associated with mass transport losses at high current densities.

E_0 in the above equations is a constant and can be expressed by:

$$E_0 = E_r + b\log(i_0) \tag{2.56}$$

where E_r is the reversible cell potential for the cell and i_0 is the exchange current density for the oxygen reduction reaction. Putting equations 2.54 and 2.56 together yields the equation for the polarization curves neglecting mass transport overpotentials and activation losses at the hydrogen electrode:

$$E = E_r - b\log\left(\frac{i}{i_0}\right) - r_i i \tag{2.57}$$

where the logarithmic term can be recognized as corresponding to the Tafel equation. Table 2.8 gives an example of the data presented by Ticianelli *et al.* [42]. Note that the catalyst loading is 0.35 mg Pt/cm^2 for both PEM 21 and PEM 45.

Table 2.8: Experimental curve-fit data

Cell no.	Cell type	p [atm]	T [°C]	E_0 [V]	i_0 [A/cm^2]	b [V/dec]	r_i
PEM 21	H_2/Air	3/5	50	0.933	110×10^{-9}	0.072	0.23
PEM 21	H_2/Air	3/5	75	0.945	277×10^{-9}	0.070	0.25
PEM 45	H_2/Air	3/5	50	0.928	20×10^{-9}	0.062	0.69
PEM 45	H_2/Air	3/5	80	0.935	104×10^{-9}	0.065	0.39

Figure 2.4 compares the results of the model at base case conditions with the experimental results obtained by Ticianelli *et al.* [42]. The agreement between the modelling results and experiments is good, especially for the low and intermediate current densities. The increasing discrepancies in the cell potential towards high current

densities can be explained by mass transport limitations, which are not considered in the empirical curve described by equation 2.57, but which were included in the modelling results. This means that a comparison can only be made in the low and intermediate current density regions (up to $\approx 1.0\,\mathrm{A}/\mathrm{cm}^2$). In addition, there is a small deviation in the slope of the linear section in the polarization curves, which indicates that the protonic conductivity of the electrolyte membrane is slightly under-estimated in the model. Finally, it has to be stated that the exact conditions of the experiments, *e.g.* the stoichiometric flow ratios used, channel geometries and electrode thickness were not given, which makes it impossible to make definite quantitative comparisons. What is important to note is that the current three-dimensional model gives realistic results without *ad-hoc* adjustment to any of the parameters.

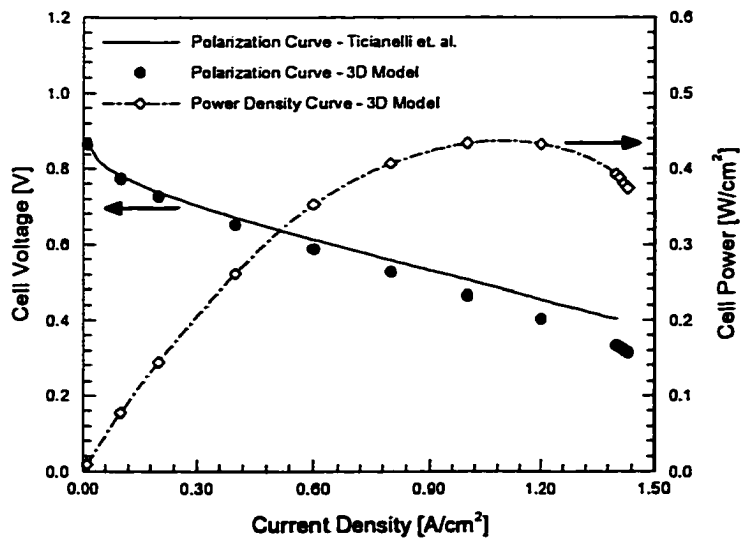

Figure 2.4: Comparison of polarization curves and power density curves between the 3D modelling results and experiments.

In general, it is possible to obtain good agreement between a model and experimental polarization curves with most models. Even the earlier one-dimensional model of the MEA developed by Bernardi and Verbrugge [8] resulted in excellent agreement between model and experiment with the adjustment of a single parameter. In the model presented here, all the parameters are within physical limits, which will allow us to conduct a systematic study on the importance of a single parameter on the fuel cell performance. Whenever possible, experimental results will be shown as comparison, but it has to be borne in mind that for the experiments that are published the exact conditions are not given. Furthermore, experiments are confined to polarization data, and detailed *in-situ* measurements are virtually non-existent.

One of the advantages of a comprehensive fuel cell model is that it allows for the assessment of the different loss mechanisms, which is shown in Figure 2.5.

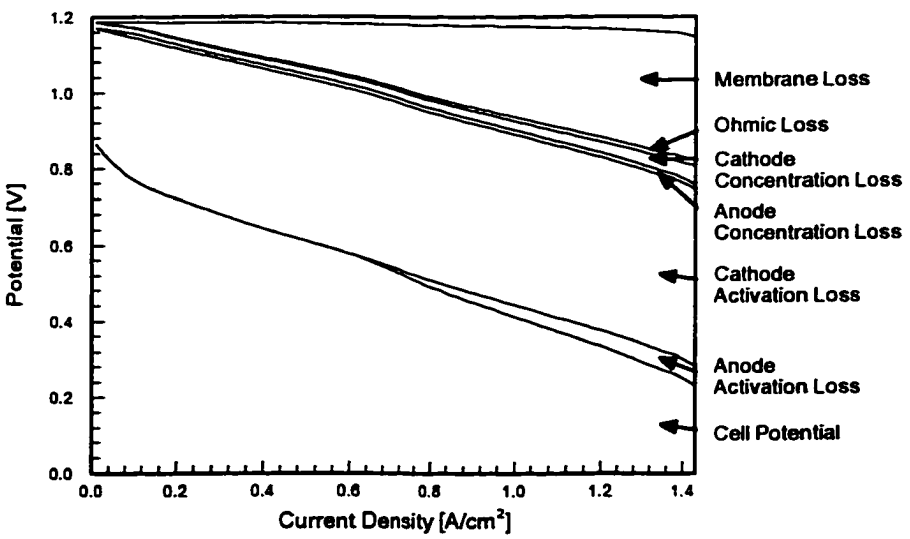

Figure 2.5: The break-up of different loss mechanisms at base case conditions.

Due to the transfer coefficient of $\alpha = 0.5$ for the anode side reaction, the anodic activation loss increases relatively fast once the cell current density exceeds the exchange current density of the anodic reaction. However, it should be possible to alleviate anodic activation losses with improved catalyst deposition.

The most important loss mechanism is the activation overpotential at the cathode side, which also has to be addressed with improved catalyst deposition techniques. At high current densities, the membrane loss becomes significant. It can be seen that due to its ohmic nature, it increases linearly with increasing current density.

The cathode concentration loss is quantitatively small, until the oxygen concentration approaches zero at the limiting current density. Because the numerical solution procedure can result in unrealizable negative mass fractions, when performing simulations in this region, the mass transport limitation regime can not be well resolved.

2.8.2 Reactant Gas and Temperature Distribution Inside the Fuel Cell

Due to the relatively low diffusivity of the oxygen compared to the hydrogen, the cathode operating conditions usually determine the limiting current density when the fuel cell is run on humidified air. This is because an increase in current density corresponds to an increase in oxygen consumption. The concentration of oxygen at the catalyst layer is balanced by the oxygen that is being consumed and the amount of oxygen that diffuses towards the catalyst layer, driven by the concentration gradient. Therefore, we will, for the most part, limit the presentation of results mainly to the cathode side of the fuel cell.

Figure 2.6 shows the reactant gas distribution inside the gas channels and attached porous gas-diffusion electrodes at a low current density. The depletion of the reactant gases from the inlet (front) towards the outlet as well as the distribution of the reactant gases inside the porous electrodes (wider parts of the "T") is clearly illustrated.

This plot demonstrates the effect of the land area between two parallel channels on the gas distribution. Due to the higher diffusivity of the hydrogen the decrease in molar concentration under the land areas is smaller than for the oxygen; the lowest ratio between the minimum hydrogen concentration at the catalyst layer and the bulk hydrogen concentration being 0.44/58. According to

$$i_0 = \left(\frac{c_{H_2}}{c^{\infty}_{H_2}}\right)^{1/2} \tag{2.58}$$

the local current density varies of the square root of the local concentration of hydrogen [17, 44]. The result is a fairly even distribution of the local current density on the anode side.

This is different at the cathode side, where the lower diffusivity of the oxygen along with the low concentration of oxygen in ambient air results in a noticeable oxygen depletion under the land areas. Since, in addition, the local current density of the cathode side reaction depends directly on the oxygen concentration ($\gamma = 1$) [31], this means that the local current density distribution under the land areas is much smaller than under the channel areas, especially near the outlet.

This is even more pronounced at higher current densities, as Figure 2.7 demonstrates. The gradients of the reactant gas distribution are steeper inside the diffusion

layers, and the oxygen concentration is less than 2% throughout the entire catalyst interface. Under the land areas it is almost zero, indicating that the limiting current density has almost been reached. From this plot it becomes clear that the diffusion of the oxygen towards the catalyst layer is the main impediment for reaching high current densities.

The molar oxygen concentration at the catalyst layer is shown in Figure 2.8. It is interesting to note that the formation of the shoulders under the land areas is strongest in the medium current density region. At a low current density, the oxygen consumption rate is low enough not to cause diffusive limitations, whereas at a high current density the concentration of oxygen under the land areas has already reached near-zero values and can not further decrease.

The temperature distribution inside the fuel cell for these current densities is shown in Figure 2.10. Naturally, the maximum temperature occurs, where the electrochemical activity is highest, which is near the cathode side inlet area. However, the temperature increase for low current densities is small, only $1\,\mathrm{K}$. We will see below that for low- and intermediate current densities the local current density distribution is fairly even, which keeps the heat release small.

This is different for high current densities. A much larger fraction of the current is being generated near the inlet of the cathode side under the channel, as will be shown in Chapter 2.8.3, and this leads to a significantly larger amount of heat being generated here. The maximum temperature is more than $4\,\mathrm{K}$ above the gas inlet temperature and it occurs inside the membrane. The gases leave the computational domain at slightly elevated temperatures, *i.e.* at around $353.6\,\mathrm{K}$ at $0.4\,\mathrm{A}/\mathrm{cm}^2$ and

at 355 K at 1.4 A / cm^2. However, it has to be borne in mind that this computational domain presents only a small fraction of a complete cell, where serpentine channels might be several orders of magnitude longer than the section investigated here, so that in a real fuel cell the gases would heat up more significantly.

Overall, the temperature rise inside a fuel cell might be quite significant, and can not be neglected. On the other hand, one of the most prominent effects on the temperature field, the heat of evaporation and condensation, was not accounted for in these computations, since the amount of water undergoing phase-change was not known. Phase change has a significant impact on the temperature distribution inside the fuel cell, and vice versa, as will be shown with the extended model in Chapter 4.

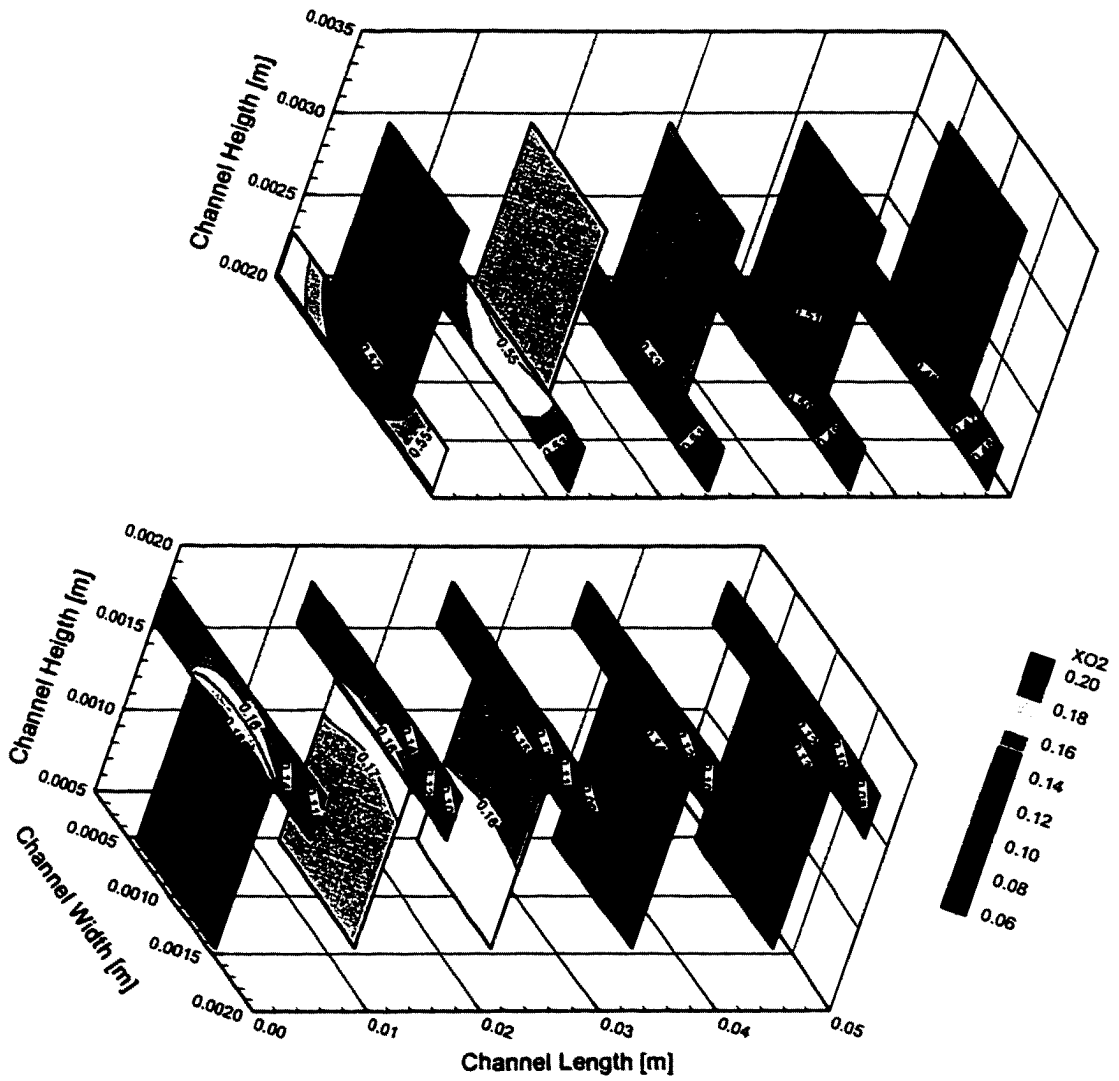

Figure 2.6: Reactant gas distribution in the anode channel and GDL (upper) and cathode channel and GDL (lower) at a nominal current density of $0.4\,\mathrm{A/cm^2}$ at base case conditions.

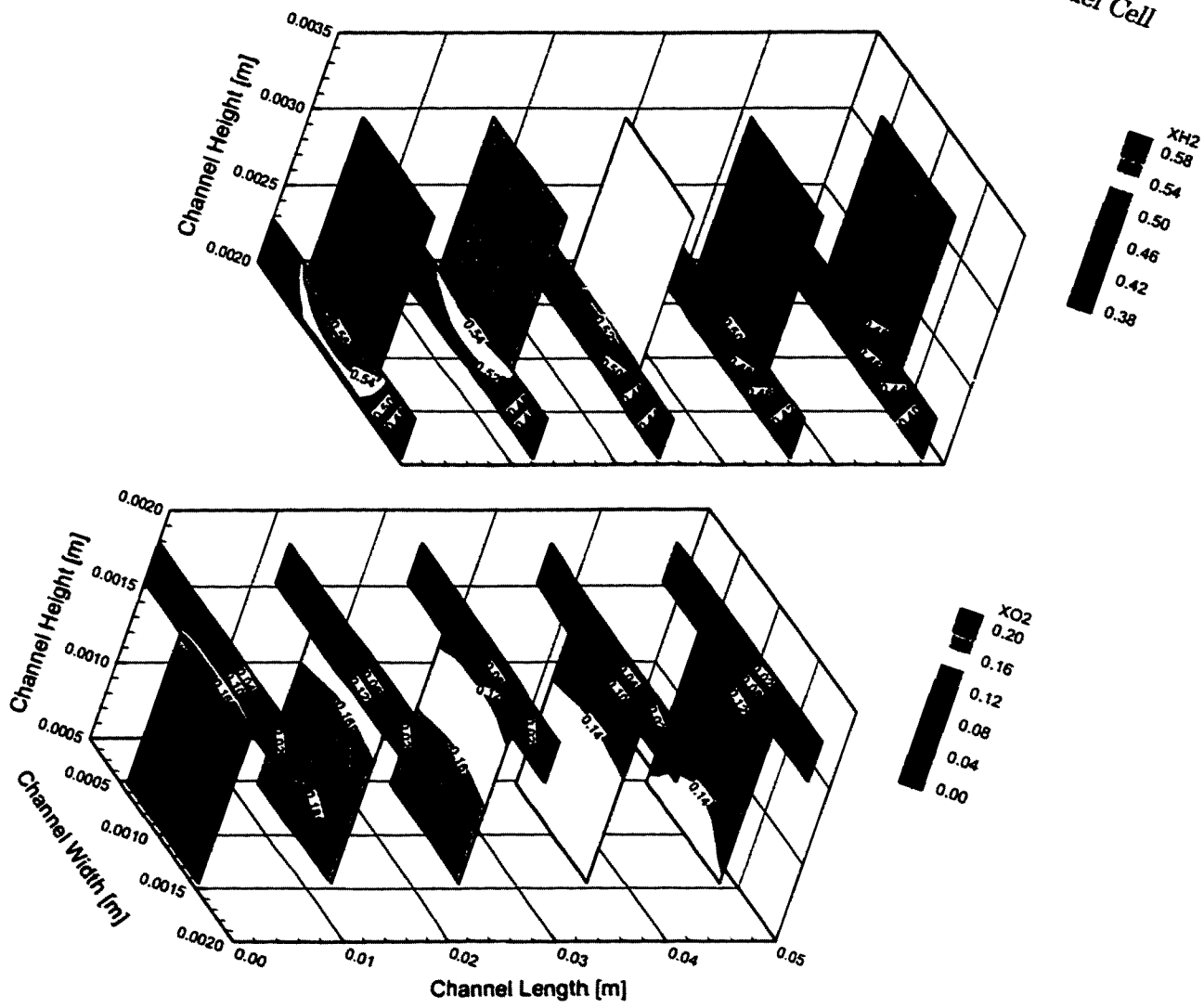

Figure 2.7: Reactant gas distribution in the anode channel and GDL (upper) and cathode channel and GDL (lower) at a nominal current density of $1.4\,A/cm^2$ at base case conditions.

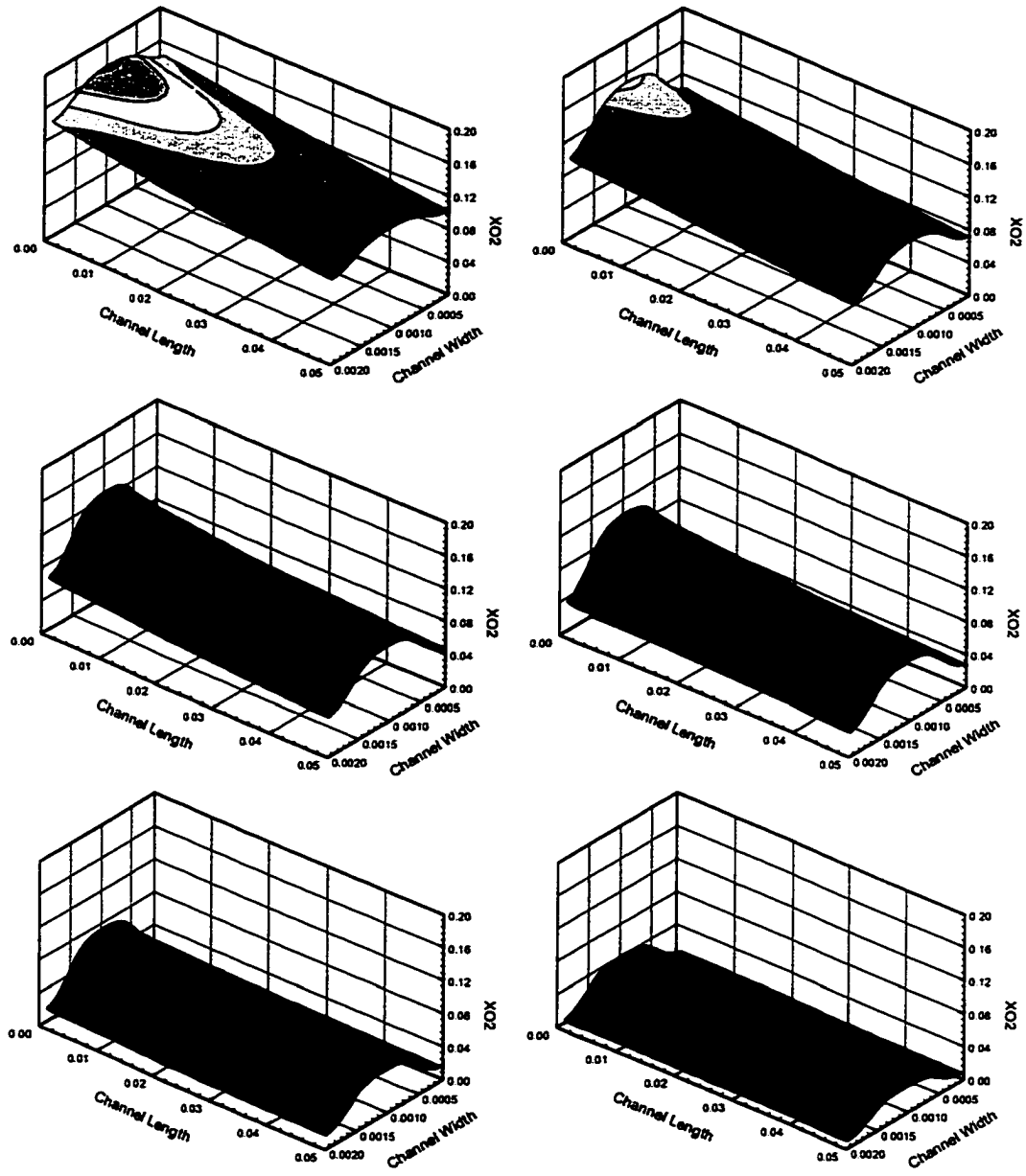

Figure 2.8: Molar oxygen concentration at the catalyst layer for six different current densities: $0.2\,\mathrm{A/cm^2}$ (upper left), $0.4\,\mathrm{A/cm^2}$ (upper right), $0.6\,\mathrm{A/cm^2}$ (centre left), $0.8\,\mathrm{A/cm^2}$ (centre right), $1.0\,\mathrm{A/cm^2}$ (lower left) and $1.2\,\mathrm{A/cm^2}$ (lower right).

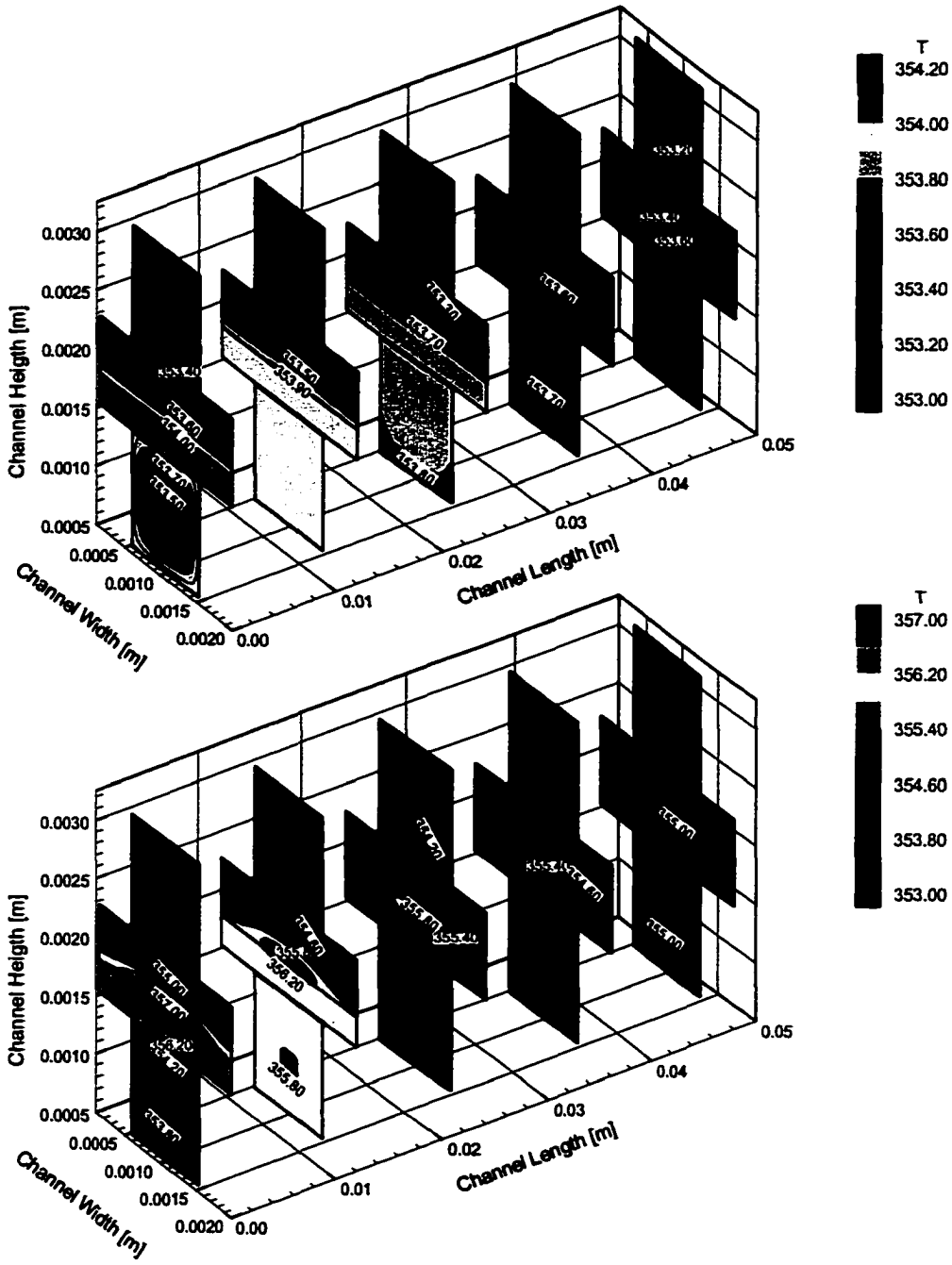

Figure 2.9: Temperature distribution inside the fuel cell at base case conditions for two different nominal current densities: $0.4\,\mathrm{A/cm^2}$ (upper) and $1.4\,\mathrm{A/cm^2}$ (lower).

2.8.3 Current Density Distribution

It was noted before that one of the most critical variables for fuel cell modelling is the local current density distribution. Once the detailed distribution of the reactant gas at the catalyst is obtained with the model, it is possible to determine the local current density distribution, assuming an even catalyst loading throughout the cell and a constant activation overpotential.

Figure 2.10 shows the local current density distribution at the cathode side catalyst layer for three different nominal current densities: $0.2\,\mathrm{A/cm^2}$, $0.8\,\mathrm{A/cm^2}$ and $1.4\,\mathrm{A/cm^2}$. For the sake of comparison, the local current density has been nominalized by divided through the average current density. It can be seen that for a low nominal current density the local current is evenly distributed, the maximum being just about 20% higher and the minimum 20% lower than the average (nominal) current density. The result is an evenly distributed heat generation, as we have seen before.

An increase in the nominal current density to $0.8\,\mathrm{A/cm^2}$ leads to a more pronounced distribution of the local current, and the maximum can exceed the average current density by more than 70% at the cathode side inlet, the minimum being 50% below the average. Further increase in the current leads to a more extreme current distribution inside the cell.

For an average current density of $1.2\,\mathrm{A/cm^2}$, a high fraction of the current is generated at the catalyst layer that lies beneath the channels, leading to an underutilization of the catalyst under the land areas.

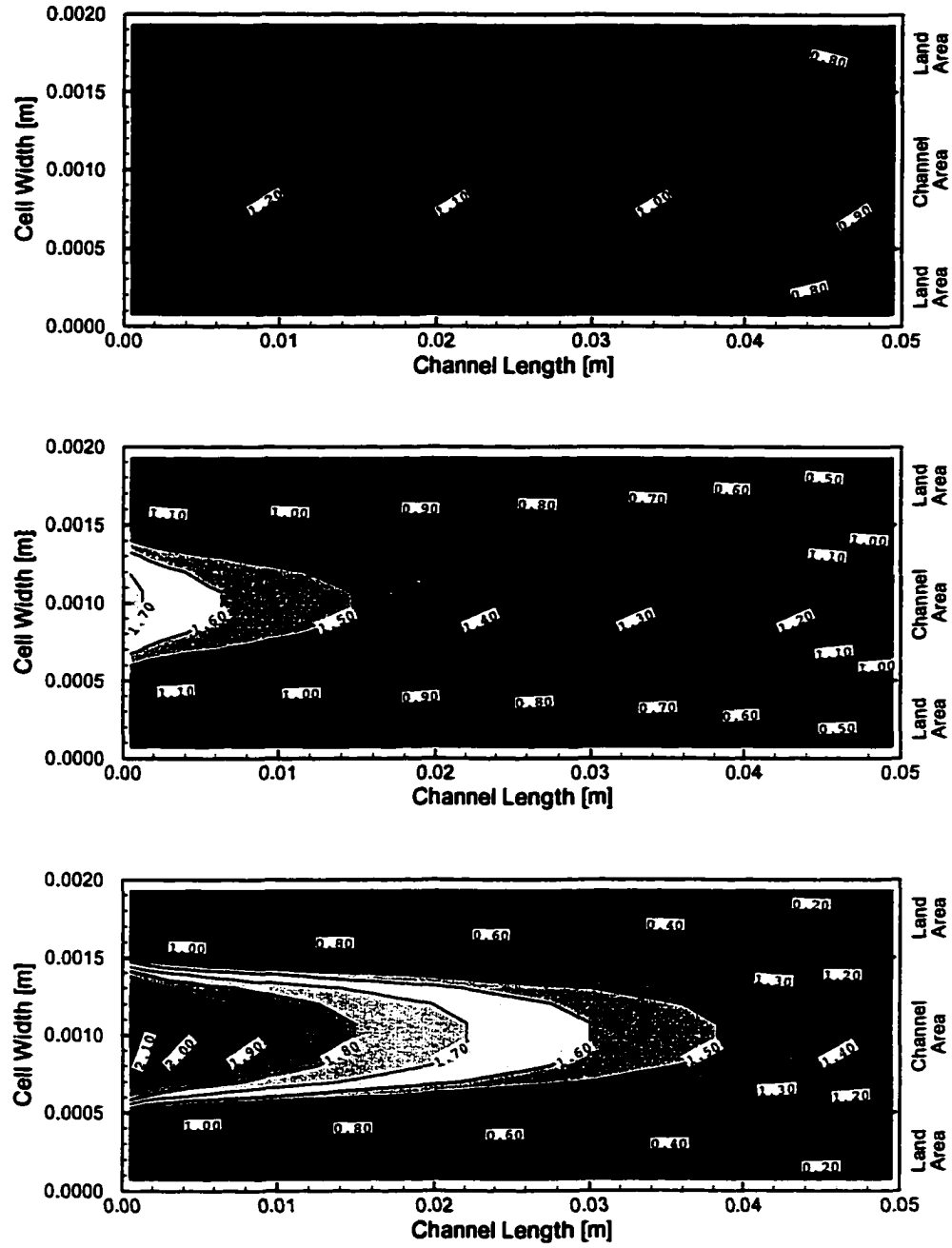

Figure 2.10: Dimensionless current density distribution i/i_{ave} at the cathode side catalyst layer for three different nominal current densities: 0.2 A / cm^2 (upper), 0.8 A / cm^2 (middle) and 1.4 A / cm^2 (lower).

The resulting ratio of the overall current that is being generated under the channel area is shown in Figure 2.11. At a low current density, around 50% of the total current is generated under the channel area. This, however, increases rapidly in an almost linear manner as the current density increases, and the maximum reaches nearly 80% at the limiting current density. Overall, the simulations suggest a more effective catalyst utilization can be achieved with a non-uniform catalyst distribution, by depositing a larger fraction of the catalyst under the land area and towards the outlet of the fuel cell.

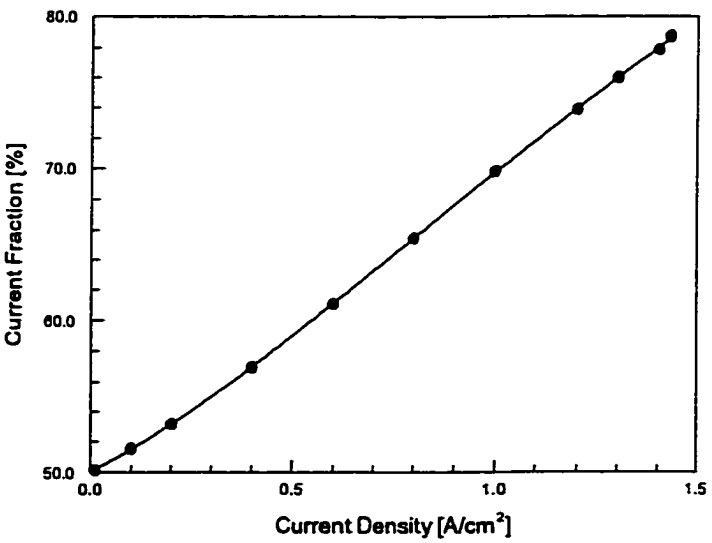

Figure 2.11: Fraction of the total current generated under the channel area as opposed to the land area.

2.8.4 Liquid Water Flux and Potential Distribution in the Membrane

The current model assumes a fully humidified membrane. In reality, the membrane is prone to partly dehumidify at the anode side [38], which leads to a non-isotropic electrical conductivity of the membrane. Nevertheless, the results for the water flux and the electrical potential distribution in the membrane shall be briefly discussed here.

Figure 2.12 shows the flow vectors of the liquid water through the membrane and the electrical potential distribution in the membrane for three different current densities. The liquid water flux is governed by two effects: the convection due to the pressure differential across the membrane and the electro-osmotic drag associated with the transport of hydrogen protons from the anode to the cathode side. As the electro-osmotic drag follows the direction of the electric current in the membrane and the current is perpendicular to the iso-lines of the electrical potential, the drag is also in the direction perpendicular to the electrical potential isolines.

At a low current density of $0.1\,\mathrm{A}/\mathrm{cm}^2$, the pressure gradient outweighs the effect of the electro-osmotic drag, and so the net water flux is directed towards the anode almost throughout the entire domain. Since the current is fairly uniformly distributed at the cathode side at low current densities, the electrical potential gradient is relatively constant in the z-direction.

When the current density is increased to $0.2\,\mathrm{A}/\mathrm{cm}^2$, the effect of the electro-osmotic drag in the membrane starts to outweigh the effect of the pressure gradient,

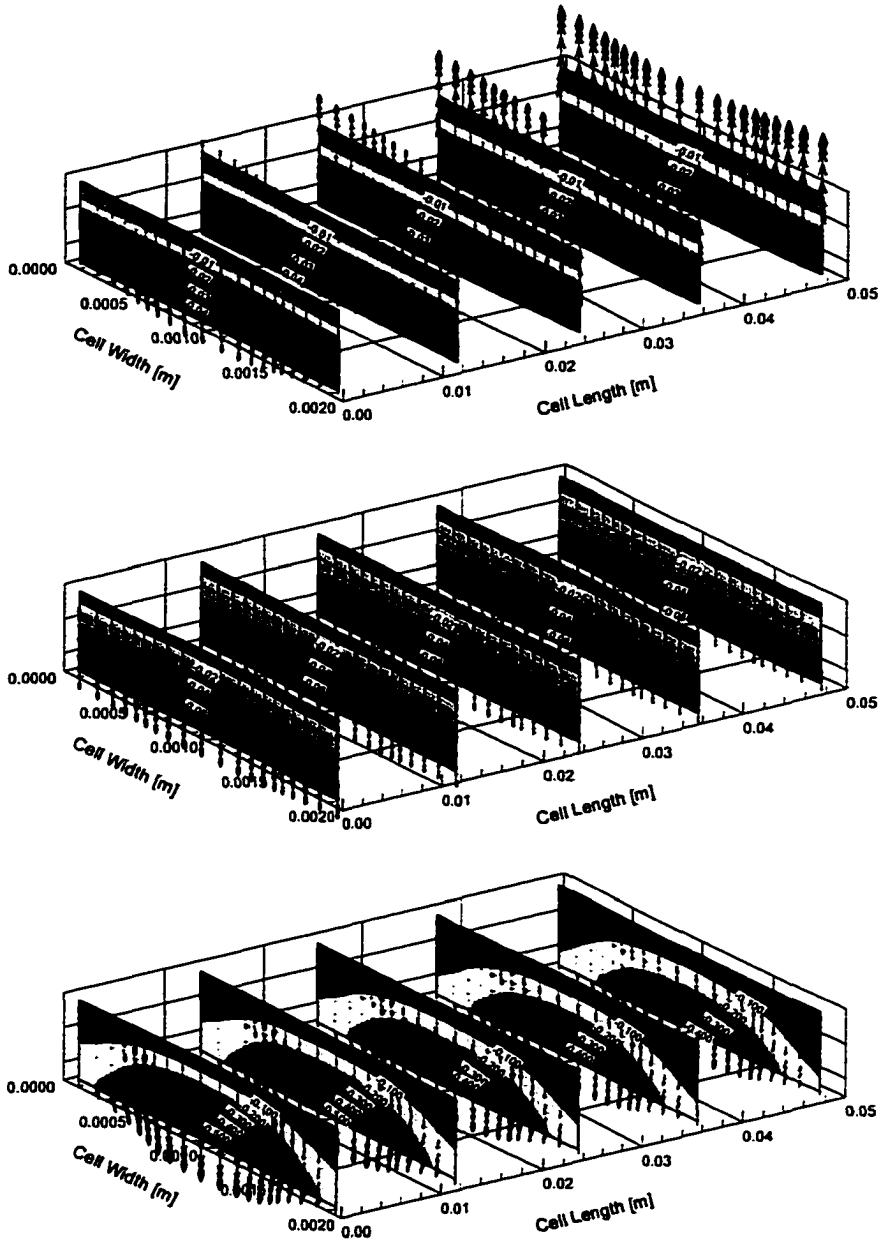

Figure 2.12: Liquid water velocity field (vectors) and potential distribution (contours) inside the membrane at base case conditions for three different current densities: $0.1\,\mathrm{A/cm^2}$ (upper), $0.2\,\mathrm{A/cm^2}$ (middle) and $1.2\,\mathrm{A/cm^2}$ (lower). The vector scale is $200\,\mathrm{cm/(m/s)}$, $20\,\mathrm{cm/(m/s)}$, and $2\,\mathrm{cm/(m/s)}$, respectively.

and the liquid water flux is directed from the anode side to the cathode side throughout the entire domain. The iso-potential lines are more and more curved around the area between the fuel cell channels, as can be seen for the current density of $1.2\,\mathrm{A}/\mathrm{cm}^2$. This is due to the high local current densities in these areas.

It is important to note that the current density, at which the electro-osmotic drag starts outweighing the pressure gradient, depends entirely on the modelling parameters used in the Schlögl equation, *i.e.* the electrokinetic permeability k_Φ and the hydraulic permeability k_p of the membrane, both of which are difficult to determine. The values used in the current calculations stem from [8], where $k_\Phi = 7.18 \times 10^{-20}\,\mathrm{m}^2$ and $k_p = 1.8 \times 10^{-18}\,\mathrm{m}^2$. Gurau *et al.* [17] used an electrokinetic permeability of $k_\Phi = 11.3 \times 10^{-20}\,\mathrm{m}^2$ and a hydraulic permeability of $k_p = 1.58 \times 10^{-18}\,\mathrm{m}^2$ in their two-dimensional model, and their results predict that for otherwise similar conditions the direction of the liquid water flux changes between $0.8\,\mathrm{A}/\mathrm{cm}^2$ and $0.9\,\mathrm{A}/\mathrm{cm}^2$. In both cases we note that the region, where the net water flux inside the membrane changes direction, is confined to a small current density range.

Another comparison can be made with the modelling results by Nguyen *et al.* [28], [52]. This group described the water flux inside the membrane by (i) electro-osmotic drag, (ii) back-diffusion by the concentration gradient of water created by the electro-osmotic flow from the anode side to the cathode side and the cathode side reaction and (iii) convection by the pressure gradient between the anode side and the cathode side of the channels:

$$\vec{N}_{w,mem} = n_d \frac{\vec{i}}{F} - \mathcal{D}_w \nabla c_w - c_w \frac{k_p}{\mu_w} \nabla p \tag{2.59}$$

where n_d is the electro-osmotic drag coefficient, *i.e.* the number of water molecules

dragged by each hydrogen proton that migrates through the membrane and $\mathcal{D}_w$ is the diffusion coefficient of water in the membrane. Note the similarity of this equation with the well-established Nernst-Planck equation [4]:

$$\vec{N}_i = -z_i \frac{F}{RT} \mathcal{D}_i c_i \nabla \Phi - \mathcal{D}_i \nabla c_i + c_i \vec{v} \tag{2.60}$$

Appendix B shows, how these expressions compare to the Schlögl equation. In order to compare the results presented here with the model presented by Nguyen *et al.*, the electrokinetic permeability of the membrane in this model has to be adjusted to $k_\Phi = 2.0 \times 10^{-20}\,\mathrm{m}^2$.

Figure 2.13 compares the modelling results for the net drag coefficient α for both values of the electrokinetic permeability k_Φ. α is defined as the net number of water molecules that crosses the membrane per hydrogen proton. Reducing the electrokinetic permeability leads to a decrease of α from values around $3.0 - 4.6$ to values below 1.0. The current density, where the water flux changes direction has increased from around $0.1\,\mathrm{A}/\mathrm{cm}^2$ to $0.4\,\mathrm{A}/\mathrm{cm}^2$.

For comparison, the α-values obtained by Yi and Nguyen [52] are in the order of $0.6 - 0.8$ at a current density of $1.1\,\mathrm{A}/\mathrm{cm}^2$, and a pressure gradient of 1 atm and a value between 0.8 and 1.0 in the absence of a pressure gradient. By adjusting the electrokinetic permeability we have obtained α-values that are of the same order of magnitude.

Experimental values for the net drag coefficient α have been obtained by Choi *et al.* [12], who found that for current densities of $0.2\,\mathrm{A}/\mathrm{cm}^2$ and higher, the value is constant at around 0.3. At lower current densities, however, the net drag coefficient

increases up to 0.55 at $0.06\,\mathrm{A/cm^2}$, which must be attributed to the back-diffusion. The experiments were conducted without a pressure gradient using humidified H_2 and O_2 as reactant gases.

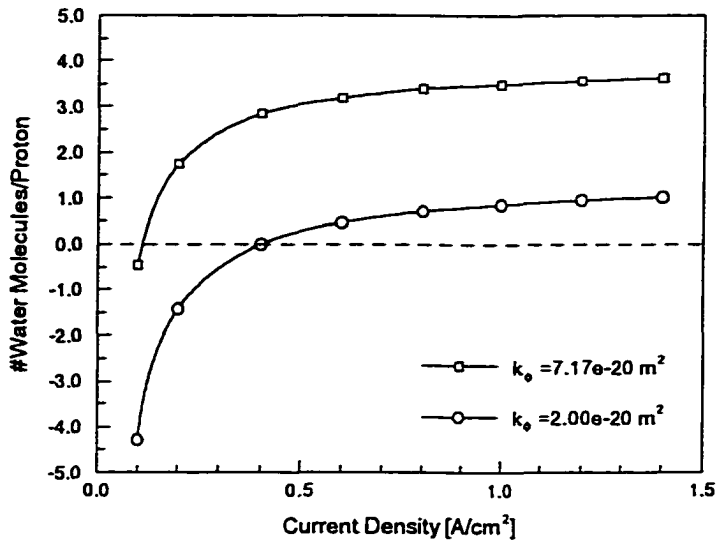

Figure 2.13: Comparison of values for the net drag coefficient α for two different values of the electrokinetic permeability of the membrane.

Overall, the Schlögl equation does not appear to be sufficient to describe the flux of liquid water through the membrane. The parameters used in the equations proved to be critical, yet difficult to determine. This will have to be addressed in future extensions of this model. For the overall model evaluation, however, the water management is not critical, because most of the experiments that we compare our result with have been conducted under controlled conditions with humidified inlet gases so that the membrane was indeed fully humidified.

2.8.5 Grid Refinement Study

Because the conservation equations listed above in Chapter 2.4 are solved in their finite-difference form, the discretization of the differential equations on the grid should become exact as the grid spacing tends to zero. The difference between the discretized equation and the exact one is called the *truncation error.* It is usually estimated by replacing all the nodal values in the discrete approximation by a Taylor series expansion about a single point. As a result one recovers the original differential equation plus a reminder, which represents the truncation error. For a method to be *consistent*, the truncation error must become zero when the mesh spacing $\Delta x_i \rightarrow 0$ [15]. Truncation error is usually proportional to a power of the grid spacing Δx [15]. Consistency of the numerical method alone is not sufficient in order to obtain a *converged solution.* In addition, the method has to be *stable*, which means that the method used does not magnify the errors that appear in the course of numerical solution process. For an iterative method as it is used here, a stable method is one that does not diverge [15].

A numerical method is said to be *convergent* if the solution of the discretized equations tends to the exact solution of the differential equation as the grid spacing tends to zero. In order to check the convergence of a non-linear problem like the one we are dealing with, convergence can only be investigated by numerical experiments, *i.e.* repeating the calculation on a series of successively refined grids. If the method is stable and all approximations used in the discretization process are consistent, we will find that the computation does converge to a *grid-independent solution.*

In order to investigate this, the grid that has been shown in Figure 2.3 has been refined twice by adding 20% of the cells and 40% of the cells in every direction,

respectively, leading to a 73% and a 174% finer grid overall. The computations at base case conditions were repeated on these refined grids, and the solutions compared.

The polarization curves obtained with the refined grids are shown in Figure 2.14, left. It is almost impossible to distinguish the three different lines, which is also true for the average molar oxygen fraction at the catalyst layer, shown on the right hand side of Figure 2.14. This indicates that in terms of the fuel cell performance the base case grid provides adequate resolution.

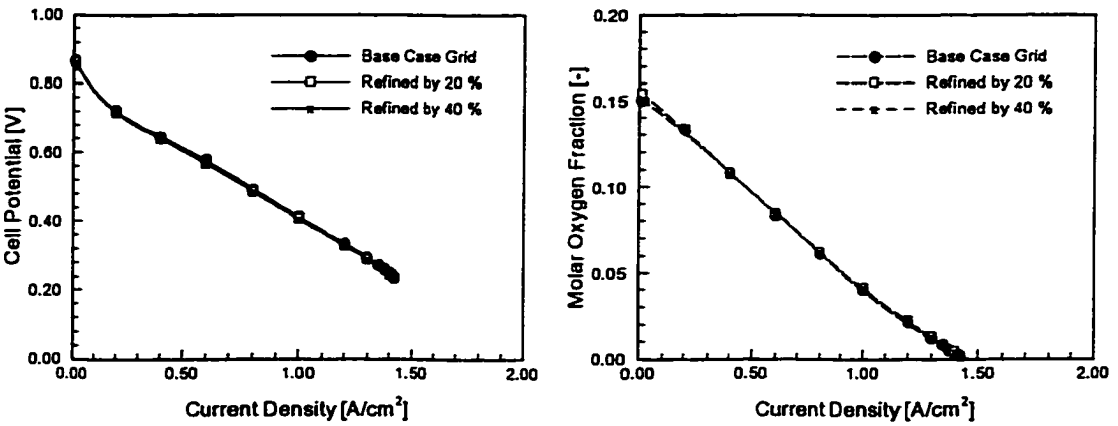

Figure 2.14: Polarization curves (left) and molar oxygen fraction at the catalyst layer as a function of the current density (right) for three different grid sizes.

The local current density distribution at the cathodic catalyst layer for the three different numerical grids is shown in Figure 2.15. Also shown is the grid used in every case (white lines). Note that the y-axes are scaled by a factor of 10 compared to the x-axes. The differences in the current density distribution are very small. A the inlet area at mid-channel the local current density is slightly higher for the coarse grid. Apart from that, no differences can be observed.

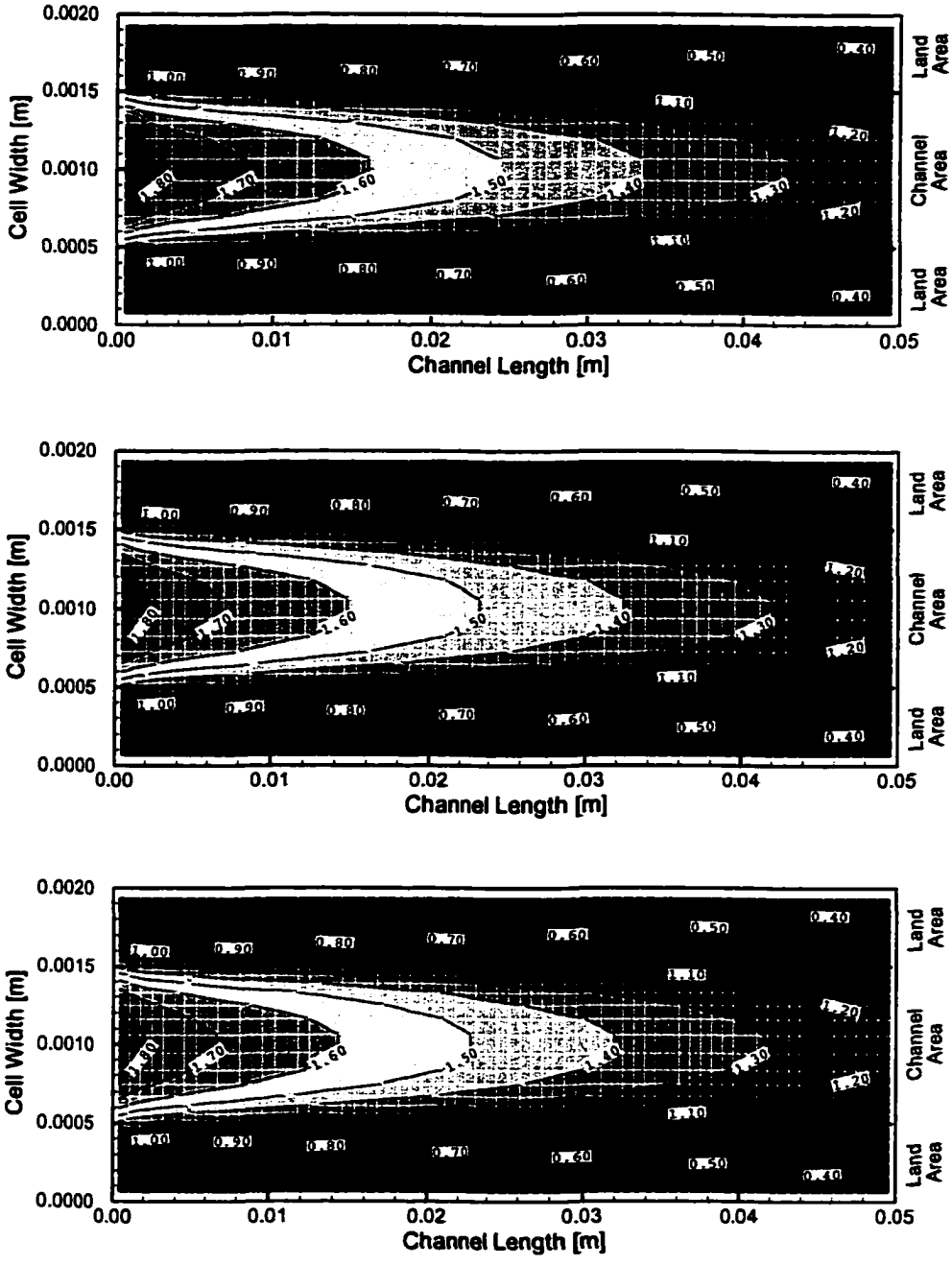

Figure 2.15: Local current distribution at the catalyst layer for three different grid sizes: Base Case (upper), 120%× Base Case (middle) and 140%× Base Case (lower). The nominal current density is $1.0\,\mathrm{A}/\mathrm{cm}^2$.

The computational cost (iterations per second) increases linearly with the number of grid cells. For the base case grid it takes about 26 seconds per iteration, which increases to roughly 45 seconds per iteration for the 73% finer grid, and to 70 seconds per iteration using the finest grid with 174% more cells than the base case, as is shown in Figure 2.16. All simulations were performed on a *Pentium II* processor with 450 MHz. Given the essentially grid-independent solution obtained with the base case grid and the impracticality of performing a large number of parametric simulations with the finer grids, the base case grid was employed for all simulations presented in the following chapter.

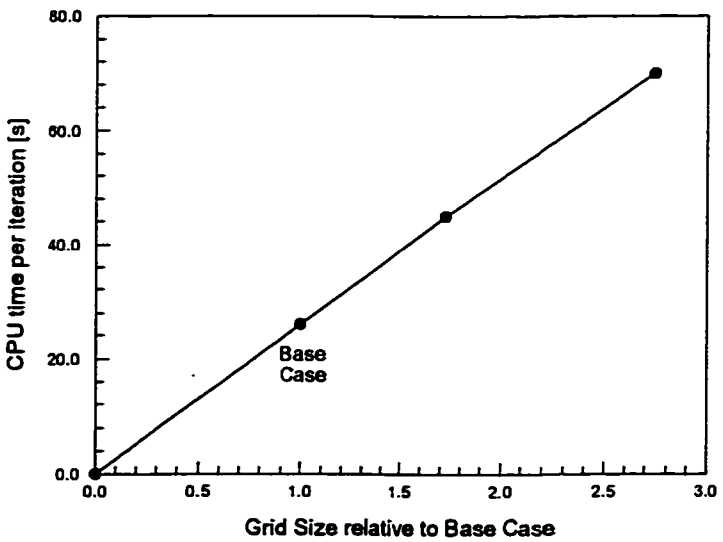

Figure 2.16: Computational cost associated with grid refinement.

2.8.6 Summary

A three-dimensional computational model of a PEM Fuel Cell has been presented in this chapter. The complete set of equations was given, and the computational procedure, based on the commercial software package *CFX 4.3*, was outlined. The results of the base case show good agreement with experimentally obtained data, taken from the literature. A detailed distribution of the reactants and the temperature field inside the fuel cell for different current densities were presented. Water management issues for the polymer membrane were addressed. A grid refinement study revealed that already for the coarsest grid that was used the solution proofed to be grid-independent.

This model can be used to provide fundamental understanding of the transport phenomena that occur in a fuel cell, and furthermore provide guidelines for fuel cell design and prototyping. The following chapter will focus on a parametric study employing the model presented here that was conducted in order to better understand and ultimately predict the fuel cell performance under various operating conditions. Operational, geometrical as well as material parameters were systematically varied in order to assess their effect on the fuel cell performance.

Chapter 3

A Parametric Study Using the Single-Phase Model

3.1 Introduction

Next, a parametric study was conducted to (*i*) identify the critical parameters for fuel cell performance, and (*ii*) determine the sensitivity of the model to various parameters and hence identify which of these need to be specified more accurately. In order to do so, only one parameter was changed from the base case conditions at a time. Care had to be taken on how other modelling parameters depend on the parameter that was changed, *i.e.* the temperature influences all other transport parameters inside the fuel cell, ranging from the diffusivities of the species to the speed of the electrochemical reactions, and this had to be taken into account. Only three aspects of the results will be emphasized during this chapter:

i. the *limiting current density*, which is reached when then oxygen consumption at the catalyst layer can just be balanced by the supply of oxygen via diffusion.

In contrast to a two-dimensional model, the three-dimensional model presented here is capable of making predictions about the limiting current density that can be reached for the different geometries investigated. As will be seen in a later chapter, the amount of spacing between the single fuel cell channels (land area) has a strong impact on the onset of mass transport limitations, which can not be captured by a two-dimensional model.

ii. the *fuel cell performance* in form of the polarization curves or power density curves. Since the electrical power of the fuel cell is equal to the product of the current density and the electrical potential, the polarization curve is equivalent to the power density curve and vice versa. However, in some cases, the results become clearer when considering the power density curve and in others the polarization curves reveal more information.

iii. the *local current density distribution at the catalyst layer*. For an optimum fuel cell performance and in order to avoid large temperature gradients inside the fuel cell, it is desirable to achieve a uniform current density distribution inside the cell.

The parameters investigated include the operating temperature and pressure, stoichiometric flow ratio, oxygen concentration of the incoming cathode stream, the porosity and thickness of the GDL and the ratio between the channel width and the land area.

3.2 Effect of Temperature

The temperature basically affects all the different transport phenomena inside the fuel cell. Predominantly affected are:

- the *composition of the incoming gas streams.* Assuming the inlet gases are fully humidified, the partial pressure of water vapour entering the cell depends on the temperature only. Thus, the molar fraction of water vapour is a function of the total inlet pressure and temperature, and so the molar fraction of the incoming hydrogen and oxygen depend on the temperature and pressure as well.

- the *exchange current density* i_0. The exchange current density of an electrochemical reaction depends strongly on the temperature. Parthasarathy *et al.* [32] conducted experiments in order to determine a correlation between the cell temperature and the exchange current density of the oxygen reduction reaction.

- the *membrane conductivity* κ. A higher temperature leads also to a higher diffusivity of the proton in the electrolyte membrane, thereby reducing the membrane resistance.

- the *reference potential* E_0. Although Equation 2.39 shows a decrease in the reference potential with an increasing temperature, experimental results indicate an increase, which can be explained with a higher diffusivity of the hydrogen with increasing temperature [32].

- the *gas-pair diffusivities* $\mathfrak{D}_{ij}$ in the Stefan-Maxwell equations. An increase in temperature leads to an increase in the gas-pair diffusivities.

In order to determine the inlet gas composition as a function of temperature, the following relation between the temperature and the saturation pressure of water has been used [38]:

$$\log_{10} p_{sat} = -2.1794 + 0.02953 \times \vartheta - 9.1837E-5 \times \vartheta^2 + 1.4454E-7 \times \vartheta^3 \quad (3.1)$$

where ϑ is the temperature in [°C]. The molar fraction of water vapour in the incoming gas stream is simply the ratio of the saturation pressure and the total pressure:

$$x_{H_2O,in} = \frac{p_{sat}}{p_{in}} \quad (3.2)$$

Since the ratio of nitrogen and oxygen in dry air is known to be 79 : 21, the inlet oxygen fraction can be found via:

$$x_{O_2,in} = \frac{1 - x_{H_2O,in}}{1 + \frac{79}{21}} \quad (3.3)$$

and the molar nitrogen fraction can be determined out of:

$$x_{N_2,in} + x_{H_2O,in} + x_{O_2,in} = 1 \quad (3.4)$$

The resulting inlet gas composition for different pressures is shown in Figure 3.1.

In order to find a correlation between the reference exchange current density i_0 for the oxygen reduction reaction (ORR) at the cathode side and the temperature, experimental results obtained by Parthasarathy *et al.* [32] were used. The following relation has been obtained using a curve-fitting approach:

$$i_{0,\varphi=5.2}(T) = 1.08 \times 10^{-21} \times \exp(0.086 * T) \quad (3.5)$$

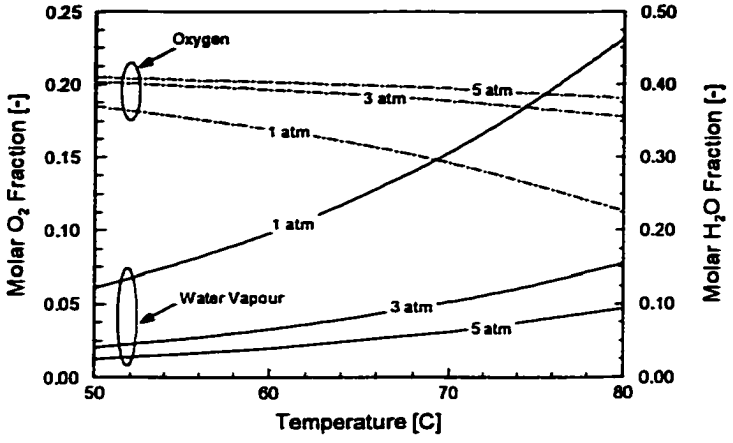

Figure 3.1: Molar inlet fraction of oxygen and water vapour as a function of temperature at three different pressures.

where T is the temperature in [K] and φ is the so-called *roughness factor*[1]. The second column of Table 3.1 lists the exchange current densities obtained by applying the above equation.

For the base case in our computational model we assume an exchange current density of $i_0 = 4.4 * 10^{-7}\,\mathrm{A/cm^2}$ at a cell temperature of 353 K [42]. Comparing this with the value obtained by Parthasarathy *et al.*, the roughness factor in our model can be determined as:

[1]The roughness factor φ is defined as the ratio between the electrochemically active area and the geometrical area of the cell, and it provides a measure the quality of the catalyst distribution. The exchange current density of the oxygen reduction reaction is only of the order of $10^{-9} - 10^{-10}$ $\mathrm{A/cm^2}$ [2]. In order to keep the activation losses within a reasonable range, however, the exchange current density based on the geometrical area must be at least in the range of $10^{-6} - 10^{-7}\,\mathrm{A/cm^2}$. This means that the electrochemically active area has to be at least two orders of magnitude higher then the geometrical area of the fuel cell.

$$\varphi^* = 5.2 \times \frac{4.4 * 10^{-7}}{1.65 * 10^{-8}} = 138.4 \tag{3.6}$$

Using this correction factor, all the exchange current densities that have been found by Parthasarathy *et al.* were adjusted to the higher catalyst loading by linear interpolation and thus the third column in Table 3.1 was obtained. It should be emphasized that for the current study it is important to obtain a qualitative estimation of how the various parameters depend on the temperature. The experiments conducted by Parthasarathy *et al.* and the experiments that we use for our base case taken from Ticianelli *et al.* [42] were conducted under different (unknown) conditions. The exchange current densities listed in the third column in Table 3.1 appear reasonable and were therefore used for the current parametric study.

Table 3.1: Exchange current density of the ORR as a function of temperature

T	$i_{0,\vartheta=5.2}(T)$	$i^*_{0,\vartheta=138.4}(T)$
353	1.65×10^{-8}	4.4×10^{-7}
343	6.99×10^{-9}	1.86×10^{-7}
333	2.96×10^{-9}	7.86×10^{-8}
323	1.25×10^{-9}	3.33×10^{-8}

Next, an expression had to be found for the protonic conductivity of the electrolyte membrane as a function of temperature. A theoretical value was given by Bernardi and Verbrugge [7] as:

$$\kappa = \frac{F^2}{RT} z_f D_{H^+} c_f \tag{3.7}$$

where F is Faraday's constant, R is the universal gas constant, z_f and c_f are the fixed charge number and -concentration, respectively, T is the temperature in [K] and $\mathcal{D}_{H^+}$ is the diffusivity if the hydrogen proton inside the membrane,which depends strongly on the temperature. The diffusivity of the hydrogen proton was measured to be [7] $\mathcal{D}_{H^+} = 4.5 * 10^{-5}$ cm^2 / s at 80 °C and $\mathcal{D}_{H^+} = 5.6 * 10^{-5}$ cm^2 / s at 95 °C. The second column in Table 3.2 lists the values for the diffusivity obtained by linear extrapolation from these values, and the third column shows the theoretical membrane conductivities assuming a linear dependence of the protonic diffusivity on the temperature.

These values, however, show a large deviation from experimentally measured protonic conductivities in an operating fuel cell. For example, Springer *et al.* [38] obtained a value of $\kappa = 0.068$ S / cm. Coincidentally, this value was also used by Bernardi and Verbrugge [8] to match their modelling data with experimental results from Ticianelli *et al.* [42]. Thus, this value was taken for our base case, and linearly scaled as a function of temperature, based on the theoretical value from the third column. The last column in Table 3.2 lists the adjusted values that were taken for the membrane conductivity at different temperatures.

Table 3.2: Proton diffusivity and membrane conductivity as function of temperature.

T [K]	D_{H^+} [cm^2 / s]	κ_{theo} [S / cm]	κ [S / cm]
353	4.5×10^{-5}	0.17	0.068
343	3.8×10^{-5}	0.13	0.052
333	3.0×10^{-5}	0.11	0.044
323	2.3×10^{-5}	0.095	0.038

As before, the adjustment of the reference exchange potential E^0 with the cell temperature is described by the Nernst equation:

$$E^0 = 1.23 - 0.9 \times 10^{-3}(T - 298) + 2.3\frac{RT}{4F}\log\left(p_{H_2}^2 p_{O_2}\right) \tag{3.8}$$

Using these adjustments, the polarization curves obtained for various cell temperatures are shown in Figure 3.2. The change in the initial drop due to the lower exchange current density is relatively small compared to the drop-off in the linear region, caused by the ohmic losses. The maximum achievable current density increases slightly with increasing operating temperature due to the overall enhanced mass transport, *i.e.* by diffusion of the reactants. For the power density curves it has to be noted that the maximum power density is shifted towards a higher current density with an increase in temperature, which is caused by the reduction in ohmic losses.

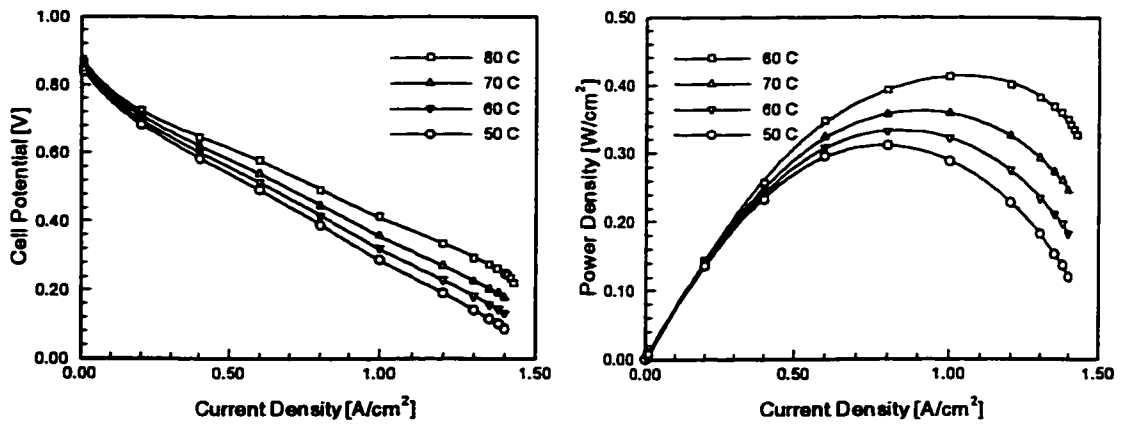

Figure 3.2: Polarization Curves (left) and power density curves (right) at various temperatures obtained with the model. All other conditions are at base case.

For comparison, experimental results reproduced from Ticianelli *et al.* [42] are shown in Figure 3.3. The polarization curves shown have been reproduced by using the electrokinetic data given in Table 2.8 on page 57. Qualitatively, the effect of the operating temperature on the performance of both cells agrees well with the modelling results presented above. Note that the difference in performance between these two cells is caused solely by the amount of Nafion impregnation at the catalyst layer. PEM 45 used 4% instead of 3.3%, which lead to a "starvation" of reactants at the cathode side.

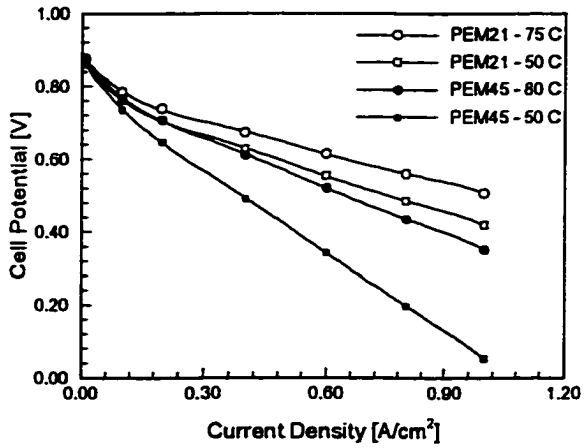

Figure 3.3: Experimentally obtained polarization curves for different operating temperatures.

Overall the modelling results exhibit good qualitative agreement with experimental data. However, in order to obtain this agreement, it is essential to understand the impact that the temperature has on the various parameters of the model, which had to be found experimentally.

3.3 Effect of Pressure

Similar to the temperature, the operating pressure enhances numerous transport properties in a PEM Fuel Cell. The following adjustment have to be made to account for a change in the operating pressure:

- the *inlet gas compositions.* A change in the operating pressure leads to a change in the inlet gas compositions, assuming the inlet gases are fully humidified.
- the *exchange current density* i_0. The dependence of the cathodic exchange current density on the oxygen pressure was investigated experimentally by Parthasarathy *et al.* [31].
- the *reference potential* E_{ref}. According to the Nernst equation, an increased pressure leads to an increase in the equilibrium potential.
- the *gas-pair diffusivities* $\mathfrak{D}_{ij}$ in the Stefan-Maxwell equations. It is well known that the product of pressure and the binary diffusivity is constant [13]. Hence, a doubling of the pressure will cut the binary diffusivity in half.

Since the saturation pressure for water is only a function of temperature, it remains constant for a variation of the inlet pressure, and the molar fraction of water vapour in the incoming cathode gas stream is given by equations 3.1 and 3.2. The molar oxygen and nitrogen fractions result then out of equations 3.3 and 3.4. Figure 3.4 shows the resulting inlet gas composition at the cathode side as a function of the pressure. It can be seen that the change in the inlet gas composition is particularly strong in the range from 1 atm to 3 atm. Above 3 atm, the composition changes only slightly with the pressure.

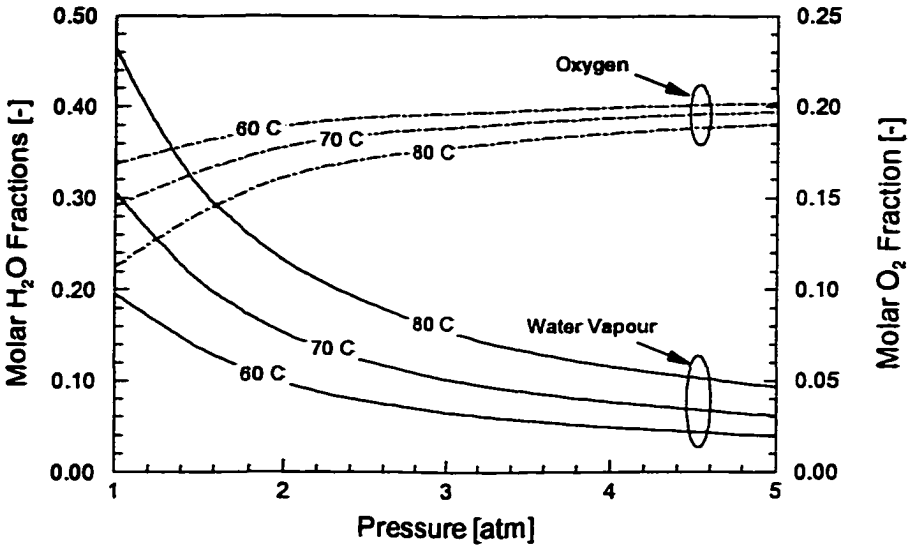

Figure 3.4: Molar oxygen and water vapour fraction of the incoming air as a function of pressure for three different temperatures.

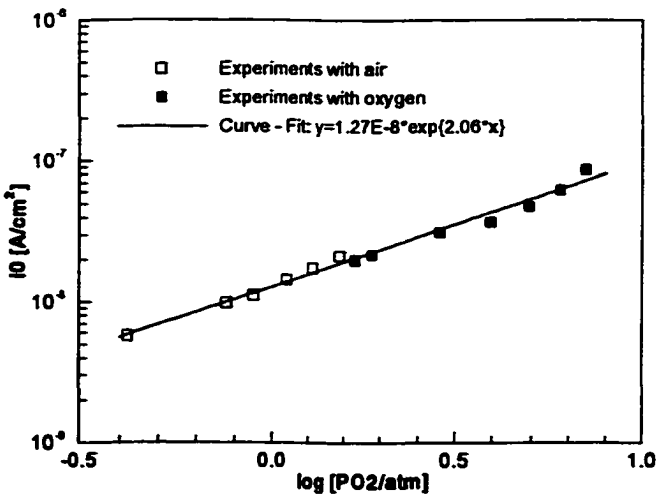

Figure 3.5: The dependence of the exchange current density of the oxygen reduction reaction on the oxygen pressure.

The exchange current density was scaled to qualitatively match experimental results obtained by Parthasarathy *et al.* [31], who determined the cathode side exchange current density as a function of the partial oxygen pressure at a temperature of 50 °C. The results are summarized in Figure 3.5. A linear relationship was found between the logarithm of the exchange current density i_0 and the logarithm of the oxygen partial pressure, according to:

$$i_0 = 1.27 \times 10^{-8} \times \exp^{2.06 * P_{O2}} \tag{3.9}$$

This equation was applied to the partial oxygen pressure of the incoming air, as listed in the second column of Table 3.3, to yield an approximation for the cathodic exchange current at a temperature of 50 °C, given in the third column of Table 3.3. The last column was obtained by linearly interpolating the exchange current densities in the third column so that the value for our base case, where the cathode side pressure is 5 atm and the temperature is 80 °C, is matched, according to:

$$i_0\,(80\,^\circ\mathrm{C}, \varphi = 138.4) = i_0\,(50\,^\circ\mathrm{C}) \times \frac{4.4 \times 10^{-7}}{9.27 \times 10^{-8}} \tag{3.10}$$

The values in the last column are the exchange current densities that were taken to model the fuel cell under different pressures.

Again this method might appear somewhat arbitrary, but it has to be kept in mind that for this part of the analysis it is important to understand the qualitative impact that the operating pressure has on the different parameters and then find a quantitative expression that represents this as closely as possible.

Table 3.3: Exchange current density of the ORR as a function of pressure

p_c[atm]	p_{O_2}[atm]	$i_0\,(p_c, T = 50\,°C)$	$i_0\,(p_c, T = 80\,°C)$
1.0	0.1251	1.64×10^{-8}	0.78×10^{-7}
1.5	0.1483	1.72×10^{-8}	0.82×10^{-7}
3.0	0.5451	3.90×10^{-8}	1.85×10^{-7}
5.0	0.9650	9.27×10^{-8}	4.40×10^{-7}

The adjustment of the reference potential E^0 was done according to the corrected Nernst equation (equation 2.39), and the diffusion coefficients for the Stefan-Maxwell equations were adjusted automatically in our model.

The result of the computations with varying operation pressure is shown in Figure 3.6. The higher oxygen fraction at the cathode side inlet leads eventually to a higher maximum current density, as can be seen in the left part of Figure 3.6. This increase is significant when the pressure is increased from atmospheric pressure up to 3 atm, which corresponds well with Figure 3.4. A further increase in the pressure from 3.0 atm to 5.0 atm does not lead to a significant improvement in terms of the limiting current density. It should be emphasized again that this is only valid as long as the incoming gases are fully humidified. The reason why even at extremely low current densities the average molar oxygen fraction at the catalyst layer differs from the value of the incoming air is discussed in Chapter 3.4.

The polarization curves on the right hand side of Figure 3.6 reveal a significant change in the initial drop-off, when the pressure is changed. This can be attributed to the change in the equilibrium potential that goes along with a decrease in the reactant pressure (Nernst equation). To a much lesser extend, the decrease in the

exchange current density with decreasing pressure also contributes to this effect.

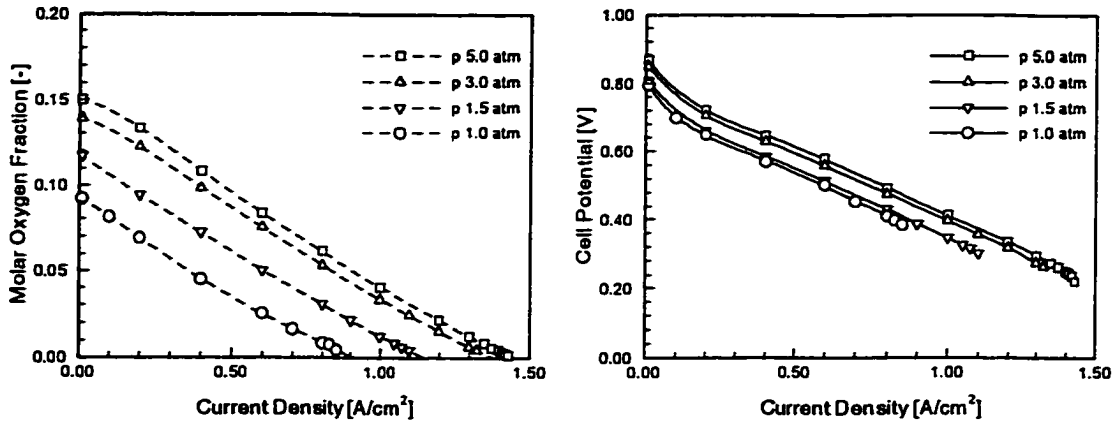

Figure 3.6: The molar oxygen fraction at the catalyst layer vs. current density (left) and the polarization curves (right) for a fuel cell operating at different cathode side pressures. All other conditions are at base case.

Again, a detailed comparison with experimental results from the literature can only be made on a qualitative basis, since the exact conditions of the various experiments are not reported. In Figure 3.7, experimentally obtained polarization curves by Kim *et al.* [20] are reproduced. The experiments were conducted with pure hydrogen at the anode side and air at the cathode side. Although the exact details of the experiments, such as the stoichiometric flow ratio and the cell geometry, are not known, the two main effects that the cathode side pressure has on the fuel cell performance can be observed for both temperatures: the increase of the limiting current density with an increase in pressure and an overall better cell performance, which can be attributed to an increase in the equilibrium potential. It is interesting to note that at 50 °C the limiting current densities for 3.0 atm and 5.0 atm almost coincide,

which agrees well with the modelling results shown above. On the other hand, the polarization curves for 3.0 atm and 5.0 atm at the elevated temperature were very close, which is also in good agreement with the modelling results at a temperature of 80 °C.

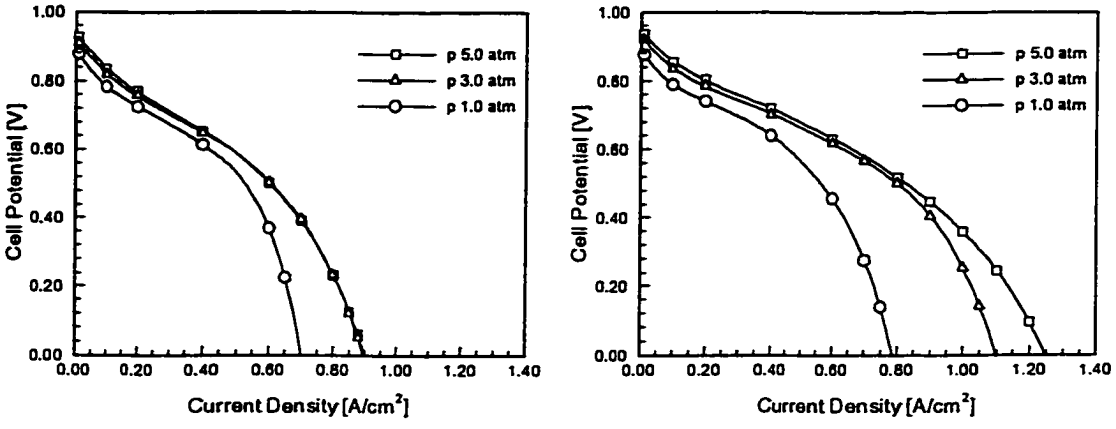

Figure 3.7: Experimentally obtained polarization curves at two diffferent temperatures (left: 50 °C; right: 70 °C) for various cathode side pressures.

In general, it is difficult to compare the results obtained with the current model with experimental results taken from the literature, since various parameters that are not given in the literature influence the fuel cell performance. Qualitative agreement, however, is very good and the principal physical benefits of operating a fuel cell at an elevated pressure have been confirmed.

3.4 Effect of Stoichiometric Flow Ratio

According to equation 2.42, an increase in the stoichiometric flow ratio means simply that the velocity of the incoming gas has to be increased with all remaining parameters remaining constant. The result is an increase in the molar oxygen fraction at the catalyst layer, as can be observed in Figure 3.8. Note that even at a current density of almost zero, the molar oxygen fraction does not reach its inlet value of around 19%. The reason for this is the constant stoichiometric flow ratio even at low current densities, which means that the air leaving the cell will always be depleted of oxygen by a significant amount, and the plot in Figure 3.8 shows the average molar oxygen fraction from the inlet to the outlet and under the land area.

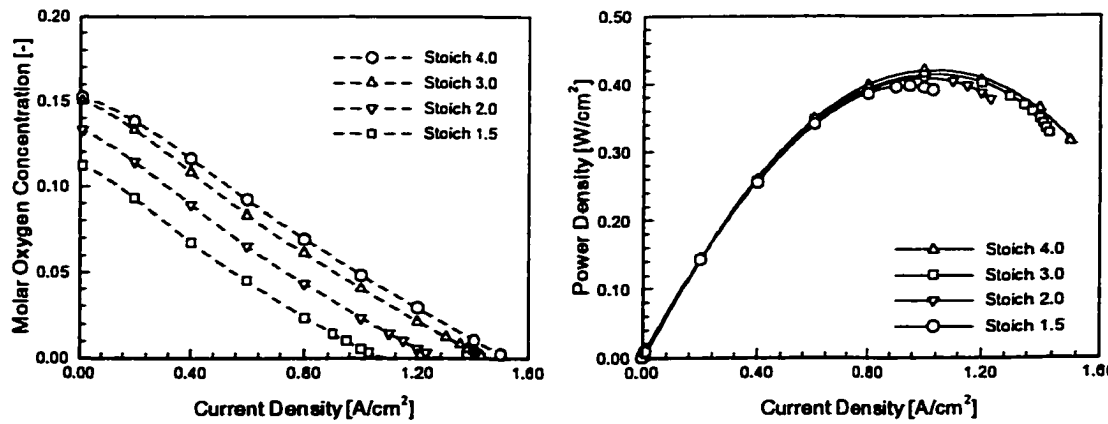

Figure 3.8: Molar oxygen fraction at the catalyst layer as a function of current density (left) and power density curves (right) for different stoichiometric flow ratios.

The increments of the gain in the limiting current density become smaller as the stoichiometric flow ratio increases, *i.e.* the gain in the maximum cell current when

the stoichiometric flow ratio is increased from $\zeta = 1.5$ to $\zeta = 2.0$ is about as large as the gain for an increase from $\zeta = 2.0$ to $\zeta = 3.0$. The benefits for a further increase to $\zeta = 4.0$ is considerably smaller.

Since there is a price to pay for an increase in the stoichiometric flow ratio, there must be an optimum, where the gain in the cell performance just balances the additional costs of a more powerful blower. This will have to be carefully considered, when designing the fuel cell system.

The right hand side of Figure 3.8 shows that the potential gain in power density is relatively small. This, however, is only valid as long as the cell is not "starved" of oxygen at a current density that is below the point that corresponds to the maximum power density, which in turn depends on the exact cell geometry and the properties of the materials that are used.

The effect of the stoichiometric flow ratio on the local current distribution is shown in Figure 3.9. An increase in the stoichiometric flow ratio from 2.0 to 4.0 leads to a decrease in the maximum local current density from above $2.2\,\mathrm{A/cm^2}$ to below $1.9\,\mathrm{A/cm^2}$ at the inlet area. This is further reduced to below $1.8\ \mathrm{A/cm^2}$, if the stoichiometric flow ratio is increased to $\zeta = 4.0$. Overall, a stoichiometric flow ratio of $\zeta = 3.0$ appears to be optimum in terms of cell performance.

It is important to realize that the effect of the stoichiometric flow ratio on the water management can not be assessed with the current model. The amount of incoming air determines, how much water vapour can be carried out of the cell. This question can only be addressed with a two-phase model.

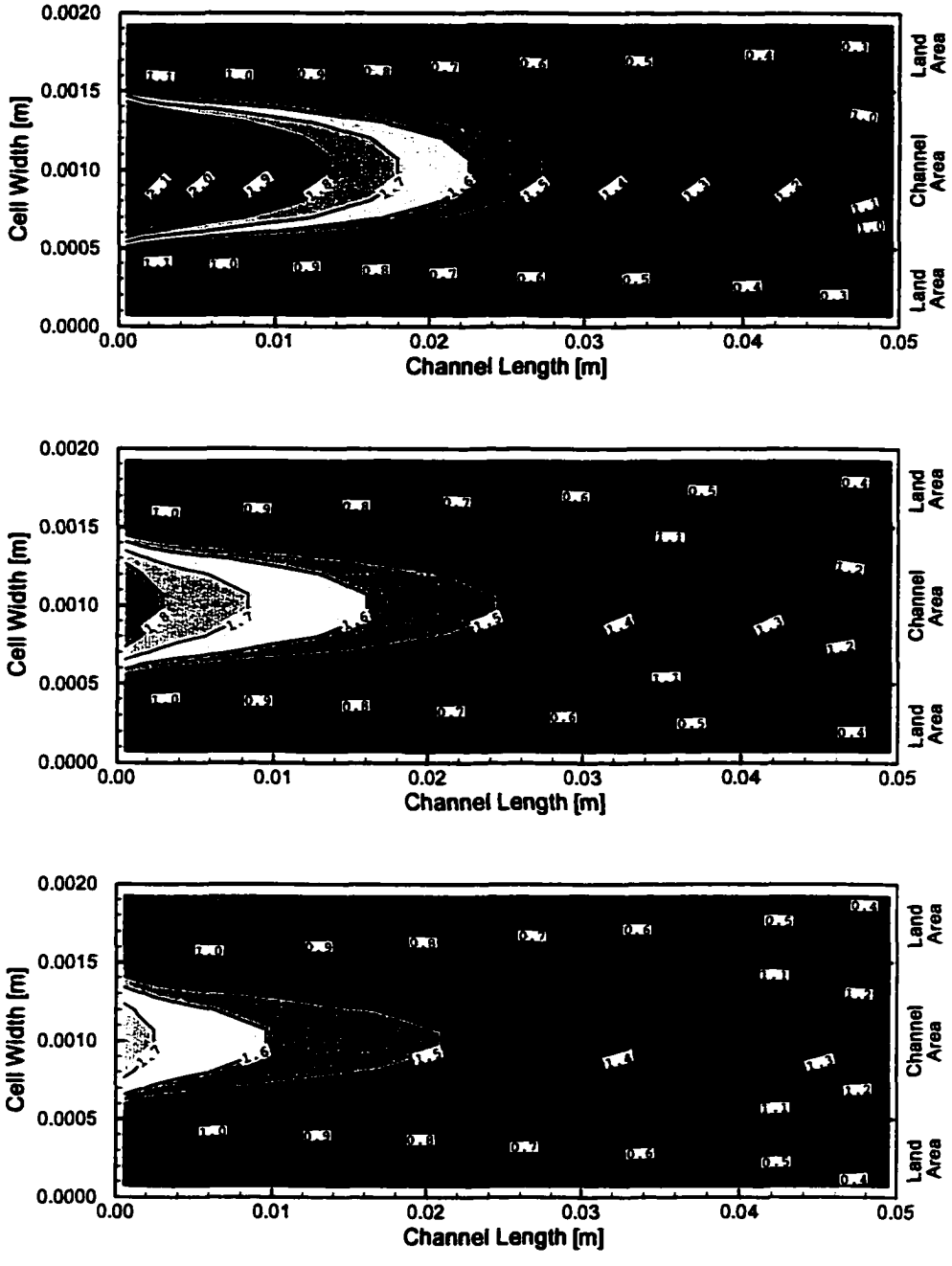

Figure 3.9: Local current density distribution for three different stoichiometric flow ratios: $\zeta = 2.0$ (top), $\zeta = 3.0$ (middle) and $\zeta = 4.0$ (bottom). The average current density is $1.0\,\mathrm{A}/\mathrm{cm}^2$.

3.5 Effect of Oxygen Enrichment

In order to alleviate mass transport losses at the cathode side, the incoming air stream is sometimes enriched with oxygen. The effect of using pure oxygen instead of air has been experimentally determined by Kim *et al.* [20]. Figure 3.10 shows the polarization curves of a fuel cell operating at two different pressures at a temperature of 50 °C for both air and pure oxygen. The obtainable current densities are more than 80% higher for all different cathode side pressures. The differences in the initial drop-off at low current densities are now understood in light of the dependence of the equilibrium potential on the oxygen pressure.

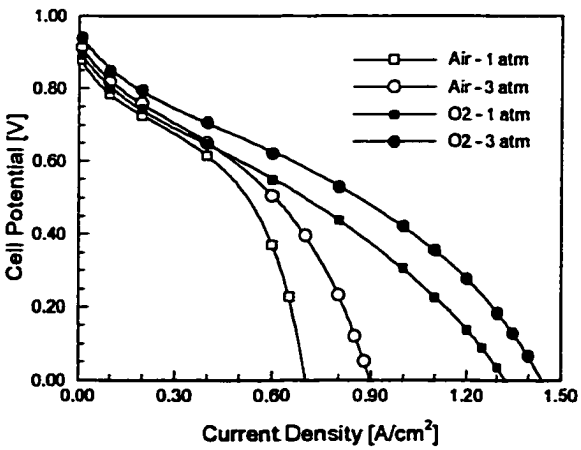

Figure 3.10: Experimentally measured fuel cell performance at 50 °C for air and pure oxygen as the cathode gas.

Using our three-dimensional model we compared the performance of the base case with oxygen enriched air, where the molar oxygen fraction of the incoming cathode gas stream has been increased to 25% and 30%, respectively. The resulting cell performance is shown in Figure 3.11. The left hand side shows again the molar

oxygen concentration at the cathodic catalyst layer as a function of the nominal current density. The higher inlet fraction of oxygen is carried over to the catalyst layer, *i.e.* the lines remain equidistant to one another. This ultimately leads to a tremendous increase in the limiting current density. It will be shown later that the slope of the molar oxygen fraction vs. current density lines depends on the geometry of the fuel cell, *i.e.* the thickness and porosity of the carbon fiber paper and the ratio of the channel width to the land area.

The right-hand side in Figure 3.11 shows the polarization curves for the three different cases. All curves are quite similar until the mass transport limitations start affecting the performance. For the case with an oxygen inlet fraction of 30%, no mass transport losses occur and the polarization curve follows a straight line. In this case the ohmic losses, which occur predominantly in the membrane become the limiting factor for achieving even higher current densities.

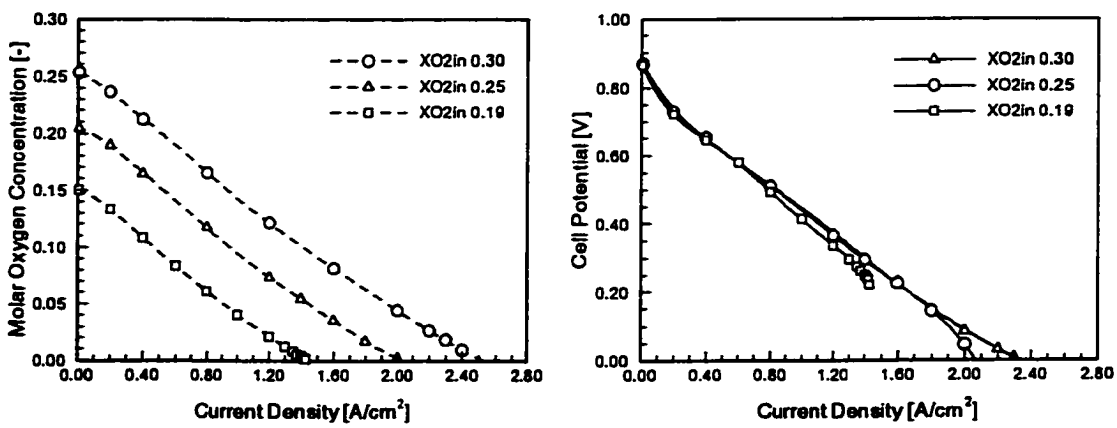

Figure 3.11: Molar oxygen fraction at the catalyst layer as a function of current density (left) and polarization curves (right) for different oxygen inlet concentrations.

3.6 Effect of GDL Porosity

The porosity of the gas-diffusion layer affects the performance of the fuel cell in two aspects: a higher void fraction provides less resistance for the reactant gases to reach the catalyst layer on one hand, but in turn it leads to a higher *contact resistance*, as will be described below.

An increase in the porosity ε enhances the diffusion of the species towards the catalyst layer, as can be seen from the *Bruggemann correction* [33]:

$$D_{ij}^{eff} = D_{ij}\varepsilon^{1.5} \tag{3.11}$$

In addition, the gas-phase permeability is affected in a way described in Appendix C. However, the convection described by Darcy's law plays only a minor role for the flux of the species towards the catalyst layer; the main contribution was found to be diffusion, particularly at the low hydraulic permeability chosen for the base case.

Figure 3.12 shows the molar oxygen fraction at the catalyst layer for different values of the porosity. Here we observe that the gradient of the oxygen concentration versus the current density changes with the porosity of the GDL. Starting from approximately the same value at a very low current density ($0.01\,\mathrm{A/cm^2}$), the oxygen concentration decreases rapidly with increasing current density at low values for the porosity, resulting in a limiting current density of only $0.75\,\mathrm{A/cm^2}$. On the other hand, when the porosity is increased from $\varepsilon = 0.4$ to $\varepsilon = 0.5$, the limiting current density increases from around $1.4\,\mathrm{A/cm^2}$ to around $2.4\,\mathrm{A/cm^2}$, which constitutes an increase of around 70%.

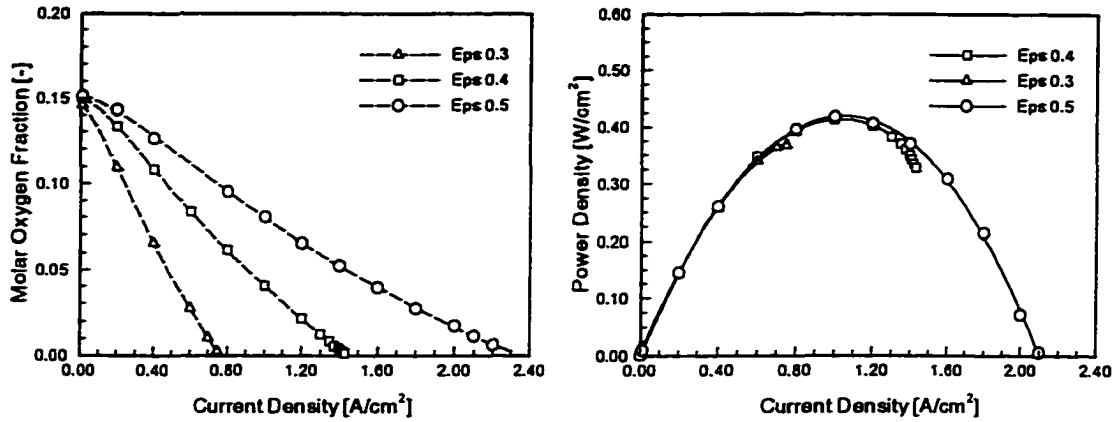

Figure 3.12: Average molar oxygen concentration at the catalyst layer (left) and power density curves (right) for three different GDL porosities.

The right hand side of Figure 3.12, however, shows that the power density decreases rapidly after the maximum power has been reached. All three power density curves are very close, because the negative impact of an increased porosity on the ohmic loss is small and is partly offset by the beneficial effect that results out of a reduction in the mass transport loss. At a porosity of 0.3, however, the cathode side is starved of oxygen before the maximum power density has been reached. Hence, it is important to keep the porosity at a maximum level in order to avoid starvation. This demonstrates the importance of avoiding the accumulation of liquid water inside the GDL, since this will reduce the pore-size available for the gas-phase and thus enhance mass transport losses.

As mentioned above, another loss mechanism that is important when considering different GDL porosities is the *contact resistance*. Contact resistances occur at all interfaces of different materials and components, and in many cases their contribution

to the fuel cell performance is small. The most important contact resistance occurs at the interface of the bipolar plates and the outer surfaces of the membrane-electrode assembly, the carbon fiber paper. The magnitude of this resistance depends on various parameters, including the material used, the surface preparation and the mechanical pressure imposed on the stack.

In the base case, a contact resistance of $0.006\,\Omega\,\mathrm{cm}^2$ was assumed. However, this value depends on so many parameters that it is worthwhile exploring, how the fuel cell performance is affected by a change in the contact resistance, *i.e.* by a change in the stack pressure. Since it can be assumed that the contact resistance varies linearly with the area of the surfaces that are in contact, the contact resistance is a linear function of the porosity ε.

Figure 3.13 shows the power density curves for a contact resistance of $0.03\,\Omega\,\mathrm{cm}^2$ and $0.06\,\Omega\,\mathrm{cm}^2$, respectively. Already for a value of $0.03\,\Omega\,\mathrm{cm}^2$ the maximum power density for a porosity of $\varepsilon = 0.4$ is higher than for $\varepsilon = 0.5$. This effect is even stronger, when a contact resistance of $0.06\,\Omega\,\mathrm{cm}^2$ is assumed. Note also the decrease in the maximum current density at a porosity of $\varepsilon = 0.5$ due to the increase in ohmic losses, which means that in this case the limiting current density is determined by the membrane loss instead of the onset of mass transport limitations.

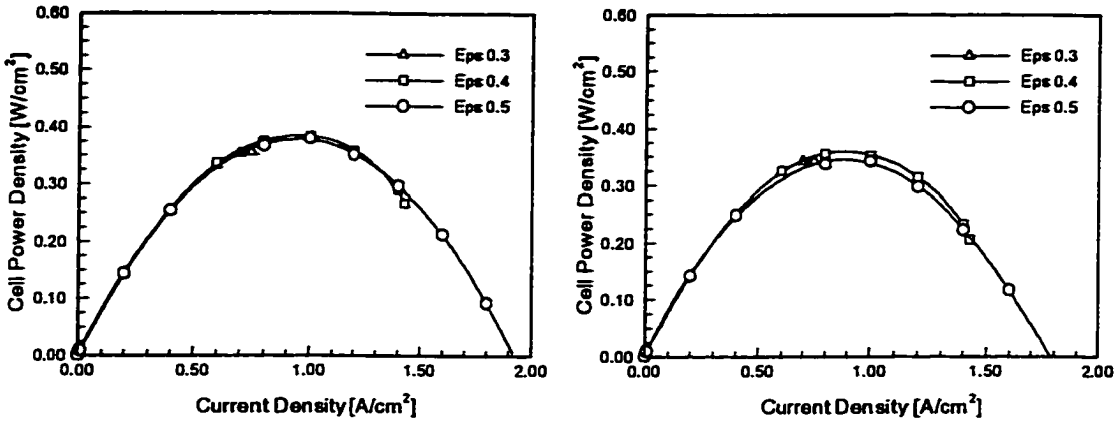

Figure 3.13: Power density curves for three different GDL porosities at two values for the contact resistance: $R_c = 0.03\,\Omega\,\mathrm{cm}^2$ (left) and $R_c = 0.06\,\Omega\,\mathrm{cm}^2$ (right).

Another the beneficial effect of a high GDL porosity is to even out the local current densities, as can be seen in Figure 3.14. Whereas the maximum local current density exceeds $1.8\,\mathrm{A}/\mathrm{cm}^2$ near the inlet area for a porosity of $\varepsilon = 0.4$, this value is reduced to about $1.5\,\mathrm{A}/\mathrm{cm}^2$ for a porosity of $\varepsilon = 0.5$ and $1.4\,\mathrm{A}/\mathrm{cm}^2$ for $\varepsilon = 0.6$; the local current density becomes much more evenly distributed with an increase in porosity.

Overall, the porosity of the GDL has been found to be a very sensitive parameter for the fuel cell performance, as it has a large influence on the limiting current density, and, since the contact losses depend on it in a linear manner, it also affects the fuel cell performance in form of the maximum power density.

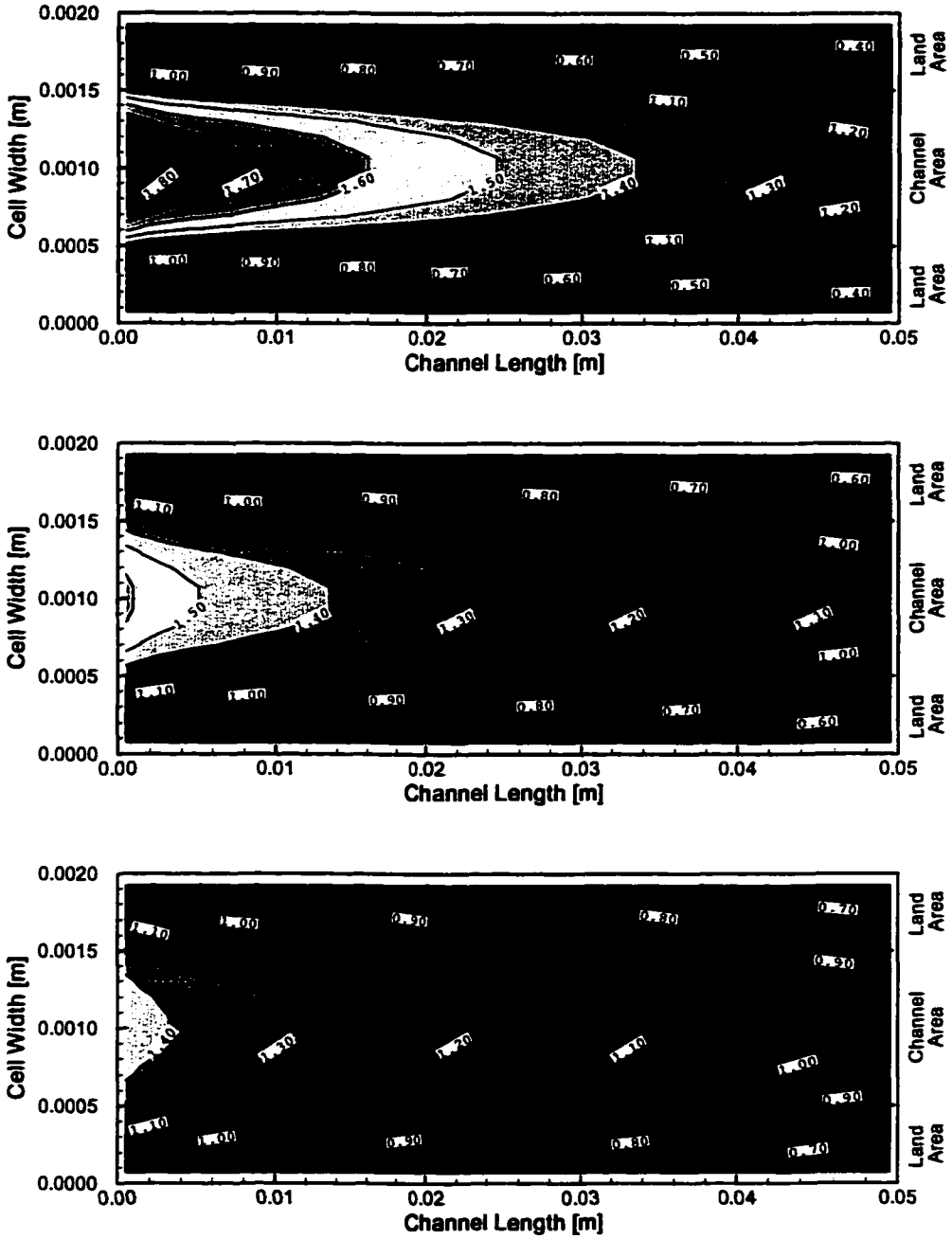

Figure 3.14: Local current densities for three different GDL porosities: $\varepsilon = 0.4$ (top), $\varepsilon = 0.5$ (middle) and $\varepsilon = 0.6$ (bottom). The average current density is $1.0\,\mathrm{A}/\mathrm{cm}^2$ for all cases.

3.7 Effect of GDL Thickness

Next, the effect of the GDL thickness shall be investigated. In theory, a thinner GDL reduces the mass transport resistance as well as ohmic losses, which are relatively small because of the high conductivity of the carbon fiber paper.

Figure 3.15 shows the average molar oxygen fraction at the catalyst layer as a function of the current density. For current densities below $0.3\,\mathrm{A/cm^2}$ the molar oxygen fraction decreases with an decreasing GDL thickness. We will see below that the reason for this behaviour is that a thinner GDL prevents the oxygen from diffusing in the z-direction from the channel area towards the land area. At a high current density the reduced resistance to the oxygen diffusion by the thinner layer becomes important, and the molar fraction at the catalyst layer increases with a decreasing GDL thickness, thus increasing the limiting current density.

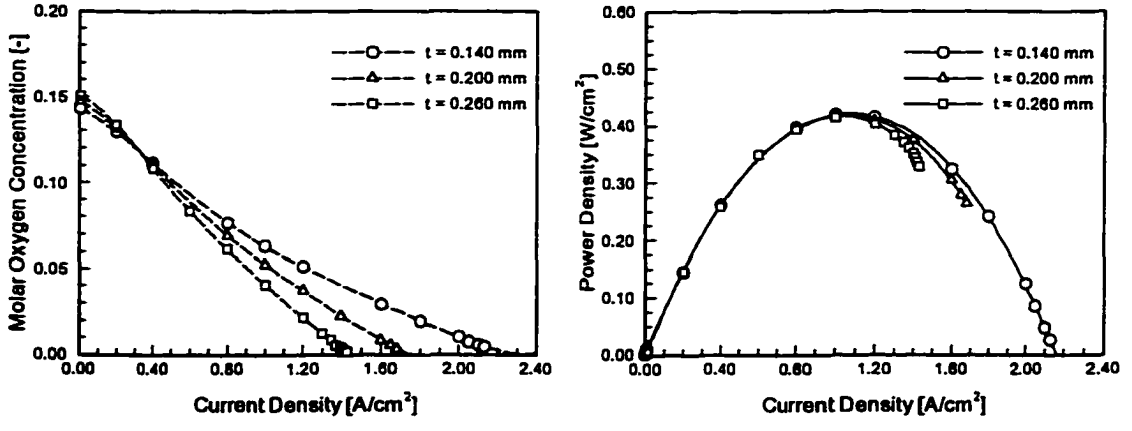

Figure 3.15: Molar oxygen concentration at the catalyst layer as a function of the current density and the power density curves for three different GDL thicknesses.

The effect of the GDL thickness on the polarization curve and the power density curve is small, because the only parameters affected are the mass transport losses – which is quantitatively a weak effect – and the ohmic losses inside the GDL, which are almost negligible. Therefore, the power density curves show differences only at high current densities. Overall, the predominant effect of the GDL thickness is on the limiting current density. There also might be issues concerning the water management, but as before, these can not be addressed with the current version of this model.

The fact that at low current densities the oxygen concentration is lower at the catalyst layer for a thinner GDL than for the thicker GDL is an interesting aspect of this diffusion problem and shall be briefly discussed here. Figures 3.16 and 3.17 show in detail the molar oxygen concentration at the catalyst layer for the three different GDL at a low and a high current density, respectively. At a current density of $0.2\,\mathrm{A}/\mathrm{cm}^2$ the oxygen consumption is low. For the thicker GDL, the "space" for the oxygen to diffuse in the lateral (z-) direction is larger than for a thinner GDL. As a result, the oxygen concentration under the land area is higher for the thicker GDL. And although the concentration under the channel areas is higher for the thinner GDL, the average concentration remains lower for this case.

At a current density of $1.2\,\mathrm{A}/\mathrm{cm}^2$ the diffusion in the y-direction is clearly the limiting factor and constitutes the limitation that eventually determines the maximum current density of the fuel cell. For the thicker GDL, the average molar oxygen fraction is around 2.1%, which has already been observed in Figure 3.15, whereas the thinner GDL allows for a higher oxygen fraction and ultimately a higher limiting current density.

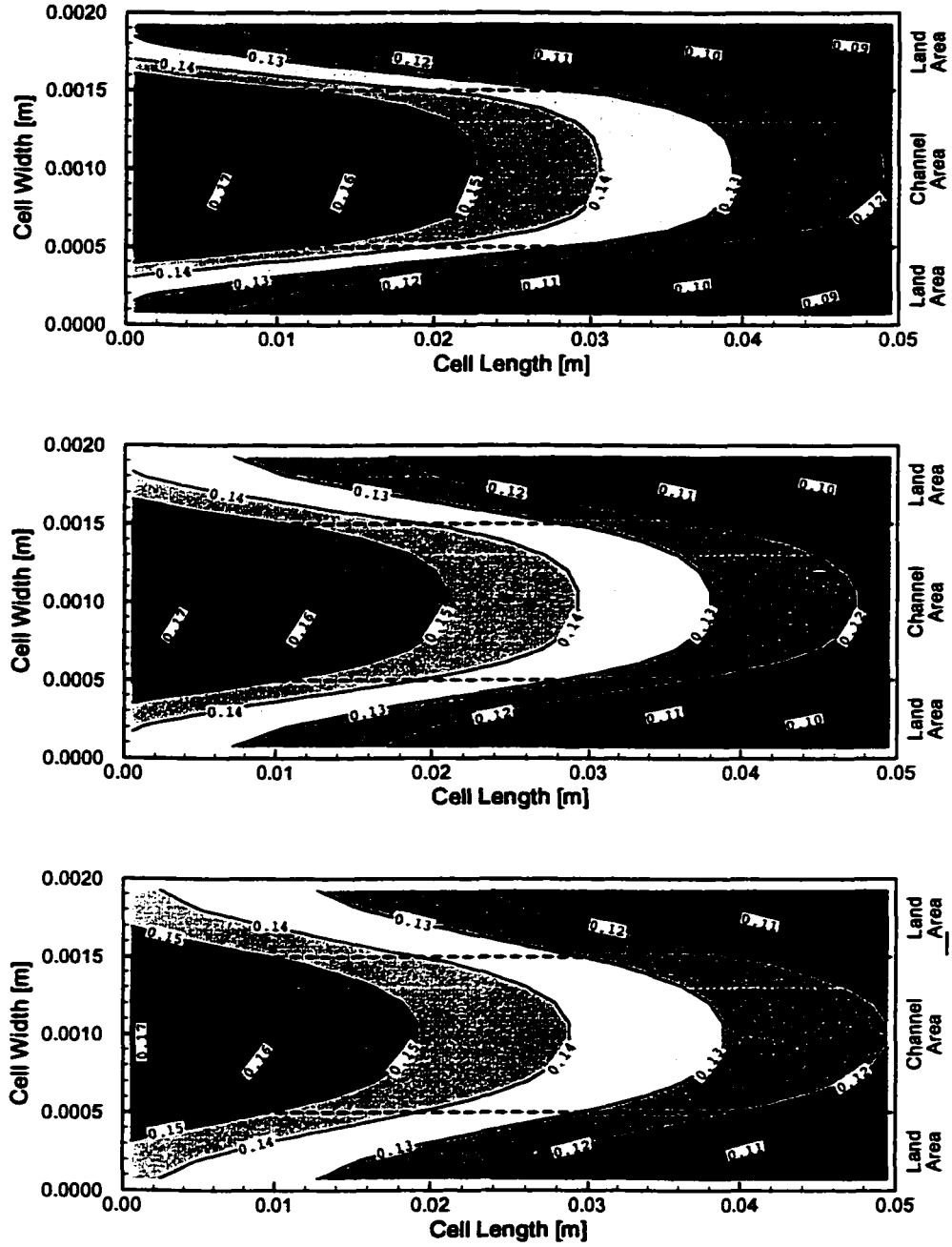

Figure 3.16: Molar oxygen concentration at the catalyst layer for three different GDL thicknesses: 140 μm (upper), 200 μm (middle) and 260 μm (lower). The nominal current density is 0.2 A / cm^2.

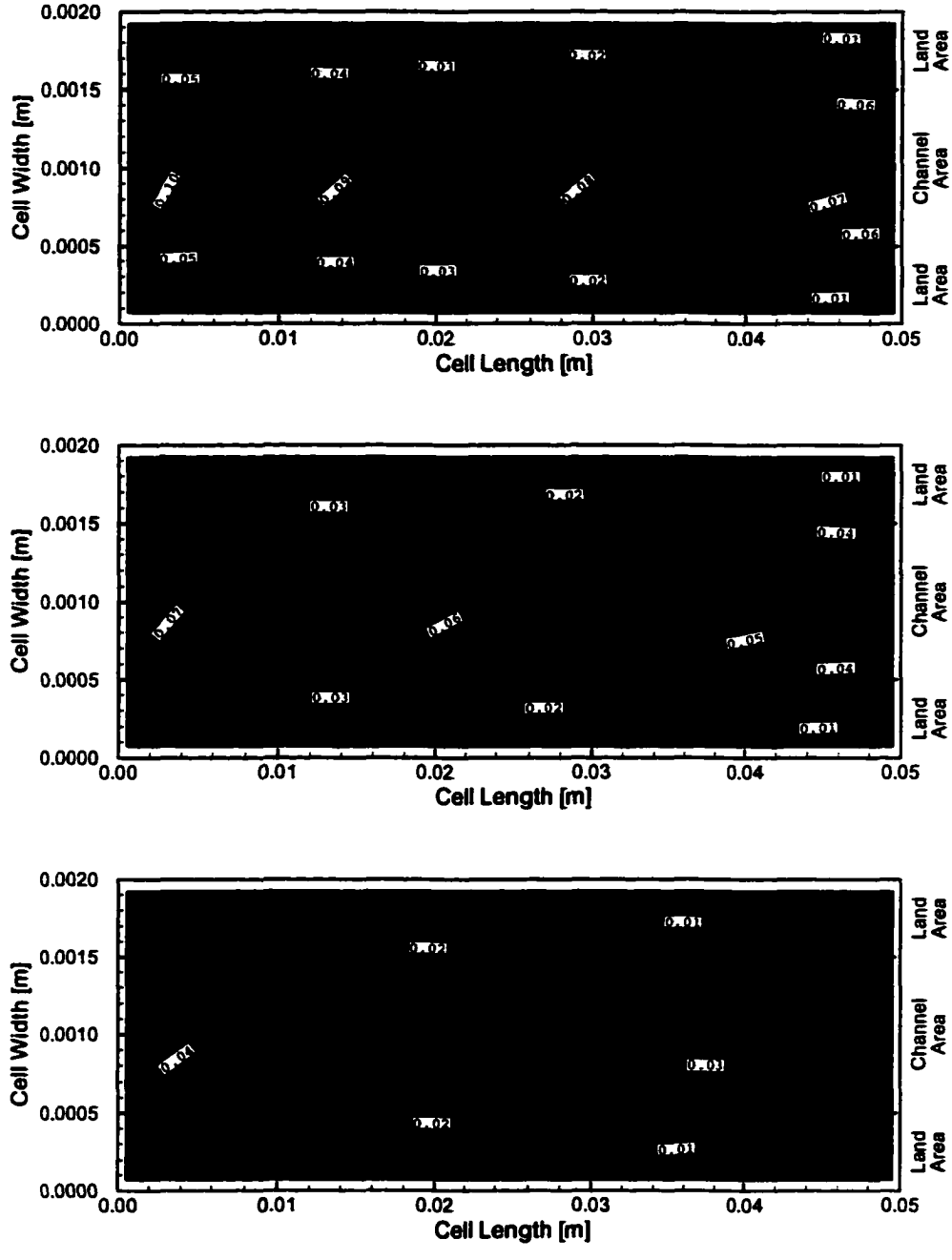

Figure 3.17: Molar oxygen concentration at the catalyst layer for three different GDL thicknesses: 140 μm (upper), 200 μm (middle) and 260 μm (lower). The nominal current density is 1.2 A / cm^2.

3.8 Effect of Channel-Width-to-Land-Area Ratio

Two different effects determine the ideal ratio between the width of the gas flow channel and the land area between the channels. A reduction in the land area width enhances the mass transport of the reactants to the catalyst layer that lies under the land area. It is expected that this will affect mainly the limiting current density and to a lesser degree the voltage drop due to mass transport limitations. On the other hand, a reduced width of the land area increases the contact resistance between the bipolar plates and the membrane-electrode assembly. Since this is an ohmic loss, it is expected to be directly correlated to the land area width.

Again, the molar oxygen fraction and the power density curves for three different ratios between the land area and the channel width is shown in Figure 3.18.

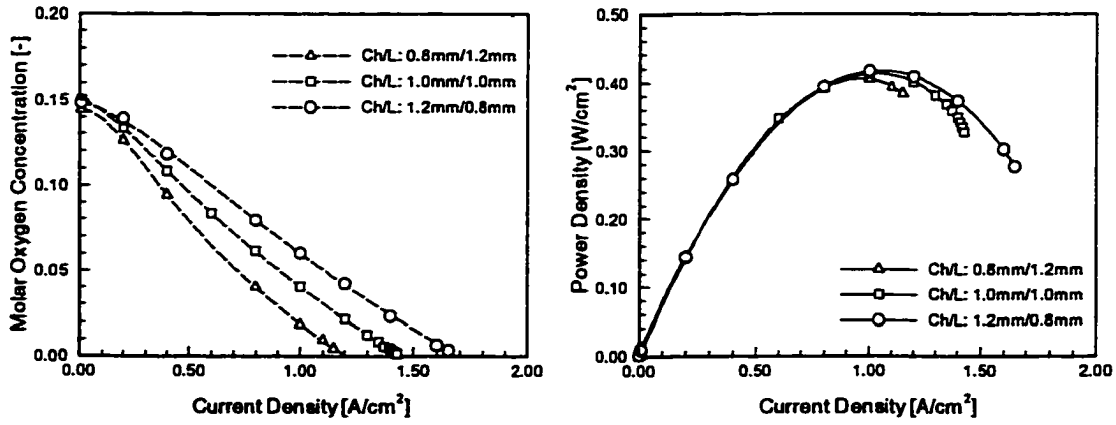

Figure 3.18: Average molar oxygen fraction at the catalyst layer as a function of current density (left) and power density curves (right) for three different channel and land area widths.

Similar to other parameters, the width of the gas flow channel mainly affects the limiting current density; a reduction in the channel width to 0.8 mm results in a decrease in the limiting current density from 1.42 A / cm^2 to 1.2 A / cm^2 (15.5%), whereas an increase in the channel width from 1.0 mm to 1.2 mm along with a decrease in the land area results in a limiting current density of 1.65 A / cm^2 (16.1%), *i.e.* equal steps for an increase in the channel width result in equal increases in the limiting current density.

The power density is weakly affected, as can be seen on the left-hand side of Figure 3.18. For the case of the narrow channel, mass transport limitations start to become noticeable at 1.0 A / cm^2, and the maximum of the power density occurs at this current density. For an increased channel width from 1.0 mm to 1.2 mm, the maximum in the powered density stays roughly the same at around 1.1 A / cm^2, because the mass transport limitations only occur at higher current densities.

Figure 3.19 depicts the local current distribution for the three cases investigated. As with previously investigated parameters, the channel width has a large impact on the local current density distribution. For the narrow channel the local current density can exceed 2.2 A / cm^2, and a large fraction of the overall current is being generated under the channel area. This maximum value is reduced to a value between 1.5 A / cm^2 and 1.6 A / cm^2 for a wider channel of 1.2 mm.

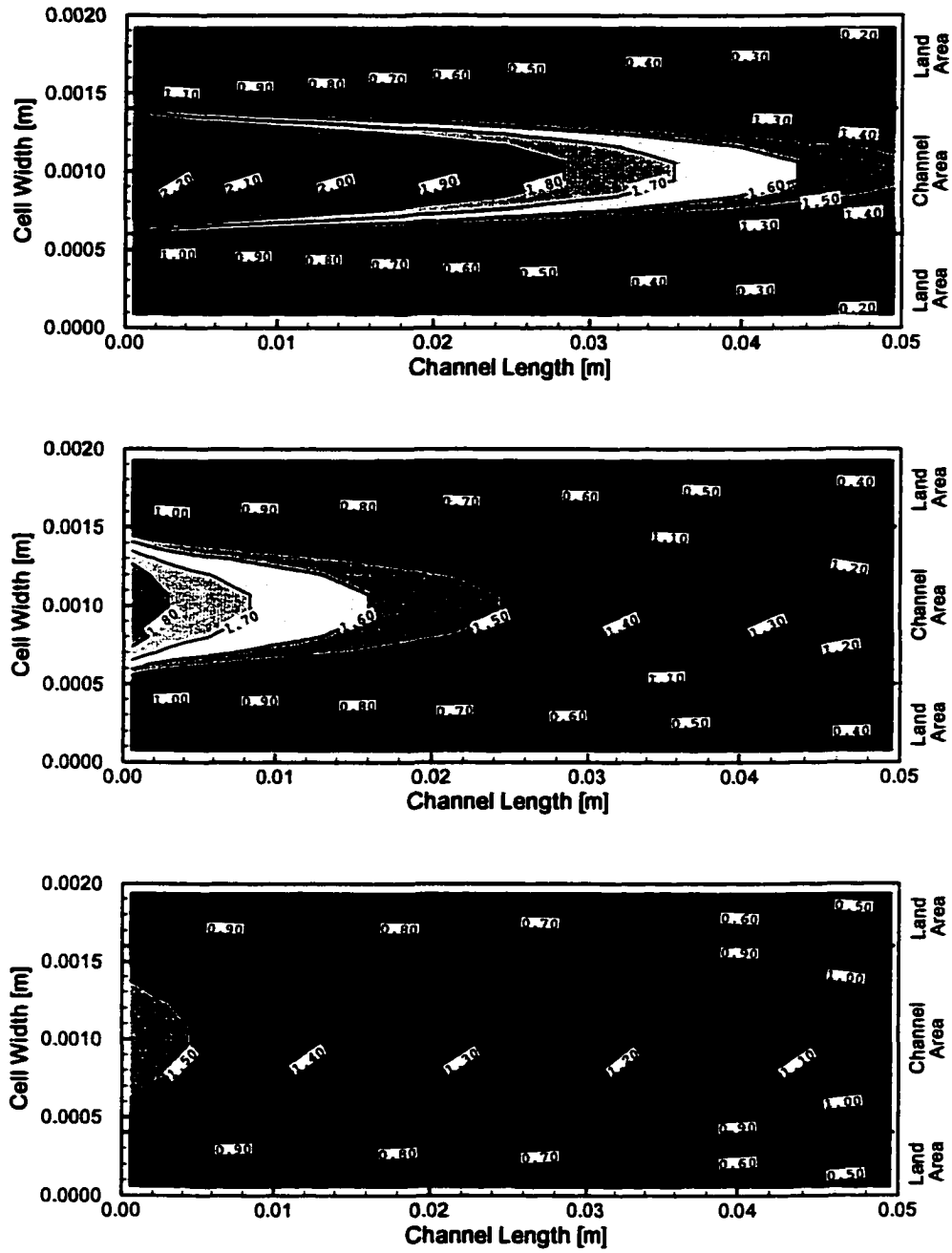

Figure 3.19: Local current density distribution for three different channel and land area widths: $Ch/L = 0.8\,\text{mm}/1.2\,\text{mm}$ (upper), $Ch/L = 1.0\,\text{mm}/1.0\,\text{mm}$ (middle) and $Ch/L = 1.2\,\text{mm}/0.8\,\text{mm}$ (lower). The nominal current density is $1.0\,\text{A}/\text{cm}^2$.

Finally, as mentioned before, the contact resistance between the graphite plates and the carbon fiber paper plays an important role, when judging the advantages of a wider channel. Again, a contact resistance of $0.03\,\Omega\,cm^2$ and $0.06\,\Omega\,cm^2$ was assumed, respectively. At an assumed contact resistance of $0.03\,\Omega\,cm^2$ all three different cases perform equally well in terms of the maximum power density. With a further increase, the case with the highest contact area starts to outperform the other two cases. Again, it has to be stretched that the values for the contact resistance are pure assumptions; it is not clear, how high the resistance can be under realistic operating conditions.

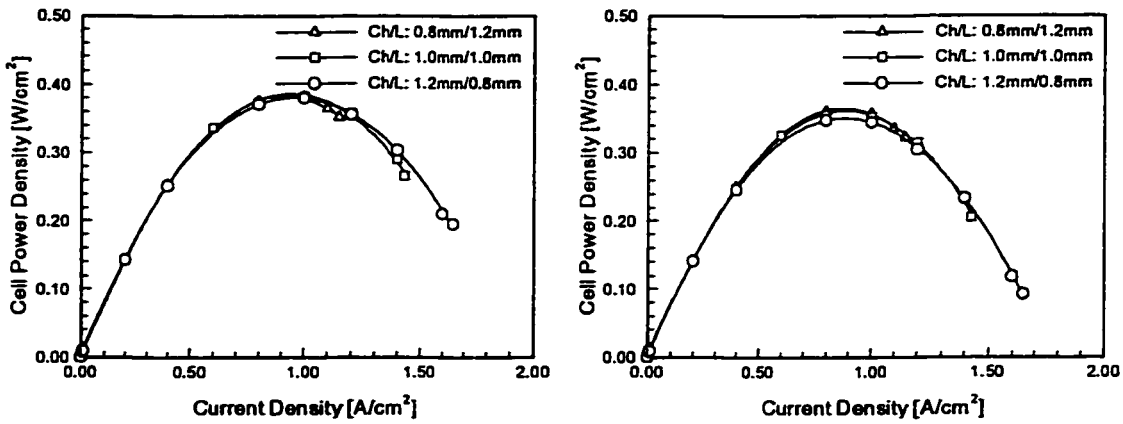

Figure 3.20: Power density curves for different assumed contact resistances: $0.03\,\Omega\,cm^2$ (left) and $0.06\,\Omega\,cm^2$ (right).

3.9 Summary

A detailed analysis of the fuel cell performance under various operating conditions has been conducted and the effects of temperature, pressure, stoichiometric flow ratio, oxygen content of the incoming air, as well as GDL thickness and porosity and channel width have been examined. In order to achieve good agreement with experimental results, functional relationships had to be developed between operating parameters, such as temperature and pressure, and input parameters for the computational model such as the exchange current density of the oxygen reduction reaction. The analysis helped identifying critical parameters and shed insight into the physical mechanisms leading to a fuel cell performance under various operating conditions. Furthermore, the study performed in this chapter helped to explain previously published experimental results by different research groups without knowledge of the exact conditions.

One of the major simplifications of the current model is the assumption that the volume of the liquid water inside the gas diffusion layers is negligible. Moreover, the gas and liquid phase are treated in separate computational domains, neglecting the interaction between the liquid water and the gas phase. In order to eliminate this shortcoming, a two-phase model has been developed, which will be presented in the following chapter.

Chapter 4

A Three-Dimensional, Two-Phase Model of a PEM Fuel Cell

4.1 Introduction

Using as a basis the one-phase model presented in Chapter 2, a two-phase model has been developed that accounts for both the gas and liquid phase in the same computational domain and thus allows for the implementation of phase change inside the gas diffusion layers. In addition, the computational domain was extended to include a cooling channel, which will allow to assess the impact of the coolant temperature and flow rate on the amount of liquid water inside the MEA under various operating conditions.

The multi-phase model presented here is different from those in the literature in that it is three-dimensional as opposed to two-dimensional (*e.g.* [18], [49]). Furthermore, it is non-isothermal and accounts for the physics of phase change in that the

rate of evaporation is a function of the amount of liquid water present and the level of undersaturation. The addition of a cooling channel is also a unique feature of the present model and enhancing its physical realism. Finally, the model is not limited to relatively low humidity reactants, as was the case in prior two-phase flow studies, and can be used to simulate conditions representative of actual fuel cell operation.

Similar to the models by Hen *et al.* [18] and Wang *et al.* [49], the current two phase study focuses on the gas-diffusion layer and the flow channels, neglecting the membrane. However, in contrast to these authors, the anode side is included in the present model as well. Water transport inside the porous gas diffusion layer is described by two physical mechanisms: viscous drag and capillary pressure forces. Liquid water, created by the electrochemical reaction and condensation, is dragged along with the gas phase. It will be shown below that at the cathode side, the humidity level of the incoming air determines whether this drag is directed into or out of the gas diffusion layer, whereas at the anode side this drag is always directed into the GDL. The capillary pressure gradient drives the liquid water out of the gas diffusion layers into the flow channels. This model is capable of identifying important parameters for the wetting behaviour of the gas diffusion layers and can be used to identify conditions that might lead to the onset of pore plugging, which has a detrimental effect of the fuel cell performance.

The simulations performed with the model will also show that phase change of water is controlled by three different, competing mechanisms: a rise in temperature leads to a rise in the saturation pressure and hence causes evaporation; the depletion of the reactants inside the gas-diffusion layers causes an increase in the partial pressure of the water vapour and can thus lead to condensation, whereas the pressure drop

inside the gas diffusion layers leads to a decrease in the pressure of the water vapour, and hence can cause evaporation.

4.2 Modelling Domain and Geometry

The modelling domain for the two-phase case is shown in Figure 4.1. The cooling water channel can be seen in the bottom of the domain. Because of the symmetry conditions applied, only one quarter of the channel has to be included. Since the liquid and the gas-phase are now accounted for in the same computational domain, the *Subdomain II* from the single-phase model is not required. However, heat transfer between the solid matrix and the gas-phase inside the gas-diffusion layers is still accounted for in the same fashion as in the single phase model (*Subdomain I*).

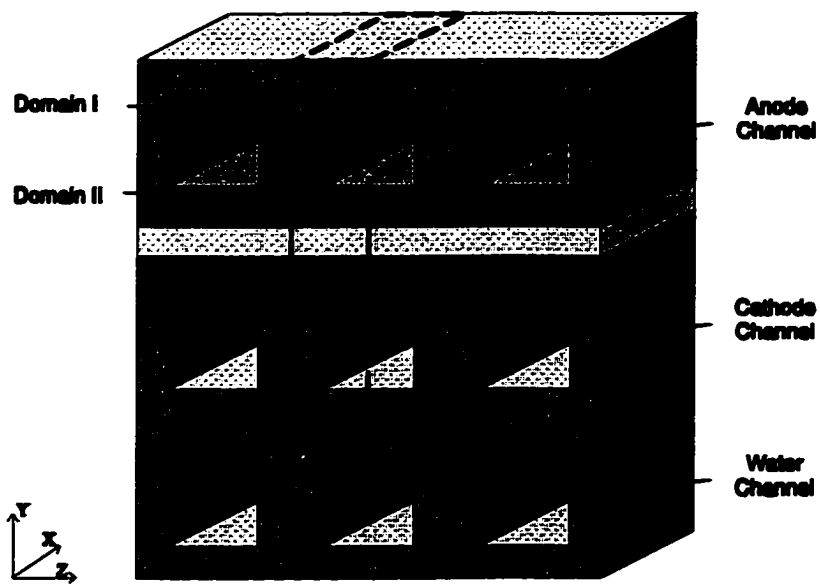

Figure 4.1: The modelling domain used for the two-phase computations.

Subdomain III, which was used to calculate the electrical potential inside the membrane, has been left out. The reason is that in the single phase model the potential distribution inside the membrane was used to calculate the liquid water flux, as described by the Schlögl equation. This, however, was found to be insufficient, and more elaborate models of the electrolyte membrane are highly empirical, with an unknown range of validity (*e.g.* Springer *et al.* [38]).

4.3 Assumptions

The assumptions made in the two-phase model are basically identical to the ones stated in Chapter 2.3. In order to implement the phase change of water, the following additional assumptions were made:

1. liquid water exists in the form of small droplets of specified diameter only,
2. inside the channels the liquid phase and the gas phase share the same pressure field,
3. equilibrium prevails at the interface of the water vapour and liquid water,
4. no other species exist in the liquid phase, *i.e.* it consists of liquid water only,
5. heat transfer between the gas-phase and the liquid water is idealized, *i.e.* both phases share the same temperature field, and
6. phase change occurs only within the porous electrodes, *i.e.* phase change of water inside the channels or at the channel/wall interfaces is not accounted for.

The first assumption has been made in order to find an expression for the rate of evaporation of water. However, it will be shown that the assumed size of the droplets has no impact on the modelling results, indicating "fast" evaporation.

The remaining assumptions are standard for the treatment of a multi-phase problem. The last assumption leads to exceedingly high relative humidities inside the flow channels, particularly when cooling is applied. However, for the current case we are predominantly interested in the phase change that occurs inside the electrodes in order to obtain the relative humidity at the electrode/membrane interface. The problem of having strong condensation terms at the channel/wall interfaces and the eventual appearance of rivulets is a complicated mathematical problem in itself and beyond the scope of this thesis.

4.4 Modelling Equations

The approach taken for the current model is to subdivide every control volume into volume fractions for the gas- and liquid phase. Hence, two sets of conservation equations for mass, momentum and energy are solved, which include the volume fraction of every phase. Mathematically, this approach is similar to the one taken for the flow through porous media, where the porosity was introduced in the Navier-Stokes equations to account for the reduced space available for the gas phase. However, in the multi-phase model, exchange terms exist between both phases, caused, for example, by the phase change of water. Thus, the volume fractions become part of the solution, and they result out of the mass conservation equations and the fact that the sum over all the volume fractions has to be equal to unity.

4.4.1 Main Computational Domain

Gas Flow Channels

The mass conservation equation for each phase yields the volume fraction r and along with the momentum equations the pressure distribution inside the channels. For the liquid phase the mass conservation equation has been adjusted to account for a diffusive term. This is coherent with the assumption that the liquid in the channel consists of small droplets only. Mathematically, this is expressed via:

$$\nabla \cdot \left(r_g \rho_g \mathbf{u}_g\right) = 0 \tag{4.1}$$

for the gas phase and

$$\nabla \cdot \left(r_l \rho_l \mathbf{u}_l\right) = \nabla \cdot \left(\rho_l D_l \nabla r_l\right) \tag{4.2}$$

for the liquid phase.

Two sets of momentum equations are solved in the channels, and it is assumed that they share the same pressure field:

$$p_g = p_l = p \tag{4.3}$$

Under these conditions, it can be shown that the momentum equations reduce to [6]:

$$\nabla \cdot \left[\left(\rho_g \mathbf{u}_g \otimes \mathbf{u}_g - \mu_g \left(\nabla \mathbf{u}_g + (\nabla \mathbf{u}_g)^T\right)\right)\right] = -r_g \nabla p \tag{4.4}$$

and

$$\nabla \cdot \left[\left(\rho_l \mathbf{u}_l \otimes \mathbf{u}_l - \mu_l \left(\nabla \mathbf{u}_l + (\nabla \mathbf{u}_l)^T\right)\right)\right] = -r_l \nabla p \tag{4.5}$$

Note that this form of the momentum equation assumes incompressible flow, which is the case for the liquid phase and a good approximation for the gas phase for a $Ma \prec 0.3$ [6].

Currently, no interaction between the phases in the form of a drag coefficient is considered inside the flow channels for the sake of simplicity.

The energy equation for each phase becomes:

$$\nabla \cdot \left[r_g \left(\rho_g \mathbf{u}_g H_g - \lambda_g \nabla T_g \right) \right] = 0 \tag{4.6}$$

and

$$\nabla \cdot \left[r_l \left(\rho_l \mathbf{u}_l H_l - \lambda_l \nabla T_l \right) \right] = 0 \tag{4.7}$$

Multiple species are considered in the gas phase only, and the species conservation equation in multi-component, multi-phase flow becomes:

$$\nabla \cdot \left[r_g \left(\rho_g \mathbf{u}_g y_{gi} - \rho_g D_{gii} \nabla y_{gi} \right) \right] = \nabla \cdot r_g \rho_g D_{gij} \nabla y_{gj} \tag{4.8}$$

where the term on the right-hand side arises because of the multi-component diffusion, as described in Appendix A. Note that in the two-phase case we are only dealing with a binary mixture at the anode side, *i.e.* hydrogen and water vapour. In this case, it can be shown that the source term on the right hand side becomes zero and the diffusivity D_{gii} reduces to the binary diffusivity of the two components [39].

The constitutive equations are the same as in the single phase case, that is the liquid phase is considered incompressible so that

$$\rho_l = \rho_w \tag{4.9}$$

and the ideal gas assumption leads to:

$$\rho_{gi} = \frac{p_g M_i}{RT}, \tag{4.10}$$

with the bulk density being:

$$\frac{1}{\rho_g} = \sum \frac{y_{gi}}{\rho_{gi}} \tag{4.11}$$

The sum of all mass fractions is equal to unity

$$\sum y_{gi} = 1, \tag{4.12}$$

and the molar fraction x is related to the mass fraction by:

$$x_{gi} = \frac{\frac{y_{gi}}{M_i}}{\sum \frac{y_{gi}}{M_i}}. \tag{4.13}$$

Overall, the flow in the channel is described as a standard dispersed two-phase flow, where the inter-phase drag is so strong that the velocity field is the same for both phases. The gas phase is considered as an ideal gas, and the liquid phase is incompressible. A change in the equations has been made in order to allow diffusion of the liquid droplets in the gas phase as a consequence of the small size of the droplets assumed.

Gas Diffusion Layers

For the conservation of mass, mass transfer in the form of evaporation and condensation is accounted for, so that the mass conservation equation results in:

$$\nabla \cdot \left((1-s)\,\varepsilon \rho_g \mathbf{u}_g \right) = \dot{m}_{evap} + \dot{m}_{cond} \tag{4.14}$$

and

$$\nabla \cdot (s\varepsilon \rho_l \mathbf{u}_l) = -\left(\dot{m}_{evap} + \dot{m}_{cond} \right) \tag{4.15}$$

Note that the *saturation* s is the same as the liquid water volume fraction r_l and has been introduced in order to keep with common notation. Since the sum of all volume fractions has to be equal to unity, the volume fraction of the gas phase r_g becomes $(1-s)$. In every given control volume, either evaporation or condensation can occur, depending on the relative humidity. The sign definition adopted here is positive for evaporation and negative for condensation.

The momentum equation for the gas-phase is again reduced to Darcy's law, which is, however, based on the *relative permeability* for the gas phase k_p^g. The relative permeability accounts for the reduction in pore volume available for one phase due to the existence of the second phase [47]. Different approaches can be adapted to mathematically describe of the relative permeability, the simplest of which has been used in the current model [18]:

$$k_p^g = (1-s) \cdot k_p^0 \tag{4.16}$$

and

$$k_p^l = s \cdot k_p^0 \tag{4.17}$$

where k_p^0 is the permeability of the dry electrode and s is again the saturation of liquid water inside the GDL [18]. With this, the momentum equation for the gas phase inside the gas diffusion layer becomes:

$$\mathbf{u}_g = -\frac{k_p^g}{\mu_g}\nabla p_g = -(1-s)\frac{k_p^0}{\mu_g}\nabla p_g \tag{4.18}$$

Transport of the liquid water is considered via two mechanisms: a shear term drives the liquid phase along with the gas phase in the direction of the pressure gradient, and capillary forces drive the liquid water from regions of high saturation towards regions of low saturation [18]. Starting from Darcy's law, we can write:

$$\mathbf{u}_l = -\frac{k_p^l}{\mu_l}\nabla p_l \tag{4.19}$$

where the liquid water pressure results out of the gas-phase pressure p_g and the capillary pressure p_c according to [47]:

$$\nabla p_l = \nabla p_g - \nabla p_c = \nabla p_g - \frac{\partial p_c}{\partial s}\nabla s \tag{4.20}$$

Introducing this expression into Equation 4.19 yields for the liquid water velocity field:

$$\mathbf{u}_l = -\frac{k_p^l}{\mu_l}\nabla p_g + \frac{k_p^l}{\mu_l}\frac{\partial p_c}{\partial s}\nabla s = -s\frac{k_p^0}{\mu_l}\nabla p_g - \mathfrak{D}(s)\nabla s \tag{4.21}$$

where the diffusivity $\mathfrak{D}(s)$ is defined as [47]:

$$\mathfrak{D}(s) = -s\frac{k_p^0}{\mu_l}\frac{\partial p_c}{\partial s} \tag{4.22}$$

For the description of the capillary pressure as a function of the saturation $p_c(s)$, Leverett [24] has shown that under idealized conditions the capillary pressure versus saturation data can be cast in the following form:

$$p_c = \sigma \left(\frac{\varepsilon}{k_p^0} \right)^{1/2} f(s) \tag{4.23}$$

where σ is the interfacial liquid/gas tension, ε is the porosity and the function $f(s)$ is determined using Udell's expression [43]:

$$f(s) = 1.417(1-s) - 2.12(1-s)^2 + 1.263(1-s)^3 \tag{4.24}$$

which has also been adopted by Wang *et al.* [49].

Different species are only considered in the gas phase, and the species conservation equation is the same as in the one-phase computations, except for the consideration of the volume fraction for each phase r_g:

$$\nabla \cdot \left[r_g \left(\varepsilon_g \rho_g \mathbf{u}_g y_{gi} - \varepsilon_g \rho_g D_{gii} \nabla y_{gi} \right) \right] = \varepsilon_g \nabla \cdot \left(r_g \rho_g D_{gij} \nabla y_{gj} \right) \tag{4.25}$$

This equation makes it obvious that the subdivision of a control volume into volume fractions is analogous to considering a porous medium, where only part of the control volume is accessible to the gas phase: r_g and ε_g are inter-changeable, except that r_g is a variable that is solved for by the continuity equations. The term on the right hand side is again due to the multi-species diffusion, as described in Chapter 2.4. Equation 4.25 is valid for species that do not undergo phase change.

For the water vapour inside the gas phase, the equation reads as follows:

$$\nabla \cdot \left[r_g \left(\varepsilon_g \rho_g \mathbf{u}_g y_{gw} - \varepsilon_g \rho_g D_{gii} \nabla y_{gw} \right) \right] = \varepsilon_g \left[\nabla \cdot \left(r_g \rho_g D_{gij} \nabla y_{gw} \right) + \dot{m}_{evap} + \dot{m}_{cond} \right] \tag{4.26}$$

where only one of the phase change terms can exist, evaporation or condensation. Because of the sign convention adopted here the condensation term is negative (see below).

The energy equation becomes:

$$\nabla \cdot \left[r_g \left(\varepsilon_g \rho_g \mathbf{u}_g h_{tot} - \varepsilon_g \lambda_g \nabla T_g \right) \right] = \beta \left(T_s - T_g \right) - \varepsilon_g \left(\dot{m}_{evap} + \dot{m}_{cond} \right) \Delta h_{evap} \tag{4.27}$$

where Δh_{evap} denotes the heat of evaporation or condensation in [J / kg] at 80 °C. The gas phase and the liquid phase are assumed to be in thermodynamic equilibrium, hence the temperature of the liquid water is the same as the gas phase temperature.

Implementation of Phase Change An important feature of this model is that it accounts for the physics of phase change, which has so far been neglected in other studies. The multi-phase model by Wang *et al.* [49] is based for instance on an isothermal assumption. In that work the relative humidity of water is calculated throughout the domain, and if it exceeds 100%, it is concluded that condensation happens here, whereas if it is less than 100% in the presence of liquid water, evaporation occurs. The amount of water undergoing phase-change is calculated *a posteriori*, based on consideration of the calculated concentration of water in any given control volume versus the saturation concentration, based on the saturation pressure as a function of temperature. This approach has one distinct weakness: the heat of evaporation

and condensation for the amount of water undergoing phase change is not accounted for. Consequently, the saturation pressure is always constant due to the isothermal assumption.

The effect of the temperature distribution on phase change is generally well understood and can be described as follows: when the (fully saturated) gas reaches the vicinity of the catalyst layer of the fuel cell, it heats up due to the heat produced by the electrochemical reaction. Consequently, the temperature increases. Since the saturation pressure is a function of temperature only, it increases as well, and the gas becomes undersaturated. This undersaturation creates a driving mechanism for the evaporation of liquid water, which is formed during the electrochemical reaction. Hence, phase change occurs already at the inlet area of the cathode gas. This evaporation induces cooling of the gas phase. This shows that there is a fine balance for evaporation/condensation, with the temperature being the determining factor. Obviously, an isothermal model can not account for that, and has a limited physical representation.

In order to account for the magnitude of phase change that occurs inside the GDL, an expression had to be found that relates the level of over- and undersaturation as well as the amount of liquid water to the rate of phase change.

Initially, the focus was directed on the expression for evaporation. This must be related to (*i*) the level of undersaturation of the gas phase in each control volume and (*ii*) the surface area of the liquid water in the control volume. The surface area can be assumed proportional to the volume fraction of the liquid water in each cell. An obvious choice for the shape of the liquid water is droplets, especially because the

catalyst area is coated with Teflon. In addition, the rate of evaporation of a single droplet in a free stream is well understood.

The evaporation of a droplet in a convective stream has been described by Bird, Steward and Lightfoot [10]. The flux of water due to phase change is:

$$\dot{N}_w = k_{xm}\pi D^2 \frac{x_{w0} - x_{w\infty}}{1 - x_{w0}} \tag{4.28}$$

where D is the diameter of the droplet, x_{w0} is the molar concentration of water at the interface, $x_{w\infty}$ is the bulk concentration of water vapour (in this case the molar concentration of water vapour in each control volume), k_{xm} is the transfer rate of water in $[\mathrm{mol}/(\mathrm{m}^2\,\mathrm{s})]$ and $\dot{N}_w$ is the flux of water from the liquid phase into the gas phase in $[\mathrm{mol}/\mathrm{s}]$. The bulk concentration $x_{w\infty}$ is known by solving the continuity equation of water. For the concentration of water vapour at the surface, thermodynamic equilibrium between the liquid phase and the gas phase is assumed. Under that condition, the surface concentration can be calculated out of the saturation pressure at the temperature of the control volume.

The mass transfer coefficient k_{xm} is analogous to a heat transfer coefficient, and reliable correlations are available for the heat transfer coefficient for convection around a sphere, so that the mass transfer coefficient k_{xm} [10] can be obtained from:

$$k_{xm} = \frac{c_g \mathfrak{D}_{wg}}{D}\left[2.0 + 0.60\left(\frac{D v_\infty \rho_g}{\mu_g}\right)^{1/2}\left(\frac{\mu_g}{\rho_g \mathfrak{D}_{wg}}\right)^{1/3}\right] \tag{4.29}$$

where c_g is the concentration of air in $[\mathrm{mol}/\mathrm{m}^3]$, $\mathfrak{D}_{wg}$ is the diffusion coefficient of water-vapour in air in $[\mathrm{m}^2/\mathrm{s}]$, v_∞ is the free-stream velocity in $[\mathrm{m}/\mathrm{s}]$ and ρ_g is the

air density in [kg / m^3]. All these properties can be easily calculated to facilitate the implementation of phase change.

It is assumed that all droplets have a specified diameter D, and the number of droplets in each control volume is found by dividing the total volume of the liquid phase in each control volume by the volume of one droplet:

$$n_{D,CV} = \frac{r_l V_{CV}}{\frac{1}{6}\pi D^3} \tag{4.30}$$

The foregoing derivation is valid for a single drop in free convection. Because of the uncertainty about the droplet size, along with the fact that inside the porous medium we are not dealing with free convection, the overall expression is scaled by a factor ϖ:

$$\dot{N}_w = \varpi n_{D,CV} c_g \mathfrak{D}_{wg} \left[2.0 + 0.60 \left(\frac{D v_\infty \rho_g}{\mu_g} \right)^{1/2} \left(\frac{\mu_g}{\rho_g \mathfrak{D}_{wg}} \right)^{1/3} \right] \pi D \frac{x_{w0} - x_{w\infty}}{1 - x_{w0}} \tag{4.31}$$

When the solution indicates that the relative humidity inside the porous medium is close to 100% for several orders of magnitude of ϖ smaller than 1.0, the rate of evaporation is indeed fast enough to justify the assumption made by other groups of having a fully humidified gas phase.

Finally, in order to obtain the mass flux caused by evaporation, the above expression has to be multiplied with the molar mass of water, which results in the amount of water undergoing evaporation in [kg / s] *in each control volume*:

$$\dot{m}_{evap} = M_{H_2O} \varpi n_{D,CV} k_{xm} \pi D \frac{x_{w0} - x_{w\infty}}{1 - x_{w0}} \tag{4.32}$$

In case the relative humidity exceeds 100%, condensation occurs and the evaporation term is switched off. The case of condensation is more complex, because it can occur on every solid surface area, but the rate of condensation changes depending on the surface conditions such as the water coverage [3]. In addition, the overall surface area in each control volume available for condensation shrinks with an increasing amount of liquid water present. It is currently assumed that the rate of condensation depends only on the level of oversaturation of the gas phase multiplied by a constant. For high levels of liquid saturation, this expression will have to be revised in the future.

$$\dot{m}_{cond} = \varpi C \frac{x_{w0} - x_{w\infty}}{1 - x_{w0}} \tag{4.33}$$

Note that because in this case the bulk concentration $x_{w\infty}$ exceeds the surface concentration resulting out of the temperature, x_{w0}, the overall mass flux through condensation is negative, *i.e.* from the gas phase to the liquid phase.

Catalyst Layers

The sink and source terms applied at the catalyst layer are the same as those in Chapter 2.4, except that the source term for liquid water at the cathode side is now accounted for in the main computational domain:

$$S_{H_2O_{(l)}} = M_{H_2O} \frac{i}{2F} \tag{4.34}$$

where the local current density i is again obtained using the Butler-Volmer equation under the assumption of a constant activation overpotential.

Bipolar Plates

As before, only conductive heat transfer is accounted for in the bipolar plates. The equation solved is:

$$\nabla \cdot (\lambda_{gr} \nabla T) = 0 \tag{4.35}$$

where the subscript "*gr*" denotes graphite.

Water Cooling Channel

In the channels, the Navier-Stokes equations for laminar, incompressible flow are solved. These are the continuity equation:

$$\nabla \cdot (\rho_l \mathbf{u}_l) = 0, \tag{4.36}$$

the momentum equation:

$$\nabla \cdot (\rho_l \mathbf{u}_l \otimes \mathbf{u}_l - \mu_l \nabla \mathbf{u}_l) = -\nabla \left(p_l + \frac{2}{3} \mu_l \nabla \cdot \mathbf{u}_l \right) + \nabla \cdot \left[\mu_l \left(\nabla \mathbf{u}_l \right)^T \right] \tag{4.37}$$

and the energy equation:

$$\nabla \cdot (\rho_l \mathbf{u}_l H_l - \lambda_l \nabla T_l) = 0. \tag{4.38}$$

where the total enthalpy H is calculated out of the static (thermodynamic) enthalpy h via:

$$H_l = h_l + \frac{1}{2} \mathbf{u}_l^2, \tag{4.39}$$

The fluid in the cooling channels is assumed to be liquid water only, hence, no additional species equation need to be solved.

4.4.2 Computational Subdomain I

The equations solved in this computational domain correspond exactly to the ones given in Chapter 2.4.

4.5 Boundary Conditions

For the main computational domain, the same boundary conditions are applied as in the one-phase model. Again, the inlet velocity is a function of the desired current density and the stoichiometric flow ratio. The gas streams entering the cell are fully humidified, but no liquid water is contained in the gas stream. At the outlets, the pressure is prescribed and it is assumed that the flow is fully developed, *i.e.* the axial gradients for all transport variables are set to zero.

Symmetry boundaries are applied at the z- and y- interfaces, so that this case simulates an endless number of parallel channels, with one cooling channel for every two active cells, which are connected in an anode-to-anode and cathode-to-cathode fashion. Therefore, only half the flow channels and a quarter of the cooling channel have to be modelled, which saves valuable computational cells and CPU time.

At the inlet of the water cooling channel, the velocity is given as well as the temperature, whereas the pressure is given at the outlet, again assuming fully developed flow.

4.6 Modelling Parameters

The geometry used for the two-phase case is summarized in Table 4.1. In order to reduce the computational overhead of the otherwise demanding two-phase model, the

length of the computational domain has been reduced to 3 cm. Otherwise the channel dimensions are the same as before.

Table 4.1: Geometrical and material parameters at base case

Parameter	Symbol	Value	Unit
Channel length	l	0.03	m
Channel height	h	1.0×10^{-3}	m
Channel width	w_c	1.0×10^{-3}	m
Land area width	w_l	1.0×10^{-3}	m
Electrode thickness	t_e	0.20×10^{-3}	m
Membrane thickness	t_{mem}	0.23×10^{-3}	m
Electrode porosity	ε	0.5	–
Hydraulic permeability	k_p^0	1.0×10^{-14}	m^2

The porosity of the gas-diffusion layer ε has been increased from 0.4 to 0.5. The permeability of the electrode was adjusted to a larger value in order to allow comparisons with Wang *et al.* [49] and He *et al.* [18].

Table 4.2 lists the operational conditions of the base case. The cooling water enters at the operating temperature of the cell at a specified flow rate. Apart from that the conditions are standard with stoichiometric flow ratios in a realistic range.

Note that in the current simulations, only a binary mixture of hydrogen and water vapour is considered at the anode side. The gas enters fully humidified, *i.e.* the molar fraction of water vapour is pre-defined out of the temperature of the humidifier and the gas phase pressure.

Table 4.2: Geometrical, operational and material parameters at base case

Parameter	Symbol	Value	Unit
Inlet fuel and air temperature	T	80	°C
Inlet water temperature	T_w	80	°C
Inlet water velocity	$u_{w,in}$	0.5	m / s
Air side pressure	p_c	1	atm
Fuel side pressure	p_a	1	atm
Air stoichiometric flow ratio	ζ_c	3	–
Fuel stoichiometric flow ratio	ζ_a	3	–
Relative humidity of inlet gases	ξ	100	%
Oxygen/Nitrogen ratio	ψ	0.79/0.21	–

The parameters introduced to account for the multi-phase flow and phase change phenomena are listed in Table 4.3. Except for the water vapour diffusivity $\mathfrak{D}_{wg}$, which was taken from Bird *et al.* [10], all these parameters had to be estimated, but it was made sure that none of these was critical for the results.

Table 4.3: Multi-phase parameters of the current model

Parameter	Symbol	Value	Unit
Droplet diameter	D	1.0×10^{-8}	m
Water droplet diffusivity	D_l	1.0×10^{-8}	m^2 / s
Condensation constant	C	1.0×10^{-5}	–
Water vapour diffusivity	$\mathfrak{D}_{wg}$	2.92×10^{-5}	m^2 / s

4.7 Results

4.7.1 Basic Considerations

Before presenting and analyzing the results in detail, some of the physics of phase change shall be described. This will help understanding and interpreting the results shown below.

The central property for phase change is the relative humidity of the gas phase, given by:

$$\xi = \frac{p_{H_2O}}{p_{sat}(T)} \tag{4.40}$$

i.e. it is the fraction between the partial pressure of the water vapour in the gas phase and the saturation pressure p_{sat}, which is a function of temperature. According to Dalton's law the partial pressure of a species i is equal to its molar fraction x_i multiplied with the total pressure of the gas phase p_g [25], which gives:

$$\xi = x_{H2O}\frac{p_g}{p_{sat}(T)} \tag{4.41}$$

If the relative humidity is below 1.0 (or 100%) in the presence of liquid water, this will give rise to evaporation. Condensation will occur when the relative humidity exceeds 100% in the presence of condensation surfaces, which are abound inside the gas diffusion layer. The gas diffusion layer of a PEM Fuel Cell is particularly interesting for phase change considerations, because all three parameters on the right hand side of equation 4.41 vary, causing the following direction of phase change:

- *the molar water fraction* x_{H2O} increases inside the cathodic GDL, because of consumption of reactants. Provided the relative humidity of the incoming air is at 100%, this effect alone would lead to condensation of liquid water.

- *the thermodynamic pressure* p_g of the gas phase changes inside the GDL. This leads to a very interesting effect and, depending on the incoming gas condition, it can yield either evaporation or condensation. In the first place, there is a pressure drop inside the GDL due to the fact that oxygen is being consumed out of the gas phase. As a result, the bulk velocity of the gas phase is directed into the GDL, as described by Darcy's law. The pressure drop inside the GDL depends strongly on the permeability. For a low permeability, the pressure drop is large, and so the partial pressure of the water vapour decreases. This effect alone leads to an undersaturation, causing evaporation. A special case arises when the incoming air is relatively dry, in which case most of the product water will evaporate. Now, from the balanced cathodic reaction, every oxygen molecule creates two water molecules, and this causes a pressure increase. As a result, the bulk flow of the gas phase is directed from the catalyst layer towards the channel. This effect can be observed in Wang's simulations [49], which were performed for a low humidification level of the incoming gas. This means that the oxygen has to diffuse towards the catalyst interface against the bulk flow of the gas phase, which causes in turn a decrease in the maximum attainable current density.

- *the saturation pressure* $p_{sat}(T)$ increases with an increase in temperature, caused by the heat production term due to the electrochemical reaction. The order of temperature increase depends mainly on the thermal conductivity of the

gas-diffusion layer. The single-phase model has shown that for a thermal conductivity of $60\,\mathrm{W/(m\,K)}$ the temperature can rise by a few degrees Kelvin, whereas a study conducted by Dutta [36] shows that for a thermal conductivity of $6.0\,\mathrm{W/(m\,K)}$, the temperature increase can be as high as $10\,\mathrm{K}$. In any case, this increase in temperature alone would lead to evaporation of liquid water.

Clearly, all these three effects are of importance, demonstrating the importance of conducting a detailed computational analysis. Note that the first two effects are also of importance inside the gas flow channels: the depletion of the reactants from the inlet towards the outlet will create oversaturation and gives rise to condensation at the walls and the channel/GDL interface, whereas the overall pressure drop along the channel alone would cause evaporation. For the straight channel section considered here, the total pressure drop is relatively small and so the oxygen depletion effect dominates. Again, all this is only valid when the incoming air is at a high humidification level.

In addition, all three of these mechanisms apply to the anode as well as the cathode of a fuel cell. Recent studies of the two-phase flow inside the fuel cell have been confined to the cathode side only ([18, 49]). It will be shown in the results section that in the anodic gas diffusion layer and along the anode channel a significant amount of water condenses, which leads to the build-up of a capillary pressure at the anode side as well. This is of importance, because typically the anode side of the membrane is the one prone to dry out, and in the past, several humidification schemes have been proposed in order to prevent this (*e.g.* [28]). The results presented here will show that a proper choice of material parameters has a large impact on the amount of liquid water in the operating fuel cell.

4.7.2 Base Case Results

For the discussion of the results, the emphasis will be on the gas diffusion layers, because this is, where the two-phase flow is most important. One of the uncertainties of the current model was the introduction of the scaling parameter ϖ into the phase change equations. Figure 4.2 shows the relative humidity inside the cathodic gas diffusion layer for two different values of ϖ. The lower boundary represents the channel/GDL interface, whereas the upper boundary is the cathodic catalyst layer. It can be seen that the relative humidity is very close to 100% throughout the entire domain in both cases. Towards the catalyst layer, the humidity level increases due to the oxygen consumption. It is important to note that the humidity is always at least 100%, which means that the evaporation is indeed fast for low values of ϖ. Hence, in the following the scaling value ϖ has been kept at 0.01.

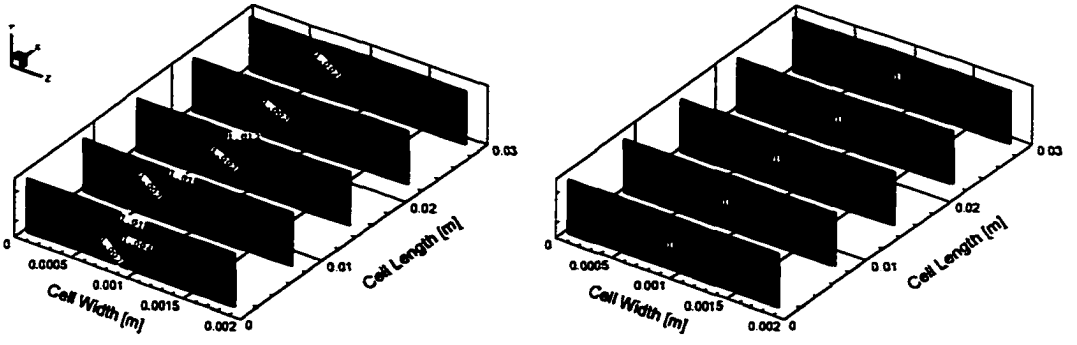

Figure 4.2: Relative humidity inside the cathodic gas diffusion layer for a scaling factor of $\varpi = 0.001$ (left) and $\varpi = 0.01$ (right). The current density is $1.2\,\mathrm{A}\,/\,\mathrm{cm}^2$.

Cathode Side

Figure 4.3 shows the by now familiar plot of the molar oxygen concentration at the cathodic catalyst layer versus current density. For the current densities investigated here, the drop is almost linear, and the expected maximum current density is around $1.6\,\mathrm{A/cm^2}$. Compared to the single phase results, this relatively high limiting current density can be attributed to the decrease in the GDL thickness and the increase in porosity, whereas the relatively low value for the oxygen concentration at a low current density results from the operating pressure of 1 atm.

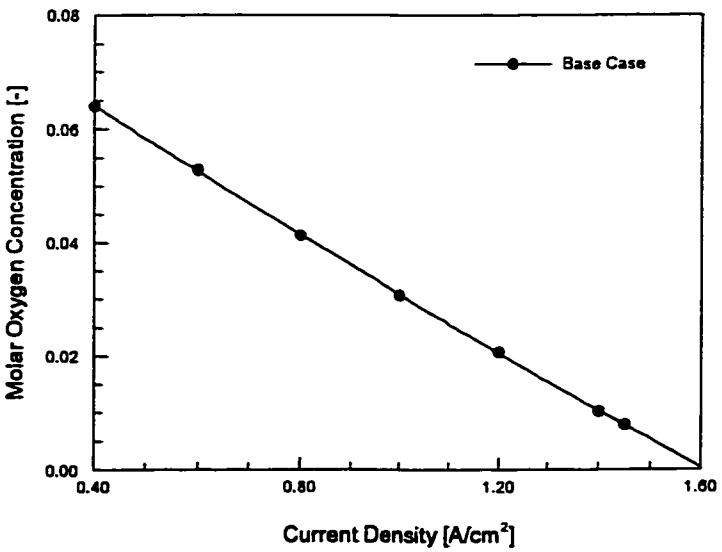

Figure 4.3: Average molar oxygen concentration at the cathodic catalyst layer as a function of current density.

The detailed distribution of the reactants inside the cathodic gas diffusion layer is shown in Figure 4.4. In this and the following plots, the channel/GDL interface is

located at the bottom of each graph, and the catalyst layer is at the top. The gas flow inside the channel is in the positive x-direction. It can be seen from the graph that, similar to the single phase computations, the oxygen depletion is strongest under the land areas and increases with current density. In the absence of phase change, this would mean that the molar water vapour fraction increases. However, the simulation yields almost uniform concentration of water vapour, with values ranging from 46.4% to 47.2%. This can only be the result of phase change occurring inside the gas diffusion layer.

The pressure and temperature distribution inside the cathodic gas diffusion layer are shown in Figure 4.5. The pressure drop increases for an increase in the current density from $0.4\,\mathrm{A}/\mathrm{cm}^2$ to $0.8\,\mathrm{A}/\mathrm{cm}^2$, which is due to the higher rate of oxygen depletion. For a further increase in the current density to $1.2\,\mathrm{A}/\mathrm{cm}^2$, however, the pressure drop becomes less, with the maximum being 2200 Pa compared to 2400 Pa at $0.8\,\mathrm{A}/\mathrm{cm}^2$. As will be shown below, this can be attributed to the evaporation of liquid water, particularly under the land areas.

A further indication of this can be found, when considering the temperature distribution. For all current densities, the temperature drops below the inlet value of 353 K under the land areas. This drop in temperature increases with current density. In addition, a slight increase in temperature can be observed at the catalyst layer. This can be due to two different causes, one being the heating term due to the electrochemical reaction, the other being a condensation term, caused by the increase in the molar water vapour fraction in this area. The temperature also increases at the channel/GDL interface. This must be attributed to the condensation that occurs here as a result of the depletion of the oxygen out of the bulk mixture. Overall, the

temperature distribution inside the gas diffusion layer is fairly uniform, which would seem to justify the isothermal assumption made by different authors (Wang *et al.* [49] and He *et al.* [18]). However, it is important to realize that the temperature distribution becomes uniform *as a result* of the heat of evaporation/condensation accounted for. By neglecting the effect of the local temperature distribution on the saturation pressure, one out of the three mechanisms leading to phase change as described above is not accounted for.

The rate of phase change and the liquid water saturation inside the cathodic gas diffusion layer are shown in Figure 4.6. As was already deduced from the temperature distribution, there are three main areas, where phase change occurs. Evaporation (positive values) prevails under the land areas, where the pressure drop is highest, which leads to a drop in the water vapour pressure and hence to undersaturation. Condensation (negative values) occurs mainly in two areas: at the catalyst layer the molar water vapour fraction increases due to the oxygen depletion, and at the channel/GDL interface, where the oversaturated bulk flow condenses out. This term is relatively small compared to the other effects.

The resulting liquid water distribution can be seen on the right hand side of Figure 4.6. The values range from 2% at the channel/GDL interface to 10% under the land areas. A gradient in the liquid water saturation is necessary for the liquid water to be driven out of the GDL by capillary forces. A sharp increase of the saturation exists inside the GDL at the border between the channel area and the land area, whereas under the land area the values are fairly constant. Also, the liquid water saturation appears to be increasing with an increase in the current density. This will be discussed in detail, later.

Finally, Figure 4.7 shows the velocity vectors for both phases inside the cathodic gas diffusion layer. The bulk flow of the gas phase is directed from the channel towards the catalyst layer, driven by the pressure gradient. It was already mentioned that when the rate of evaporation is high, *i.e.* when the humidity level of the incoming gas stream is low, the pressure gradient will be directed from the catalyst layer towards the channel, and the velocity vectors of the gas phase would point out of the GDL, as has been observed by Wang *et al.* [49]. The flux of the liquid water is directed towards the flow channel, where it can leave the cell. The velocity of the liquid phase, however, is much lower than for the gas phase, which is due to the higher viscosity. The liquid water "oozes out" of the GDL, mainly at the corners of the GDL/channel interface.

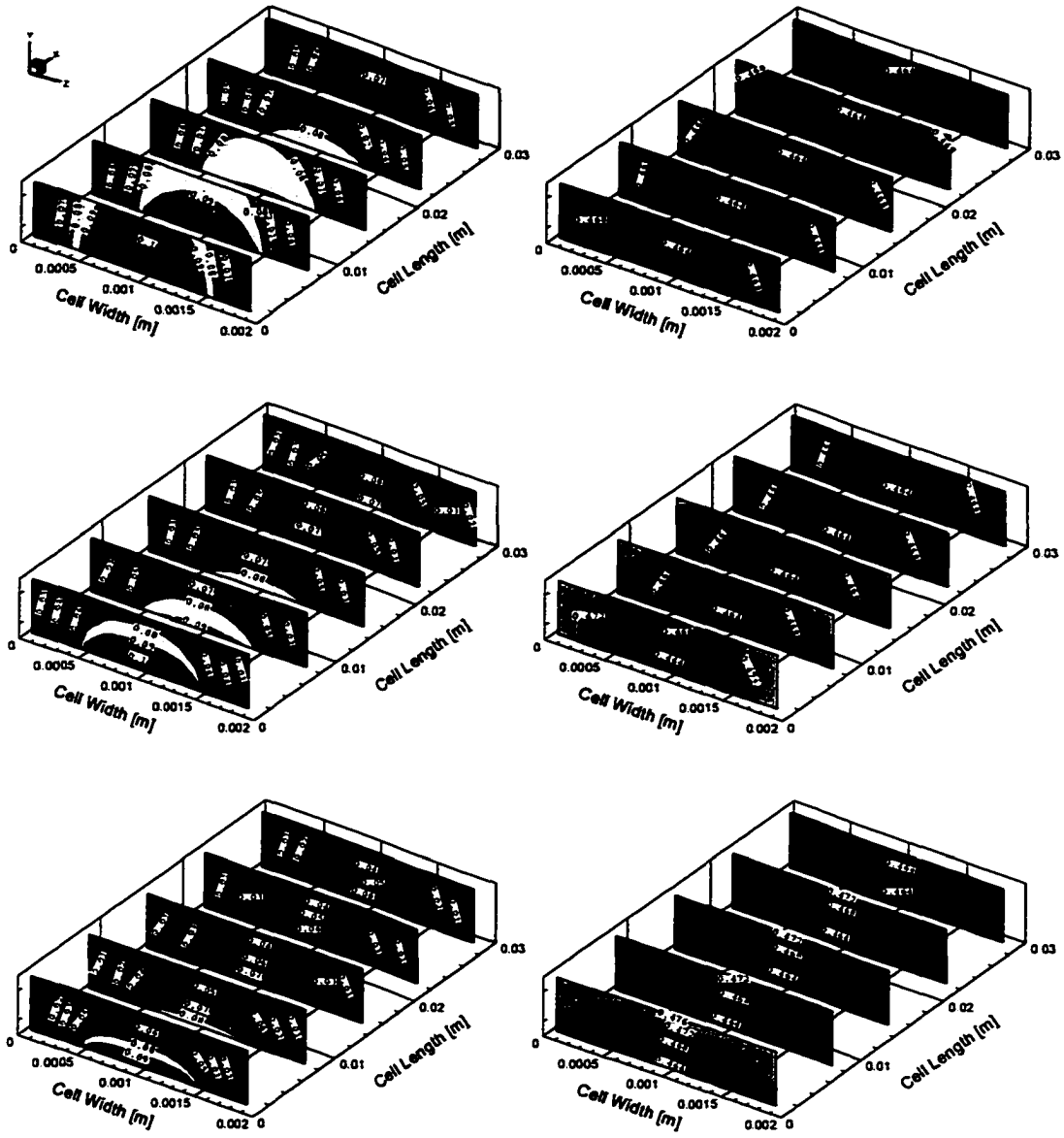

Figure 4.4: Molar oxygen concentration (left) and water vapour distribution (right) inside the cathodic gas diffusion layer for three different current densities: $0.4\,\mathrm{A}/\mathrm{cm}^2$ (top), $0.8\,\mathrm{A}/\mathrm{cm}^2$ (centre) and $1.2\,\mathrm{A}/\mathrm{cm}^2$ (bottom).

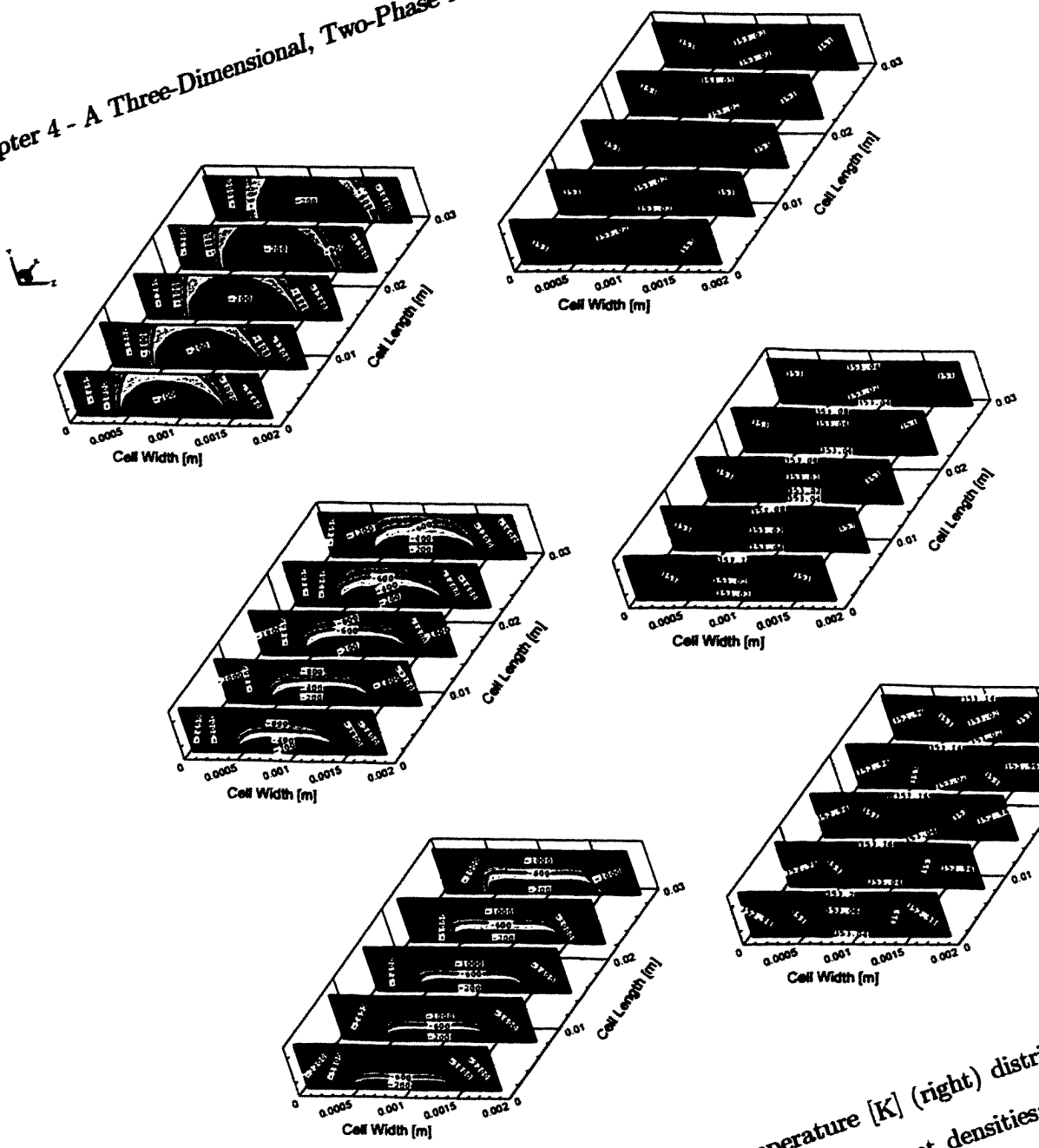

Figure 4.5: Pressure [Pa] (left) and temperature [K] (right) distribution inside the cathodic gas diffusion layer for three different current densities: 0.4 A / cm^2 (top), 0.8 A / cm^2 (centre) and 1.2 A / cm^2 (bottom).

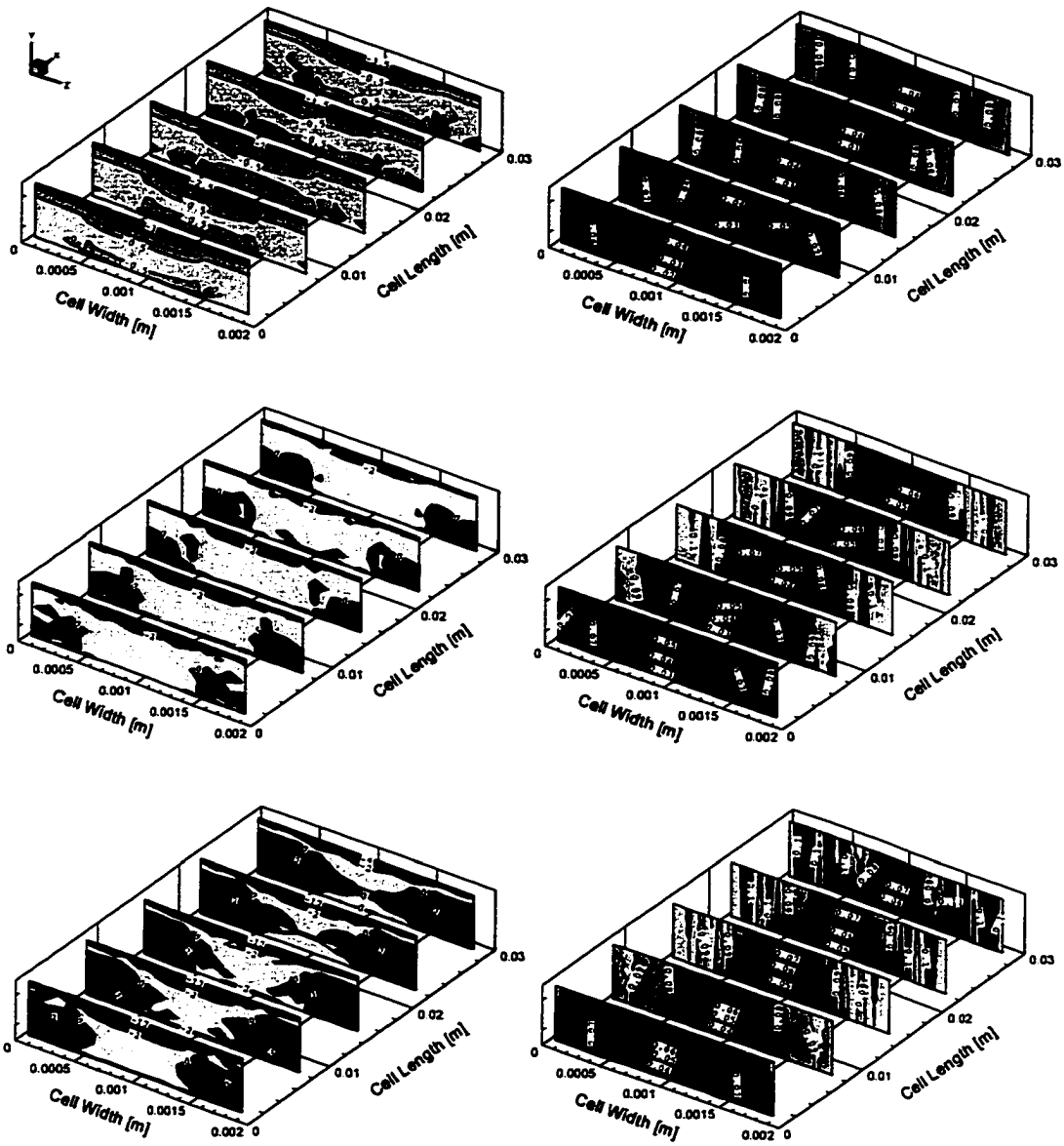

Figure 4.6: Rate of phase change [kg / (m^3 s)] (left) and liquid water saturation [−] (right) inside the cathodic gas diffusion layer for three different current densities: 0.4 A / cm^2 (top), 0.8 A / cm^2 (centre) and 1.2 A / cm^2 (bottom).

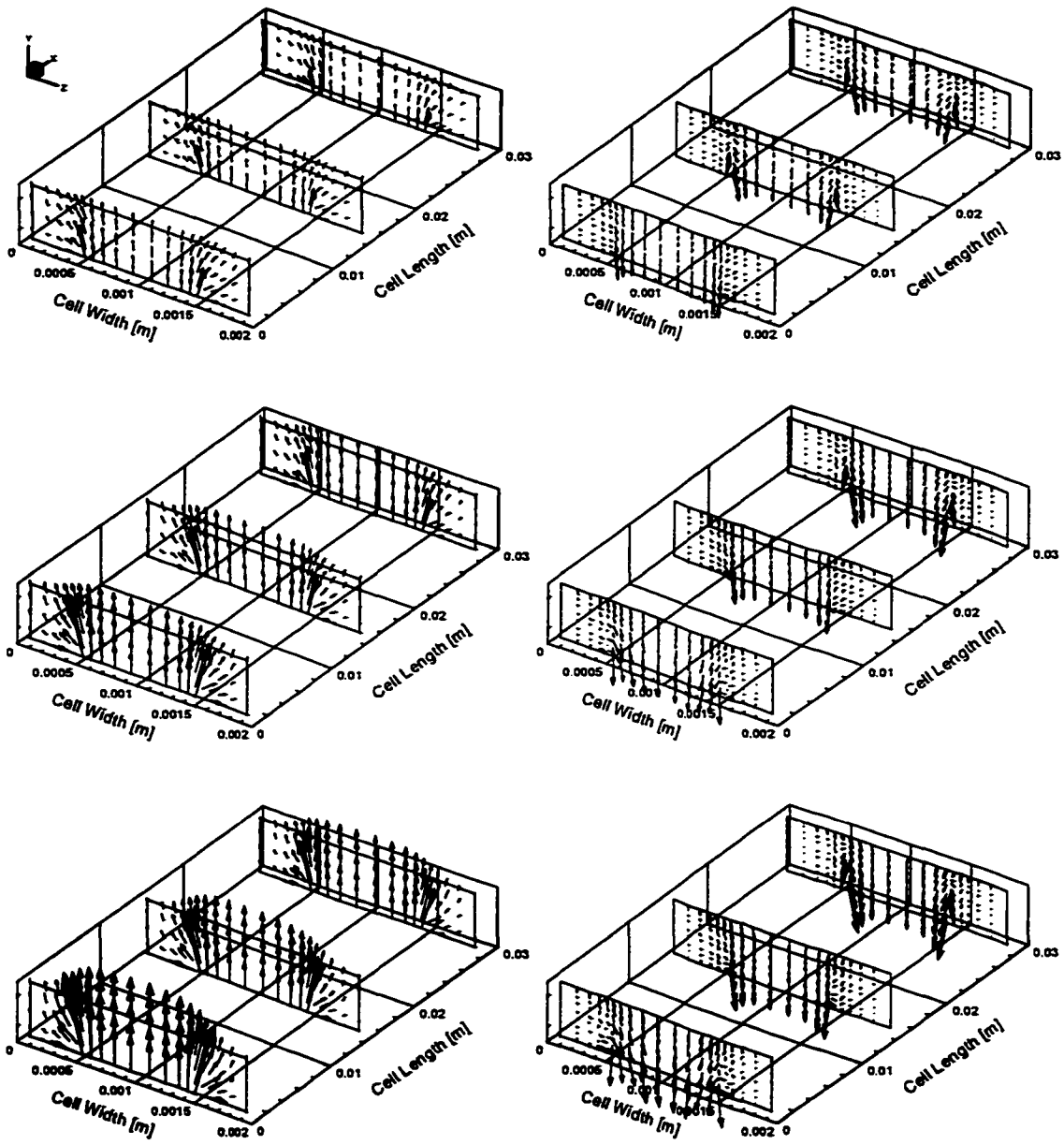

Figure 4.7: Velocity vectors of the gas phase (left) and the liquid phase (right) inside the cathodic gas diffusion layer for three different current densities: $0.4\,\mathrm{A}/\mathrm{cm}^2$ (top), $0.8\,\mathrm{A}/\mathrm{cm}^2$ (centre) and $1.2\,\mathrm{A}/\mathrm{cm}^2$ (bottom). The scale is $5\,[(\mathrm{m}/\mathrm{s})/\mathrm{cm}]$ for the gas phase and $100\,[(\mathrm{m}/\mathrm{s})/\mathrm{cm}]$ for the liquid phase.

Anode Side

So far, every detailed two-phase study of a PEM Fuel Cell has focussed on the cathode side only. However, phase change phenomena also occur at the anode side, mainly due to changes in the pressure and gas composition. Furthermore, for an overall water balance of the fuel cell the anode side has to be included as well. This is a step towards the ultimate goal of the present model, *i.e.* to predict the fuel cell performance under various operating conditions, including a partly dehydrated membrane.

Figure 4.8 shows the rate of phase change and the liquid water saturation inside the anodic gas diffusion layer. The negative values for the rate of phase change throughout the domain indicate that condensation occurs as a result of depletion of the reactant gas. This condensation is stronger than at the cathode side, because at the anode we are dealing with a binary mixture only, which means that the decrease in the molar hydrogen fraction leads to an equivalent increase in the molar water vapour fraction. At the cathode side, this increase is partly "absorbed" up by the nitrogen, which acts as a buffer. The condensation is strongest at the channel/GDL interface, located at the top centre of each plot. Similar to the cathode side, the condensation term is lowest under the land areas because of the high pressure drop in this region.

The liquid water saturation is relatively high, ranging from around 5% at low current density to 8% at a high current density, the maximum being under the land areas. The reason for this is clear: once liquid water is being created by condensation, it is dragged into the GDL by the gas phase. Similar to the cathode side, the liquid water can only leave the GDL through the build-up of a capillary pressure gradient to overcome the viscous drag, because at steady state operation, all the condensed

water has to leave the cell.

Figure 4.9 shows the pressure and temperature distribution inside the anodic gas diffusion layer. The pressure drop at the anode side is much higher than at the cathode side, the maximum being 5000 Pa at a current density of $1.2\,\mathrm{A}/\mathrm{cm}^2$. The reason for this is again the high rate of condensation that occurs here due to the hydrogen depletion, which causes a drop in the gas phase pressure. This can also be seen from the molar hydrogen fraction: the decrease under the land areas is much less than in the absence of phase change, because the condensation of liquid water reduces the molar water vapour fraction in return. As a result, the molar hydrogen fraction is above 50% throughout the entire domain for all current densities.

The velocity profiles for both phases are shown in Figure 4.10. In the case of the anode, the gas phase flow is always directed from the channel into the GDL, because there is no reactant water that can evaporate and cause a pressure increase. The gas phase velocity is roughly two orders of magnitude higher than the liquid phase velocity, and again the highest liquid water velocity occurs at the corners of the channel/GDL interface.

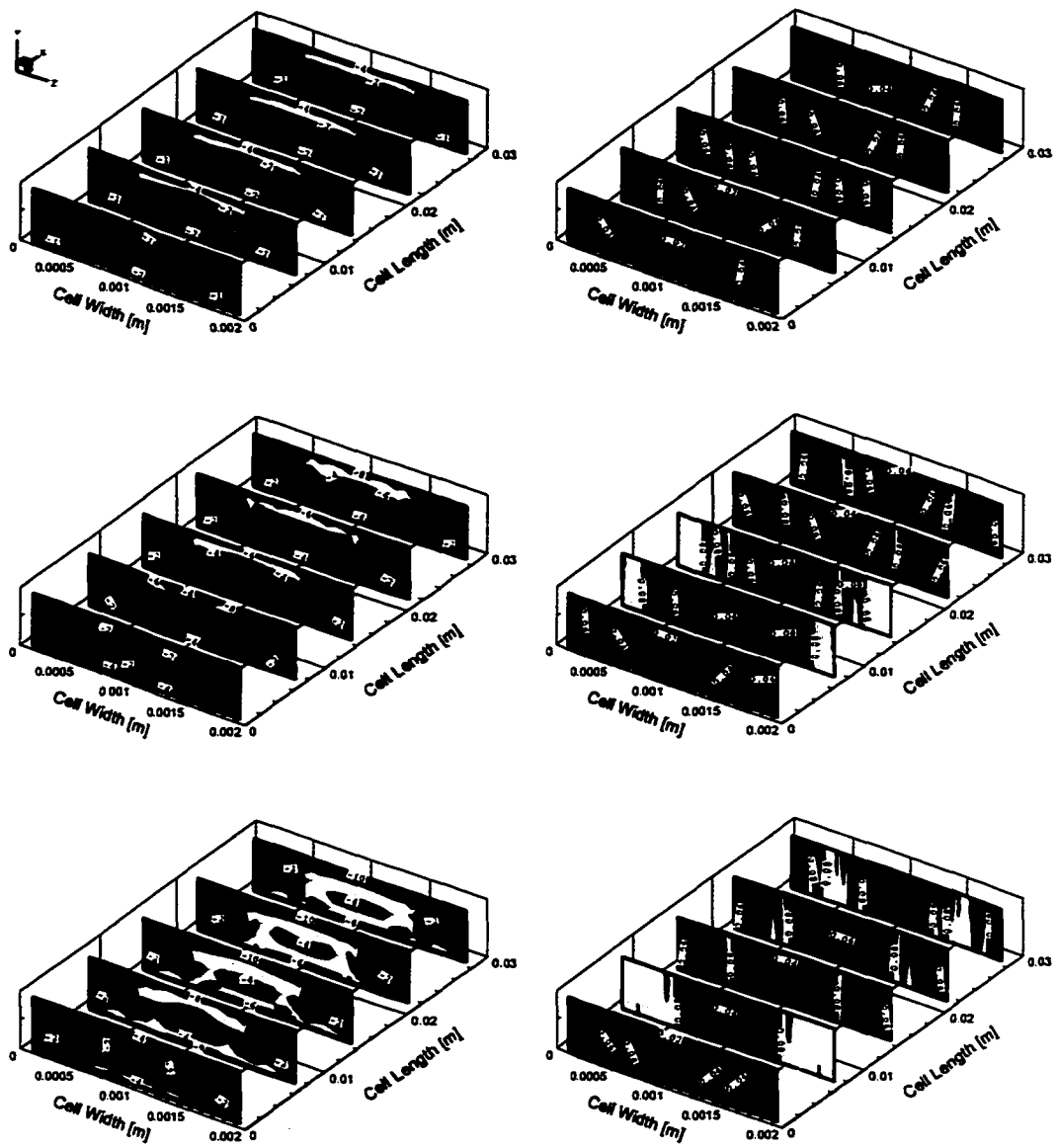

Figure 4.8: Rate of phase change [kg / (m^3 s)] (left) and liquid water saturation [−] (right) inside the anodic gas diffusion layer for three different current densities: 0.4 A / cm^2 (top), 0.8 A / cm^2 (centre) and 1.2 A / cm^2 (bottom).

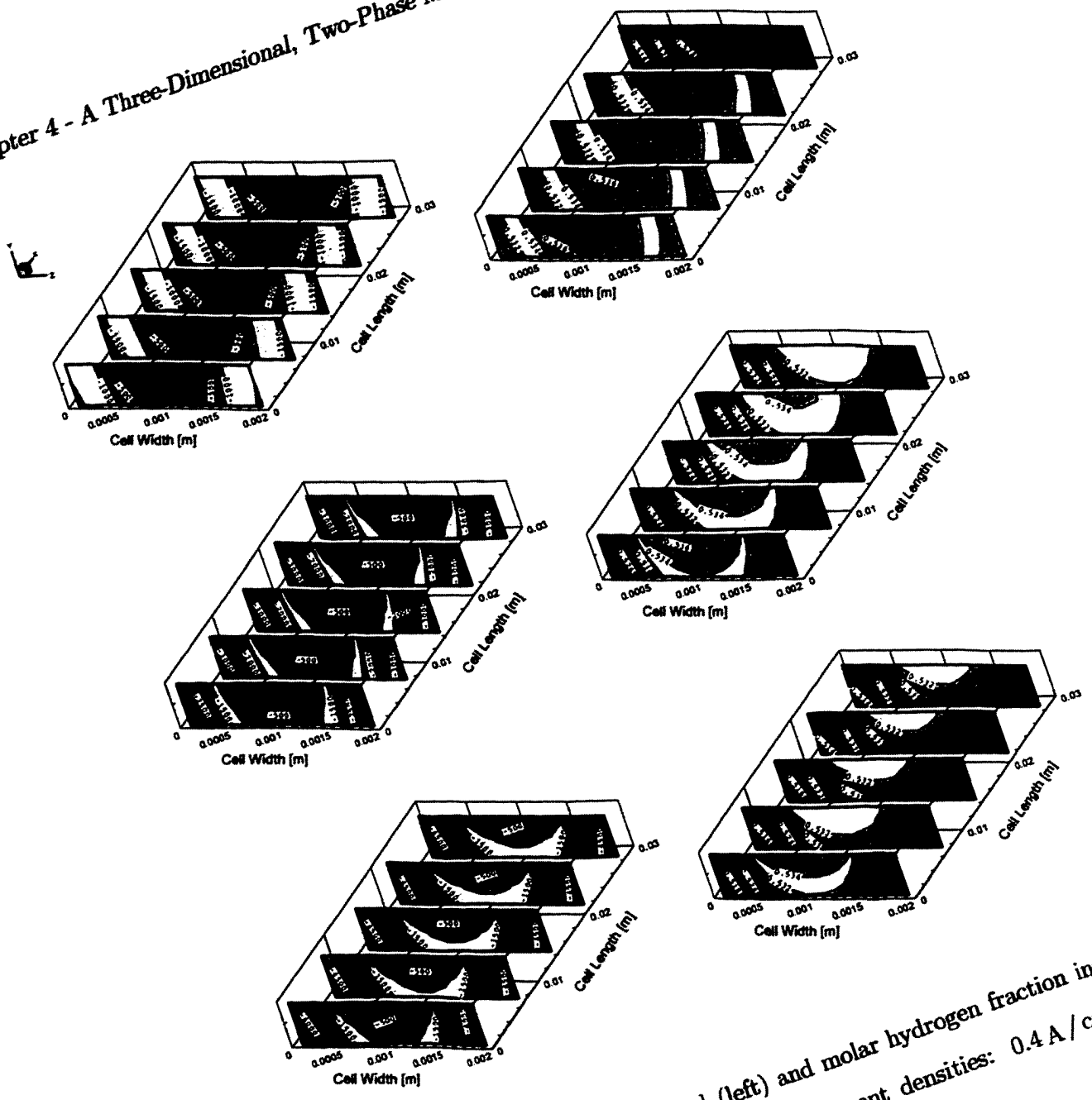

Figure 4.9: Pressure distribution [Pa] (left) and molar hydrogen fraction inside the anodic gas diffusion layer for three different current densities: $0.4\,A/cm^2$ (top), $0.8\,A/cm^2$ (centre) and $1.2\,A/cm^2$ (bottom).

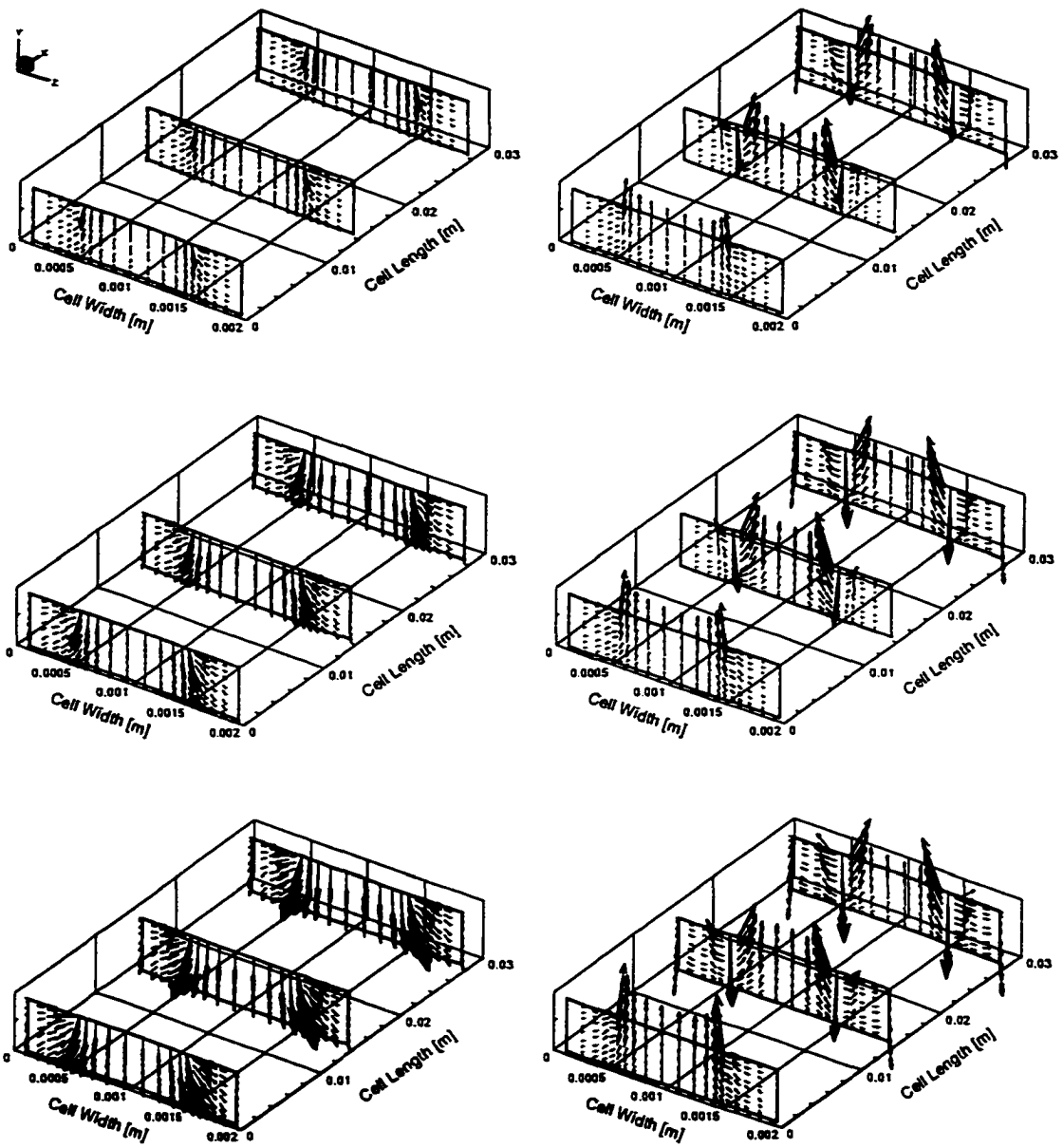

Figure 4.10: Velocity vectors of the gas phase (left) and the liquid phase (right) inside the anodic gas diffusion layer for three different current densities: $0.4\,\mathrm{A}/\mathrm{cm}^2$ (top), $0.8\,\mathrm{A}/\mathrm{cm}^2$ (centre) and $1.2\,\mathrm{A}/\mathrm{cm}^2$ (bottom). The scale is $2\,(\mathrm{m}/\mathrm{s})/\mathrm{cm}$ for the gas phase and $200\,(\mathrm{m}/\mathrm{s})/\mathrm{cm}$ for the liquid phase.

Mass Balance

Having demonstrated the basic capabilities of the two-phase model, we now examine the mass flow balances of the gas- and liquid phase in detail. The average error for the anode and cathode mass flows combined was around 2%. This value appears quite high from a computational standpoint, and it could be reduced by adding more iterations. However, it has to be noted that the results are already very consistent throughout all current densities, *i.e.* most of the results obtained follow smooth curves, as can be seen below. In addition, the computations are very demanding, and an imbalance of 2% for a problem as complex as the present one is deemed acceptable.

Figure 4.11 and 4.12 show the detailed mass flow balance for the anode and cathode, respectively. Because of the constant stoichiometric flow ratio, the incoming and outgoing gas flows increase linearly with the current density. At both sides, the total amount of liquid water leaving the cell is an order of magnitude lower than the gas phase fluxes. At the anode side, the amount of liquid water increases rapidly at high current densities, whereas it increases only up to a current density of $1.2\,\mathrm{A}/\mathrm{cm}^2$ at the cathode side, and decreases for even higher current densities. This effect will be discussed in detail, below.

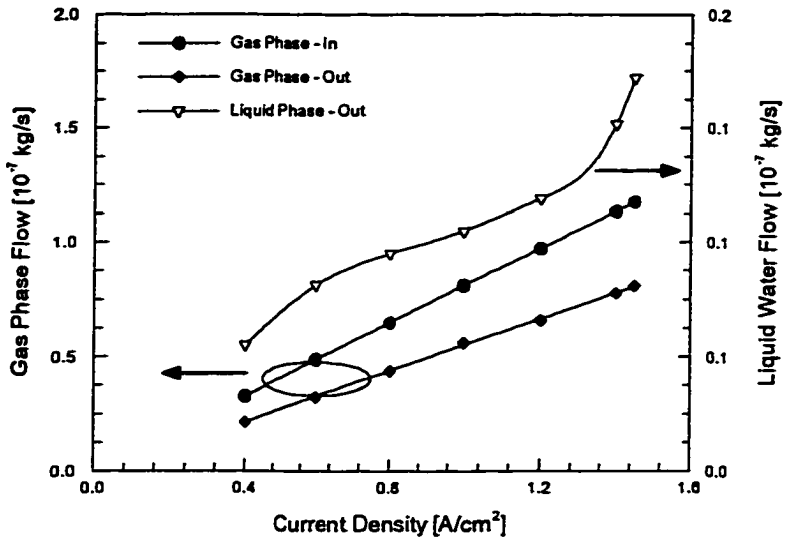

Figure 4.11: Mass flow balance at the anode side.

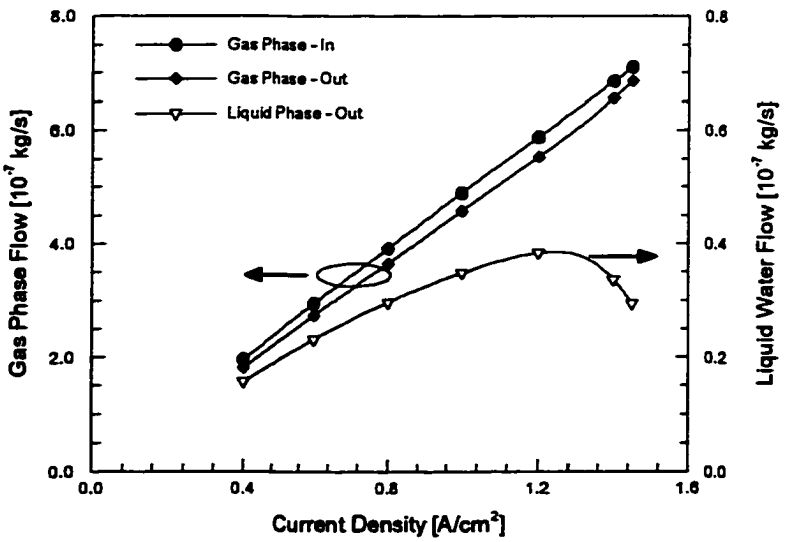

Figure 4.12: Mass flow balance at the cathode side.

Figure 4.13 shows the average liquid water saturation inside the gas diffusion layers as a function of current density. At both sides, the trend of the liquid water inside the GDL follows the observed behaviour for the water fluxes leaving the cell. At the anode side the amount of liquid water inside the GDL increases steadily from around 5% to 8% with an increase in the current density. For a current density higher than $1.2\,\mathrm{A/cm^2}$ this increase becomes very steep. The opposite is true for the cathode side, where the amount of liquid water inside the GDL increases only up to a current density of $1.2\,\mathrm{A/cm^2}$, where it reaches its maximum of around 8%, and decreases rapidly for a further increase in the current density so that beyond a current density of $1.3\,\mathrm{A/cm^2}$ the amount of water inside the anodic GDL exceeds the amount inside the cathodic GDL. The maximum in the liquid water saturation at the cathode side coincides with the maximum in the liquid water flux.

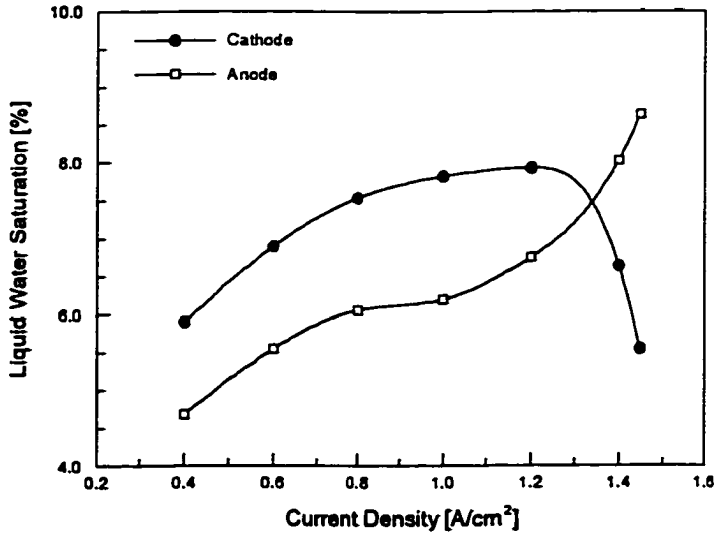

Figure 4.13: Average liquid water saturation inside the gas diffusion layers.

Figure 4.14 shows the rate of phase change and the liquid water saturation inside the cathodic GDL at a current density of $1.4\,\mathrm{A}/\mathrm{cm}^2$.

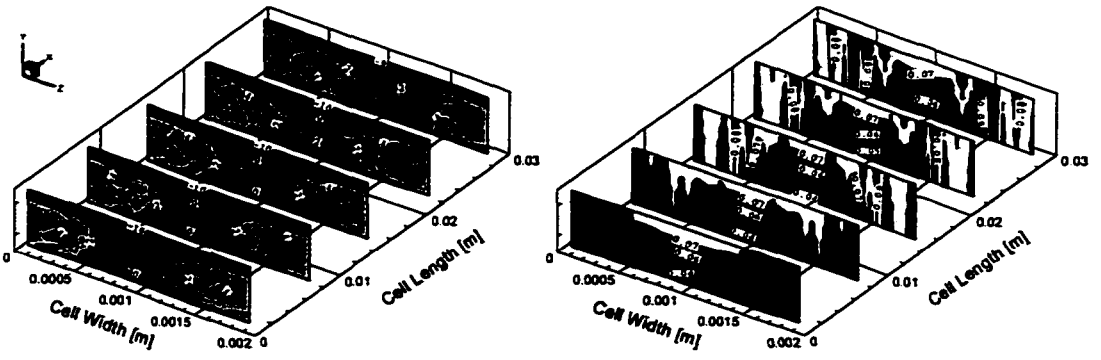

Figure 4.14: Rate of phase change $[\mathrm{kg}/(\mathrm{m}^3\,\mathrm{s})]$ (left) and liquid water saturation $[-]$ (right) inside the cathodic gas diffusion layer for a current density of $1.4\,\mathrm{A}/\mathrm{cm}^2$.

It can be seen that the rate of phase change is positive in almost the entire GDL, indicating evaporation. The liquid water distribution shows that particularly near the inlet area the maximum of the liquid water saturation occurs at the catalyst under the channel area, whereas for lower current densities it was under the land area. The reason for this is the local current density distribution. One of the findings of the single-phase model was that the fraction of current generated under the channel area increases linearly with the current density. Consequently, the liquid water production term increases under the channel area. The capillary pressure term that drives the liquid water out of the GDL is similar to a diffusion term, and clearly the distance between the catalyst layer at mid-channel and the channel is shorter than from the land area. This shorter path means that a lower capillary pressure gradient is needed to drive the water out of the cell, which leads to a decrease in the overall liquid water

saturation. Hence, two mechanisms lead to a decrease in the liquid water saturation at high current densities: the increase in evaporation along with a shift in the local current density distribution towards the channel area.

Balancing the total amount of water undergoing phase change results in a plot shown in Figure 4.15. The net phase change is calculated out of the difference between the liquid water production term and the amount of liquid water leaving the cell, *i.e.* a negative value means that, overall, water vapour entering the cell is condensed, whereas a positive value means that a fraction of the product water evaporates. Also shown is the amount of product water as a function of current density.

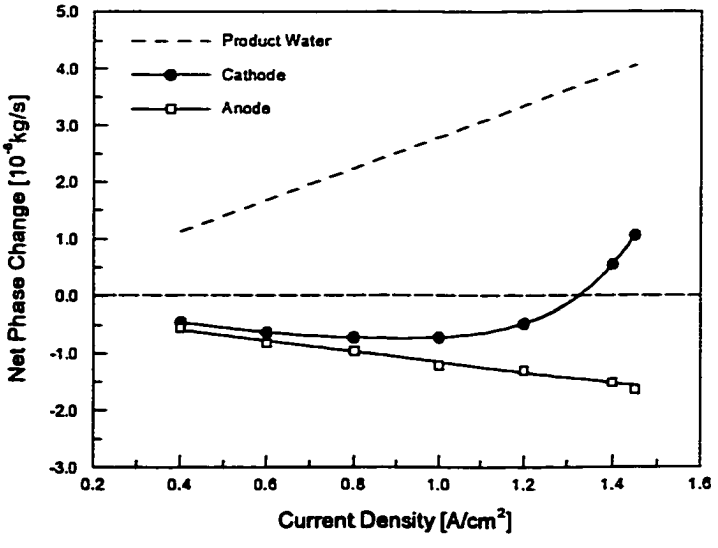

Figure 4.15: Net amount of phase change inside the gas diffusion layers. Negative values indicate condensation, and positive values evaporation.

Clearly, at the anode side, all the liquid water leaving the cell must be condensed

water. For the net phase change at the cathode side, it can be observed that condensation of incoming water occurs up to a current density of around $1.3\,\mathrm{A}/\mathrm{cm}^2$. However, the curve indicates a sharp turnaround at a current density of around $1.2\,\mathrm{A}/\mathrm{cm}^2$, where the rate of evaporation starts to increase strongly.

Because it is important to limit the amount of liquid water inside the cathodic gas diffusion layer, and at the same time keep the membrane fully humidified, especially at the anode side, it will be interesting to follow up on the current work and further investigate, how the physical mechanisms observed here depend on material and operational properties. The scope of this thesis, however, was to develope and implement the multi-phase model and identify the underlying physics at base case conditions. A detailed parametric study as was done using the single phase model is beyond the scope of this thesis.

4.8 Summary

This chapter presented a three-dimensional, two-phase model of the cathode and anode of a PEM Fuel Cell. The mathematical model accounts for the liquid water flux inside the gas diffusion layers by viscous and capillary forces and hence is capable of predicting the amount of liquid water inside the gas diffusion layers. The current model is similar to Wang *et al.* [49] and He *et al.* [18] in these aspects, but in addition, the present model accounts for non-isothermal effects, and incorporates the anode. The physics of phase change are included in the current model by prescribing the local evaporation term as a function of the amount of liquid water present and the level of undersaturation, whereas the condensation has been simplified to be a

function of the level of oversaturation only. A water channel has been included in the model, which will allow for the assessment of the effect of cooling the cell on the amount of condensation inside the fuel cell in the future.

Base case simulations have been performed for conditions representative of actual fuel cell operation including high humidified reactant streams. The base case results reveal numerous physical effects that have not been discussed in the literature, so far. Three different physical mechanisms that lead to phase change inside the gas diffusion layers were identified. A rise in temperature because of the electrochemical reaction leads to evaporation, mainly at the cathode side. If the gases entering the cell are fully humidified, the depletion of the reactants leads to an increase in the partial pressure of the water vapour, and hence to condensation along the channel and inside the gas diffusion layers. Finally, a decrease in the gas phase pressure inside the gas diffusion layers leads to a decrease in the water vapour pressure, and hence causes evaporation.

The liquid water saturation is below 10% for the chosen operating parameters at base case conditions. At the anode side it increases monotonically with the current density, whereas it attains a maximum at the cathode side and decreases rapidly at higher current densities. It was shown that this is caused by two different effects: a strong increase of the evaporation of the product water at high current densities, and a shifting of the local current density distribution towards the channel area. For the current conditions, product water only starts to evaporate at a current density of $1.3\,\mathrm{A/cm^2}$.

At the anode side all the liquid water leaving the cell is condensed water. The high levels of liquid water saturation observed at steady-state operating conditions

can be explained by the fact that the condensation water is dragged into the GDL by the gas phase, and can only leave the gas diffusion layer by capillary pressure forces, which means that there has to be a build-up of a liquid water saturation gradient in order to drive the water out.

Chapter 5

Conclusions and Outlook

5.1 Conclusions

A three-dimensional model of a PEM Fuel Cell has been developed. Employing the methods of computational fluid dynamics, the model accounts for the fluid flow inside the channels and the porous media as well as heat transfer. A single-phase version of this model is capable of predicting the distribution of the reactant gases, the temperature distribution and local current densities as well as the fuel cell performance under various operating conditions. A parametric study revealed the effect of various operating and geometrical parameters on the fuel cell performance. Where possible, qualitative comparisons were made between experimental results from the literature and results obtained with the model. Good overall agreement was obtained.

A two-phase version of the model has been developed that accounts for phase change inside the porous media. In particular, this model allows for the prediction of the amount of liquid water inside the gas diffusion layers. Compared to previ-

ous work, the two-phase model presented here has several unique features including: three-dimensionality; non-isothermal conditions; and extension of the computational domain to include the anode as well as a cooling channel. The results obtained with the multi-phase model helped understanding the physics of phase change inside a porous medium. An overall water balance of the fuel cell resulted in very interesting insights into various effects, particularly at the cathode side.

5.2 Contributions

During the course of this thesis the following contributions were made in detail:

- Finalizing an existing three-dimensional model. The model that has been described in Chapter 2 was originally developed by Dr. Dongming Lu and Dr. Ned Djilali at the *Institute for Integrated Energy Systems* of the University of Victoria *(IESVic)*. During the research that led to this thesis, this model was completed and refined, and convergence difficulties resolved. The changes made to the existing model led to an overall increase of convergence speed by a factor of ten without reducing any of its capabilities.

- Conducting a detailed parametric study using the single-phase model and a literature study in order to find functional relationships between operational parameters and input parameters for this model. A detailed study employing a three-dimensional model such as the one presented in Chapter 3 has not been published, yet, and is therefore an original contribution.

- A contribution in terms of model development has been made by further developing the single-phase model in order to account for a second phase and phase

change. The model presented in Chapter 4 is the first three-dimensional model of a PEM Fuel Cell that includes a detailed non-isothermal multi-phase model of the gas diffusion layer. In addition, it has some unique features such as the inclusion of the water cooling channel, and the anode side of the cell.

- The capabilities of the two-phase model have been demonstrated in a base case study. Contributions were made in terms of the fundamental understanding of the physical mechanisms that lead to phase change and the distribution of liquid water inside a PEM Fuel Cell.

5.3 Outlook

The model presented here represents a significant step towards physically realistic three-dimensional simulations of a complete fuel cell under various operating conditions. The results presented in this thesis demonstrate the capabilities of the model in providing insight and shedding light on many of the physical phenomena that lead to experimentally observed fuel cell performance. However, the model can, by no means, be considered complete.

In order to further improve this model, there are numerous extensions and improvements that should be considered. The following is a list of improvements that could and should be made in order to fully account for all first-order effects:

- Improve assumptions made in modelling the electrochemistry. One of the key assumptions made was that the activation overpotential at the cathode is constant throughout the catalyst layer. Although this assumption has also been made by other authors (He *et al.* [18], Wang *et al.* [49]) a better approach

has been taken by Dutta *et al.* [14], whose model is more complete in terms of the electrochemistry included. This error introduced by the above-mentioned assumption is believed to be small. However, it would lead to slightly different distribution of the local current density, and this was pointed out to be a sensitive parameter.

- Include a membrane model. So far, the transport phenomena inside the membrane have been greatly simplified. A detailed membrane model is very complex, and in many cases, authors have used the empirical model devised by Springer *et al.* [38]. An alternative would be the model presented by Nguyen *et al.* [28]. Although these models are limited in their range of validity, they can provide insight into the basic transport phenomena that occur inside the fuel cell membrane.

- Include unsteady-state phenomena. The current model is at steady-state, whereas comparable two-phase models can include transient effects (*e.g.* Wang *et al.* [49]). Although these effects have been found to be small - changes in terms of fuel cell performance occur almost instantly - this can not be true for the mass transport phenomena, which are in part limited by diffusion.

Appendix A

On Multicomponent Diffusion

In the following, we deviate from the common notation of i and j for different species. Instead, numbers are used in order to keep with common notation in literature on multi-species diffusion (*e.g.* [39] and [13]). "1" refers to oxygen at the cathode side and hydrogen at the anode side, and "2" refers to water vapour at both sides. In a ternary diffusion problem, "3" commonly refers to the background fluid (*e.g.* nitrogen at the cathode and carbon-dioxide at the anode), but only two equations are of interest, since the last mass fraction results out of:

$$1 = y_1 + y_2 + y_3 \tag{A.1}$$

When only a binary mixture is considered, diffusion can be expressed via *Fick's law* [13], and the generic advection-diffusion equation for species conservation as solved by the CFX code becomes [1]:

$$\nabla \cdot (\rho_g \mathbf{u}_g y_{gi}) - \nabla \cdot (\rho_g D_{gi} \nabla y_{gi}) = S_{gi} \tag{A.2}$$

where the second term on the left hand side can be recognized as Fick's law for binary diffusion, written in the form of a mass averaged reference frame, and S_{gi} represents a source term for species i.

In a mixture with n components, however, the diffusive flux of species i depends on the concentration gradient of $n-1$ components as expressed by the Stefan-Maxwell equations:

$$\nabla \cdot x_i = -\sum_{j=1}^{n-1} \frac{x_i x_j}{\mathfrak{D}_{ij}} (\mathbf{v}_i - \mathbf{v}_j) \tag{A.3}$$

where $\mathbf{v}_i$ is the diffusion velocity vector of species i, x is the molar fraction and $\mathfrak{D}_{ij}$ is the binary diffusivity of any two species. It can be seen that this expression is impractical to use.

A more practical, yet equivalent description is the *generalized Fick's law*, which can be rationalized using irreversible thermodynamics [13]. For a system with n components, $n-1$ equations are needed, e.g. for the ternary case:

$$j_1 = -\rho D_{11} \nabla y_1 - \rho D_{12} \nabla y_2 \tag{A.4}$$

$$j_2 = -\rho D_{21} \nabla y_1 - \rho D_{22} \nabla y_2 \tag{A.5}$$

where ρ is the mixture density in [kg / m^3] and j_1 and j_2 are the mass diffusion fluxes relative to the mass average velocity with the unit [kg / (m^2 s)]. The diagonal terms (the D_{ii}) are called "main-term" diffusion coefficients, because they are commonly large and similar in magnitude to binary values. The off-diagonal term ($D_{ij,i\neq j}$), called the "cross-term" diffusion coefficients, are often 10% or less of the main terms

[13]. Note that the diffusion coefficients D in the above expressions are not the binary coefficients, but they depend on these in a manner specified below. A similar derivation has been made by Taylor and Krishna [39].

Equations A.4 and A.5 can be expressed in matrix form as:

$$(\mathbf{j}) = -\rho\,[\mathbf{D}]\,(\nabla \mathbf{y}) \tag{A.6}$$

where $(\mathbf{j})$ and $(\mathbf{y})$ are vectors of the order $n-1$ and $[\mathbf{D}]$ is a matrix of dimension $n-1 \times n-1$.

A further complication arises, because Fick's law is originally stated for *molar averaged* quantities [39]:

$$(\mathbf{J}) = -c_t\,[\mathbf{D}^0]\,\nabla x \tag{A.7}$$

where $\mathbf{J}$ is the molar diffusion flux relative to the molar averaged velocity in $[\mathrm{mol}\,/\,(\mathrm{m}^2\,\mathrm{s})]$, c_t is the mixture molar density in $[\mathrm{mol}\,/\,\mathrm{m}^3]$ and $[\mathbf{D}^0]$ refers to the binary diffusivities in the molar averaged velocity reference frame.

In order to relate $[\mathbf{D}^0]$ to the mass averaged reference frame $[\mathbf{D}]$ the following transformation has to be done [39]:

$$[\mathbf{D}] = [\mathbf{B}^{uo}]^{-1}\,[\mathbf{y}]\,[\mathbf{x}]^{-1}\,[\mathbf{D}^0]\,[\mathbf{x}]\,[\mathbf{y}]^{-1}\,[\mathbf{B}^{uo}] = [\mathbf{B}^{ou}]\,[\mathbf{y}]\,[\mathbf{x}]^{-1}\,[\mathbf{D}^0]\,[\mathbf{x}]\,[\mathbf{y}]^{-1}\,[\mathbf{B}^{ou}]^{-1} \tag{A.8}$$

where $[\mathbf{x}]$ is a diagonal matrix whose nonzero elements are the molar fractions x_i. The matrix $[\mathbf{y}]$ is also diagonal with nonzero elements that are the mass fractions y_i.

The matrices $[\mathbf{B}^{uo}]^{-1}$ and $[\mathbf{B}^{ou}]$ have elements defined by Equations A.9 and A.10, respectively [39].

$$\mathbf{B}_{ik}^{uo} = \delta_{ik} - y_i \left(\frac{x_k}{y_k} - \frac{x_n}{y_n} \right) \tag{A.9}$$

$$\mathbf{B}_{ik}^{ou} = \delta_{ik} - y_i \left(1 - \frac{y_n x_k}{x_n y_k} \right) \tag{A.10}$$

where n denotes the background fluid and δ_{ik} is the "*Kronecker-Delta*" with the properties:

$$\delta_{ik} = 1, i = k \tag{A.11}$$

$$\delta_{ik} = 0, i \neq k \tag{A.12}$$

The exact relationship between the diffusion coefficients $[\mathbf{D}^0]$ and the binary diffusion coefficients is not known, except for the dilute gas limit, given by [13]:

$$[\mathbf{D}^0] = \frac{\mathfrak{D}_{12}\mathfrak{D}_{13}\mathfrak{D}_{23}}{\mathfrak{D}_{23}x_1 + \mathfrak{D}_{13}x_2 + \mathfrak{D}_{12}x_3} \begin{bmatrix} \frac{x_1}{\mathfrak{D}_{12}} + \frac{x_2+x_3}{\mathfrak{D}_{23}} & x_1\left(\frac{1}{\mathfrak{D}_{13}} - \frac{1}{\mathfrak{D}_{12}}\right) \\ x_2\left(\frac{1}{\mathfrak{D}_{23}} - \frac{1}{\mathfrak{D}_{12}}\right) & \frac{x_1+x_3}{\mathfrak{D}_{13}} + \frac{x_2}{\mathfrak{D}_{12}} \end{bmatrix} \tag{A.13}$$

where x_i denotes the molar fraction of species i and $\mathfrak{D}_{ij}$ are the binary diffusion coefficients.

Comparing equation A.2, solved by the CFX code, with equations A.4 and A.5 shows that the flux caused by the "cross-term" diffusion has to be accounted for in a source term on the right hand side, according to:

$$\nabla \cdot (\rho_g \mathbf{u}_g y_{gi}) - \nabla \cdot (\rho_g D_{gii} \nabla y_{gi}) = \nabla \cdot (\rho_g D_{gij} \nabla y_{gj}) \tag{A.14}$$

where i stands for oxygen at the cathode side and hydrogen at the anode side, and j denotes water vapour at both sides.

Overall, multi-component diffusion is a complex topic in itself, and the interested reader is referred to Cussler [13] and Taylor & Krishna [39].

Appendix B

Comparison between the Schlögl Equation and the Nernst-Planck Equation

This appendix shows, how the description of the water flux through the membrane compares to the approach used by Nguyen *et al.* [28], who used a modified version of the Nernst-Planck equation.

The well-established Nernst-Planck equation describes the flux of a charged species through an electrical field by migration, diffusion and convection, according to [4]:

$$\vec{N}_i = -z_i \frac{F}{RT} \mathfrak{D}_i c_i \nabla \Phi - \mathfrak{D}_i \nabla c_i + c_i \vec{v} \tag{B.1}$$

Nguyen *et al.* used a modified version of this equation, which included the effect of electro-osmotic drag instead of the migration term to describe the flux of liquid water through the membrane:

$$\vec{N}_{w,m} = n_d \frac{\vec{i}}{F} - \mathfrak{D}_w \nabla c_w - c_w \frac{k_p}{\mu_l} \nabla p \tag{B.2}$$

where n_d is the electro-osmotic drag coefficient, *i.e.* the number of water molecules dragged by each hydrogen proton that migrates through the membrane and $\mathfrak{D}_w$ is the diffusion coefficient of water in the membrane. If we want to compare this expression with the Schlögl equation that is used in the model described in this thesis, we need to find an expression for one of the material properties as a function of the parameters used in the expression above.

Replacing the local current density in equation B.2 by Ohm's law and assuming a constant electrical conductivity of the membrane yields:

$$\vec{N}_{w,m} = -n_d \frac{\kappa}{F} \nabla \Phi - \mathfrak{D}_w \nabla c_w - c_w \frac{k_p}{\mu_l} \nabla p \tag{B.3}$$

Furthermore, it has been found in the simulations by Yi and Nguyen [52] that the contribution of the second term on the right hand side, *i.e.* the back-diffusion of water, is small compared to the electro-osmotic drag and the convection, and shall be neglected for simplicity:

$$\vec{N}_{w,m} = -n_d \frac{\kappa}{F} \nabla \Phi - c_w \frac{k_p}{\mu_l} \nabla p \tag{B.4}$$

On the other hand, in the model presented here the flux of liquid water through the membrane is governed by the Schlögl equation:

$$\mathbf{u}_l = \frac{k_\Phi}{\mu_l} z_f c_f F \nabla \Phi - \frac{k_p}{\mu_l} \nabla p \tag{B.5}$$

Multiplying the pore-water velocity **u** with the molar concentration of water inside the membrane, c_w, gives the molar flux of water inside the membrane described by the Schlögl equation:

$$\vec{N}_{w,m} = c_w \frac{k_\Phi}{\mu_l} z_f c_f F \nabla \Phi - c_w \frac{k_p}{\mu_l} \nabla p \tag{B.6}$$

Electroneutrality in the membrane requires that [7]:

$$z_f c_f + \sum_i z_i c_i = 0 \tag{B.7}$$

and since the only mobile ions in the membrane are the hydrogen ions, this leads to [7]:

$$-z_f c_f = c_{H^+} \tag{B.8}$$

which leaves for the final version of the modified Schlögl equation:

$$\vec{N}_{w,m} = -c_w \frac{k_\Phi}{\mu_l} c_{H^+} F \nabla \Phi - c_w \frac{k_p}{\mu_l} \nabla p \tag{B.9}$$

Comparing this equation with equation B.4 shows that both expressions are similar. In order to compare the results obtained with both models, we have to use the same modelling parameters, *e.g.* by adjusting the electrokinetic permeability k_Φ used in our model to a value that corresponds to the model by Yi and Nguyen [52]:

$$-n_d \frac{\kappa}{F} = c_w \frac{k_\Phi}{\mu_l} c_{H^+} F \tag{B.10}$$

Solving this expression for the electrokinetic permeability yields:

$$k_\Phi = n_d \frac{\kappa}{F^2} \frac{\mu_l}{c_w c_{H^+}} \tag{B.11}$$

and assuming that the membrane is fully humified, the molar water concentration inside the membrane can be determined via:

$$c_w = \frac{\rho_l}{M_w} \cdot \varepsilon_{w,m} \tag{B.12}$$

where ρ_l is the density of liquid water, M_w is the molecular weight of water (roughly 18×10^{-3} kg/mol), and $\varepsilon_{w,m}$ is the volume fraction of liquid water inside the membrane which has been determined to be 0.28 at 80 °C by Parthasarathy *et al.* [32]. The only unknown parameter in the above equation is now the electro-osmotic drag coefficient n_d, and this is approximated by Nguyen and White [28] to be:

$$n_d = 0.0049 + 2.02a_a - 4.53a_a^2 + 4.09a_a^3; \quad a_a \leq 1 \tag{B.13}$$

where a_a is the water-vapour activity at the anode side. In our model, we assume that the gases are saturated with water, and so the water-vapour activity is unity. Hence, solving equation B.11 with the parameters given in Table 2.7 yields:

$$k_\Phi = 2.0 \times 10^{-20}\,\mathrm{m}^2 \tag{B.14}$$

This compares to a value of $k_\Phi = 7.18 \times 10^{-20}\,\mathrm{m}^2$ that was used for the base case of the model presented in this thesis.

Appendix C

The Dependence of the Hydraulic Permeability of the GDL on the Porosity

Verbrugge and Hill [45] outline a method in order to obtain a theoretical value for the permeability, based on the assumption of a GDL structure can be adequately represented by an array of capillary pores with a uniform cross section. In that case the permeability can be described by [34]:

$$k_p = \frac{\varepsilon^3}{5S_o^2(1-\varepsilon)^2} \tag{C.1}$$

where k_p is the hydraulic permeability, ε is the porosity and S_o is the specific surface area in [m^2 / m^3], or the surface exposed to the fluid per unit volume of solid. For an array of pores of circular cross section, it holds that [45]

$$S_o = \frac{4\varepsilon}{d(1-\varepsilon)} \tag{C.2}$$

where d is the pore-width. Combining Equations C.1 and C.2 yields a simple expression for the permeability:

$$k_p = \frac{\varepsilon^3}{5\left(\frac{4\varepsilon}{d(1-\varepsilon)}\right)^2(1-\varepsilon)^2} = \frac{d^2}{80}\varepsilon \tag{C.3}$$

Hence, assuming that the diameter of the pores remains constant[1] the hydraulic permeability of the GDL is a linear function of the gas-phase porosity. Using this relationship the values in Table C.1 have been obtained by scaling the value for the permeability for our base case of $\varepsilon = 0.4$ linearly with the porosity.

Table C.1: Hydraulic permeabilities used for different GDL porosities

ε	0.3	0.4	0.5	0.6
k_p [m^2]	3.55×10^{-19}	$4.73 * 10^{-19}$	$5.91 * 10^{-19}$	$7.1 * 10^{-19}$

Although these changes were made to the permeability, the results showed that they did not affect the results in any way. This confirms that diffusion is the dominating transport mechanism that drives the reactant gases towards the catalyst layer.

[1]This assumption is probably not very accurate. However, the effect of the convection compared to diffusion inside the porous GDL is small, and therefore the exact correlation between the permeability and the porosity is not believed to be critical.

References

[1] *CFX-4.3 Solver Manual.* AEA Technology plc, Didcot, UK, 2000.

[2] A. J. Appleby and F. R. Foulkes. *Fuel Cell Handbook.* Krieger Publishing Company, Florida, 1993.

[3] H. D. Baehr and K. Stephan. *Heat and Mass Transfer.* Springer, Berlin, 1998.

[4] A. J. Bard and L. R. Faulkner. *Electrochemical Methods.* Wiley, New York, 1980.

[5] J. J. Baschuk and X. Li. "Modelling of polymer electrolyte membrane fuel cells with variable degrees of water flooding". *J. Power Sources*, 86:181–195, 2000.

[6] G. K. Bathcelor. *An Introduction to Fluid Dynamics.* Cambridge University Press, 1970.

[7] D. M. Bernardi and M. W. Verbrugge. "Mathematical Model of a Gas Diffusion Electrode Bonded to a Polymer Electrolyte". *AIChE J.*, 37(8):1151–1163, 1991.

[8] D. M. Bernardi and M. W. Verbrugge. "A Mathematical Model of the Solid-Polymer-Electrolyte Fuel Cell". *J. Electrochem. Soc.*, 139(9):2477–2491, 1992.

[9] D. Bevers, M. Woehr, K. Yasuda, and K. Oguro. "Simulation of a Polymer Electrolyte Fuel Cell Electrode". *J. Applied Electrochem.*, 27:1254–1264, 1997.

[10] R. B. Bird, W. Steward, and E. N. Lightfood. *Transport Phenomena.* Wiley, New York, 1960.

[11] J. O'M Bockris and S. Srinivasan. *Fuel Cells: Their Electrochemistry.* McGraw-Hill, New York, 1969.

[12] K.H. Choi, D.-H. Peck, C. S. Kim, D.-R. Shin, and T.-H. Lee. "Water transport in polymer membranes for PEMFC". *J. Power Sources*, 86:197–201, 2000.

[13] E. L. Cussler. *Diffusion–Mass Transfer in Fluid Systems.* Cambridge University Press, 1984.

[14] S. Dutta, S. Shimpalee, and J.W Van Zee. "Three-dimensional Numerical Simulation of Straight Channel PEM Fuel Cells". *J. Applied Electrochem.*, 30:135–146, 2000.

[15] J. H. Ferziger and M. Peric. *Computational Methods for Fluid Dynamics.* Springer, Berlin, 1997.

[16] T. F. Fuller and J. Newman. "Water and Thermal Managament in Solid-Polymer-Electrolyte Fuel Cells". *J. Electrochem. Soc.*, 140(5):1218–1225, 1993.

[17] V. Gurau, H. Liu, and S. Kakac. "Two-Dimensional Model for Proton Exchange Membrane Fuel Cells". *AIChE Journal*, 44(11):2410–2422, 1998.

[18] W. He, J. S. Yi, and T. V. Nguyen. "Two-Phase Flow Model of the Cathode of PEM Fuel Cells Using Interdigitated Flow Fields". *AIChE Journal*, 46(10):2053–2064, 2000.

[19] F. P. Incropera and D. P. DeWitt. *Fundamentals of Heat and Mass Transfer.* Wiley, New York, fourth edition, 1996.

[20] J. Kim, S.-M. Lee, S. Srinivasan, and C. E. Chamberlin. "Modeling of proton Exchange Membrane Fuel Cell Performance with an Empirical Equation". *J. Electrochem. Soc.*, 142(8):2670–2674, 1995.

[21] J. A. Kolde, B. Bahar, M. S. Wilson, T. A. Zawodzinski, and S. Gottesfeld. "Advanced Composite Polymer Electrolyte Fuel Cell Membranes". *Proc. Electrochem. Society*, 23:193–201, 1995.

[22] M. J. Lampinen and M. Fomino. "Analysis of Free Energy and Entropy Changes for Half-Cell Reactions". *J. Electrochem. Soc.*, 140(12):3537–3546, 1993.

[23] J. Larminie and A. Dicks. *Fuel Cell Systems Explained.* Wiley, Chichester, 2000.

[24] M. C. Leverett. "Capillary Behavior in Porous Solids". *AIME Trans.*, 142:152–169, 1941.

[25] M. J. Moran and H. N. Shapiro. *Fundamentals of Engineering Thermodynamics.* Wiley, New York, third edition, 1995.

[26] J. S. Newman. *Electrochemical Systems.* Prentice Hall, Englewood Cliffs, New Jersey, 1991.

[27] T. V. Nguyen. "A Gas Distributor Design for Proton-Exchange-Membrane Fuel Cells". *J. Electrochem. Soc.*, 143(5):L103–L105, 1996.

[28] T. V. Nguyen and R. E. White. "A Water and Heat Management Model for Proton-Exchange-Membrane Fuel Cells". *J. Electrochem. Soc.*, 140(8):2178–2186, 1993.

[29] K. B. Oldham and J. C. Myland. *Fundamentals of Electrochemical Science.* Academic Press, 1994.

[30] A. Parthasarathy, B. Dave, S. Srinivasan, J. A. Appleby, and C. R. Martin. "The Platinum Microelectrode/Nafion Interface: An Electrochemical Impedance Spectroscopic Analysis of Oxygen Reduction Kinetics and Nafion Characteristics". *J. Electrochem. Soc.*, 139(6):1634–1641, 1992.

[31] A. Parthasarathy, S. Srinivasan, J. A. Appleby, and C. R. Martin. "Pressure Dependence of the Oxygen Reduction Reaction at the Platinum Microelectrode/Nafion Interface: Electrode Kinetics and Mass Transport". *J. Electrochem. Soc.*, 139(10):2856–2862, 1992.

[32] A. Parthasarathy, S. Srinivasan, J. A. Appleby, and C. R. Martin. "Temperature Dependence of the Electrode Kinetics of Oxygen Reduction at the Platinum/Nafion Interface – A Microelectrode Investigation". *J. Electrochem. Soc.*, 139(9):2530–2537, 1992.

[33] R. E. De La Rue and C. W. Tobias. "On the Conductivity of Dispersions". *J. Electrochem. Soc.*, 106:827–836, 1959.

[34] A. E. Scheidegger. *The Physics of Flow through Porous Media.* University of Toronto Press, Toronto, third edition, 1974.

[35] R. Schloegl. "Zur Theorie der anomalen Osmose". *Z. Physik. Chem.*, 3:73–102, 1955.

[36] S. Shimpalee and S. Dutta. "Numerical Prediction of Temperature Distribution in PEM Fuel Cells". *Num. Heat Transfer*, 38:111–128, 2000.

[37] T. E. Springer, M. S. Wilson, and S. Gottesfeld. "Modeling and Experimental Diagnostics in Polymer Electrolyte Fuel Cells". *J. Electrochem. Soc.*, 140(12):3513–3526, 1993.

[38] T. E. Springer, T. A. Zawodzinski, and S. Gottesfeld. "Polymer Electrolyte Fuel Cell Model". *J. Electrochem. Soc.*, 138(8):2334–2342, 1991.

[39] R. Taylor and R. Krishna. *Multicomponent Mass Transfer.* Wiley, New York, 1993.

[40] D. Thirumalai and R. E. White. "Mathematical Modeling of Proton-Exchange-Membrane Fuel-Cell Stacks". *J. Electrochem. Soc.*, 144(5):1717–1723, 1997.

[41] E. A. Ticianelli, J. G. Beery, and S. Srinivasan. "Dependence of Performance of Solid Polymer Electrolyte Fuel Cells with Low Platinum Loading on Morphologic Characteristics of the Electrodes". *J. Electroanal. Chem.*, 251:275–295, 1988.

[42] E. A. Ticianelli, C. R. Derouin, A. Redondo, and S. Srinivasan. "Methods to Advance Technology of Proton Exchange Membrane Fuel Cells". *J. Electrochem. Soc.*, 135(9):2209–2214, 1988.

[43] K. S. Udell. "Heat Transfer in Porous Media Considering Phase Change and Capillarity – The Heat Pipe Effect". *Int. J. Heat Mass Transfer*, 28(2):485–495, 1985.

[44] S. Um, C. Y. Wang, and K. S. Chen. "Computational Fluid Dynamics Modeling of Proton Exchange Membrane Fuel Cells". *J. Electrochem. Soc.*, 147(12):4485–4493, 2000.

[45] M. W. Verbrugge and R. F. Hill. "Transport Phenomena in Perfluorosulfonic Acid Membranes During the Passage of Current". *J. Electrochem. Soc.*, 137(4):1131–1138, 1990.

[46] K. J. Vetter. *Electrochemical Kinetics.* Academic Press, New York, 1967.

[47] C. Y. Wang and P. Cheng. "Multiphase Flow and Heat Transfer in Porous Media". *Adv. Heat Transfer*, 30:93–196, 1997.

[48] J.-T. Wang and R. F. Savinell. "Simulation Studies on the Fuel Electrode of a H2-O2 Polymer Electrolyte Fuel Cell". *Electrochimica Acta*, 37(15):2737–2745, 1992.

[49] Z. H. Wang, C. Y. Wang, and K. S. Chen. "Two-phase flow and transport in the air cathode of proton exchange membrane fuel cells". *J. Power Sources*, 94:40–50, 2001.

[50] K. R. Weisbrod, S. A. Grot, and N. E. Vanderborgh. "Through-the-Electrode Model of a Proton Exchange Membrane Fuel Cell". *Electrochem. Soc. Proceedings*, 95(23):152–166, 1995.

[51] M. Woehr, K. Bolwin, W. Schnurnberger, M. Fischer, W. Neubrand, and G. Eigenberger. "Dynamic Modelling and Simulation of a Polymer Membrane Fuel Cell Includinmg Mass Transport Limitations". *Int. J. Hydrogen Energy*, 23(3):213–218, 1998.

[52] J. S. Yi and T. V. Nguyen. "An Along-the-Channel Model for Proton Exchange Membrane Fuel Cells". *J. Electrochem. Soc.*, 145(4):1149–1159, 1998.

[53] J. S. Yi and T. V. Nguyen. "Multicomponent Transport in Porous Electrodes of Proton Exchange Membrane Fuel Cells Using the Interdigitated Gas Distributors". *J. Electrochem. Soc.*, 146(1):38–45, 1999.